Effect of Velocity Ratio on the Performance of a Shrouded Tail Rotor in Edgewise Flight

Purui Chen

Department of Mechanical Engineering

McGill University
Montreal

A thesis submitted to McGill University
in partial fulfilment of the requirements of the degree of
Master of Science

August 2024

Declaration

I declare that the contents of this thesis are original, except where specific reference is made to the work of others. It has not been submitted in whole, or in part, for consideration for any other degree or qualification at this, or any other university. This dissertation is my own work, and contains nothing which is the outcome of work done in collaboration with others, except as specified in the text and Acknowledgements.

Purui Chen
Montreal
August 2024

Abstract

The concept of a shrouded rotor has gained considerable attention in modern rotorcraft design due to its potential to improve the aerodynamic and aeroacoustics performance of the rotor. By enclosing the rotor within a cylindrical shroud, additional thrust can be generated while achieving considerable noise reduction. Most existing research has focused on the hovering condition, assuming a zero-freestream velocity. However, during the climb and descent, the shrouded tail rotor operates in an edgewise flight condition, leading to observable inflow distortion. In this study, a shrouded rotor was experimentally examined in a wind tunnel at various tip-to-freestream velocity ratios μ. The non-dimensional aerodynamic loads showed a clear trend with the change of μ, indicating that μ is a decisive factor for the aerodynamic performance. Measurements of the pressure distribution on the shroud's inner surface were investigated, which showed a clear change in topology as μ increased. A peak positive pressure was observed on the downwind side of the shroud, which moved towards the shroud exit as μ increased. The velocity at the inlet and outlet of the shroud were measured. The mean velocity at the inlet shows an uneven distribution in the front and rear half, proving the generation of the nose-up pitching moment. The topology of the mean velocity distribution also varies with the increase of μ. A spectral analysis of the velocity data was also conducted, which would help further acoustic studies on the shrouded rotor in this flight condition.

Abrégé

Le concept de rotor caréné a suscité une attention considérable dans la conception des giravions modernes en raison de son potentiel d'amélioration des performances aérodynamiques et aéroacoustiques du rotor. En enfermant le rotor dans une enveloppe cylindrique, il est possible de générer une poussée supplémentaire tout en réduisant considérablement le bruit. La plupart des recherches existantes se sont concentrées sur les conditions de vol stationnaire, en supposant une vitesse nulle dans la veine libre. Cependant, pendant la montée et la descente, le rotor de queue caréné fonctionne dans le sens de la marche, ce qui entraîne une distorsion observable de l'écoulement. Dans cette étude, un rotor caréné a été examiné expérimentalement dans une soufflerie à différents rapports de vitesse entre l'extrémité et l'écoulement libre μ. Les charges aérodynamiques non dimensionnelles ont montré une tendance claire avec le changement de μ, indiquant que μ est un facteur décisif pour la performance aérodynamique. Les mesures de la distribution de la pression sur la surface intérieure de l'enveloppe ont été étudiées et ont montré un changement clair de la topologie avec l'augmentation de μ. Un pic de pression positive a été observé du côté vent arrière de la coiffe, qui s'est déplacé vers la sortie de la coiffe au fur et à mesure que μ augmentait. La vitesse à l'entrée et à la sortie du linceul a été mesurée. La vitesse moyenne à l'entrée montre une distribution inégale dans les moitiés avant et arrière, ce qui prouve la génération du moment de tangage à cabrer. La topologie de la distribution de la vitesse moyenne varie également avec l'augmentation de μ. Une analyse spectrale des données de vitesse a également été réalisée, ce qui devrait permettre d'approfondir les études acoustiques sur le rotor caréné dans ces conditions de vol.

Acknowledgements

First and foremost, I would like to express my deepest gratitude to my supervisor, Professor Jovan Nedić, for his invaluable guidance and supervision throughout this research. His insights and encouragement have been instrumental in shaping the direction and quality of this thesis.

I would also like to extend my thanks to Dylan, Anushka, Leah, and Ziad from McGill Fluid Dynamics Lab for their kind assistance and collaboration during the design and execution of the experiments. Their expertise and support have been crucial to the success of this research.

I am profoundly grateful to my parents for their unwavering support and encouragement, especially during times when I felt stressed and depressed during this journey. Their love and understanding have been a constant source of motivation for me.

Finally, I would like to acknowledge my friends Yicheng, Xiangyun, and Lingzhi for their companionship and support throughout this journey.

This work would not have been possible without the financial support from an NSERC-Alliance grant with Bell Textron.

Contents

List of Figures

List of Tables

Chapter 1

Introduction

1.1 Shrouded Rotor

After its first production in 1942, the helicopter has become a popular transportation vehicle under low airspeed conditions for its ability to vertically take off and land and its high hovering functionality. Over its development history, helicopters have been widely utilized in military, construction, firefighting, search, rescue, etc. (Johnson, 2013).

The noise generated by the rotors is one of the significant environmental impacts of helicopter flight. Reducing helicopter noise is essential to promoting sustainable and safe helicopter operations. As an anti-torque system that counters the torque from the main rotor, the tail rotor is one of the major noise sources during helicopter flight. After first being practically applied by French manufacturer *Sud Aviation* in the 1970s (Mouille & Bourquardez, 1970), the concept of a shrouded rotor (also called Helicopter Fenestron^{TM}) has gained considerable attention in modern rotorcraft design due to its potential to improve the aerodynamic and aeroacoustic performance of the rotor. Enclosing the rotor within a cylindrical shroud could generate additional thrust and obtain significant noise reduction (Weisgerber & Neuwerth, 2003). The shroud also provides a protective barrier, reducing the risk of accidents caused by contact with the rotor blades, which makes them desirable for human-crewed vehicles and missions operating near people or buildings.

(a) Sud Aviation SA 340 (b) EC 120B's shrouded tail rotor

Fig. 1.1: The application of shrouded tail rotor on helicopter

(a) DJI Avata (b) Airbus EVTOL

Fig. 1.2: The application of shrouded rotor on UAV and EVTOL

With the development of unmanned aerial vehicles (UAVs) and electric vertical take-off and landing vehicles (EVTOLs) in recent decades, the shrouded rotor has also been considered in the design for the same advantages.

1.2 Motivations

Over the past two decades, the aerodynamic and aeroacoustic performance of shrouded rotors in hover and axial inflow conditions has been extensively investigated. Pereira (2008), and Hrishikeshavan (2011) have experimentally and computationally proved the increase of thrust for the shrouded rotor compared with the open rotor in hover conditions. Martin & Tung (2004) performed a parametric study on the design parameters and showed that the increase of tip-gap ratio has a negative effect on the

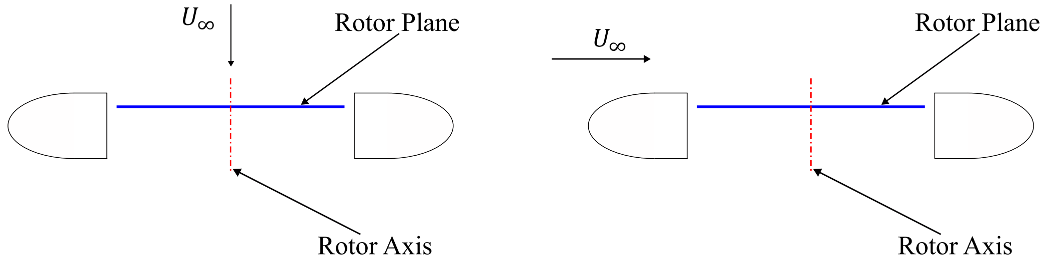

(a) Axial inflow (b) Edgewise inflow

Fig. 1.3: The schematic of axial inflow and edgewise inflow

hover performance. Zhang *et al.* (2021) computationally validated the noise reduction in hover and axial inflow conditions.

However, the shrouded rotor is not always in these two flight conditions. A helicopter's shrouded tail rotor is in an edgewise flight condition during climbing, descending, and cruising. Similarly, the shrouded rotors on UAVs and EVTOLs are also in an edgewise flight condition in their forward flight, where the inflow velocity is normal to the rotor axis (shown in Figure 1.3). The performance of the shrouded rotor is crucial during these flight conditions as it is closer to personnel on the ground. The edgewise flight condition has been less studied. Unlike hovering conditions, inflow distortion is observed for the shrouded rotor in edgewise flight, which affects the aerodynamic performance. Akturk & Camci (2010) used a combination of experimental and computational methods and showed that the inflow distortion was significantly affected by the separation bubble on the upstream shroud inlet. Misiorowski *et al.* (2019a) performed a computational study using Reynolds Average Navier-Stokes (RANS) and demonstrated that both the induced velocity of the rotor and the edgewise inflow velocity could affect the aerodynamic performances of the shrouded rotor.

During flight, a pilot has control of the rotating speed of the rotor and the climb/descend/cruise/forward flight velocity. Therefore, it would be beneficial for the pilot or the flight controller if a single parameter that combines these two velocities could help predict the performance of the shrouded rotor in edgewise flight.

This study aims to experimentally examine the effect of the rotor tip-to-edgewise velocity ratio μ on the aerodynamics performance of a shrouded rotor in edgewise flight. A shrouded rotor was designed and tested in the wind tunnel. The aerodynamic loads, the mean pressure distribution, and the velocity on the inlet plane of the shroud were measured at various μ. The turbulence spectra at the inlet of the shroud were also examined, which will be utilized in further acoustic studies.

1.3 Thesis Organization

This thesis is structured as follows: In Chapter 2, the working principle of the shrouded rotor and the previous study on its hovering and edgewise flight are presented. Chapter 3 presents the measurement techniques, apparatus, and tested shrouded rotor. Chapter 4 shows the results and discusses the key observations. Finally, Chapter 5 shows the suggested future tests that could be performed on this setup, while Chapter 6 will summarize the results obtained in this study.

Chapter 2

Background & Literature review

2.1 Shrouded Rotor in Hover

Unlike fixed-wing aircraft, rotary-wing vehicles use rotating wings to generate lift, allowing them to remain airborne without any relative velocity to the air. Therefore, helicopters possess the capability for vertical flight, including vertical take-off and landing. The ability to hover and perform vertical flight efficiently with a heavier-than-air vehicle is a fundamental characteristic of helicopter rotors (Johnson, 2013). For helicopters with conventional configuration (with main and tail rotor), under hovering flight conditions, the thrust generated by the main rotor counters the vehicle's gravity, and the thrust of the tail rotor counteracts the torque of the main rotor. Given that a rotary-wing vehicle operates a large portion of its lifespan in hovering conditions, enhancing the hovering efficiency is essential in rotorcraft design to reduce power consumption and extend the hovering duration. Other than optimizing the design of rotor blades, encasing the rotor in a cylindrical shroud is the other potential solution. Due to the difficulty of installation and the consideration of additional weight, the shrouded rotor option is commonly implemented on tail rotors rather than the main rotor. Shrouded rotors are widely installed on helicopters and UAVs because they offer improved hovering performance compared to unshrouded open rotors (Pereira, 2008). This improvement can be explained by the Actuator Disk theory.

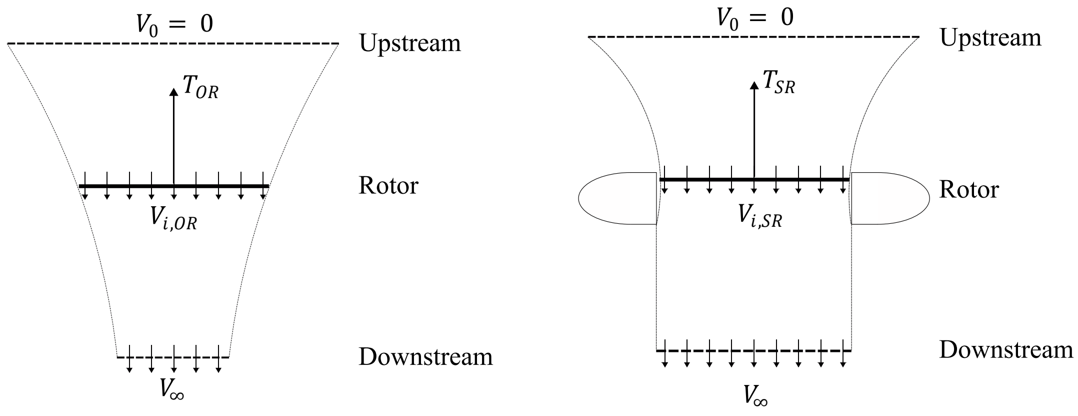

(a) Open rotor (b) Shrouded rotor

Fig. 2.1: Open rotor and shrouded rotor

The Actuator Disk theory (or the Momentum theory), originally developed by Rankine (Rankine, 1865) and Froude (Froude, 1889), was used to derive the thrust and induced power of an open rotor in hover. In this theory, the rotor is treated as an actuator disk of diameter D_r with area $A_r = \pi D_r^2/4$. The flow is assumed to be one-dimensional with velocity parallel to the rotor axis only, with no variation with respect to radial location. Under the hovering condition, the velocity far upstream of the rotor is $V_0 = 0$. The velocities above and below the rotor are assumed to be $V_1 = V_2 = V_{i,OR}$, where the subscript OR stands for the open rotor, and the velocity far downstream is V_∞. Since the rotor thrust is the only force acting on the fluid, from the conservation of momentum, the open rotor thrust T_{OR} is

$$T_{OR} = \dot{m} V_\infty, \tag{2.1}$$

where $\dot{m}$ is the mass flow rate. With the conservation of energy, the induced power of the rotor equals the change of kinetic energy of the flow

$$T_{OR} V_{i,OR} = \frac{1}{2} \dot{m} V_\infty^2. \tag{2.2}$$

Combining Equation (2.2) and Equation (2.1), the induced velocity is

$$V_{i,OR} = \frac{1}{2}V_\infty = \sqrt{\frac{T_{OR}}{2\rho A_r}}. \tag{2.3}$$

The induced power of the open rotor could also be expressed as

$$P_{i,OR} = \frac{T_{OR}^{3/2}}{\sqrt{2\rho A_r}}\ . \tag{2.4}$$

In this theory, the velocity far downstream of the open rotor V_∞ is twice the induced velocity V_i (Johnson, 2013). According to the conservation of mass

$$\dot{m} = \rho A_r V_i = \rho A_\infty V_\infty, \tag{2.5}$$

the cross-section of the slipstream A_∞ is half of A_r. This decrease in the cross-section area and increase in wake velocity is referred to as the Vena Contracta effect (Leishman, 2006).

By encasing a cylindrical or diverging shroud around the rotor, the flow downstream of the rotor stays attached to the shroud's inner surface, which indicates that the cross-section area of the slipstream can be forced to maintain constant or even increase (Pereira, 2008). The Momentum Theory for the ducted rotor is shown in Figure 2.1b. The exit area of the shroud is A_e, and the flow is assumed to be fully accelerated at the exit of the shroud, which means $V_e = V_\infty$. Other assumptions are the same as the open rotor case. The ratio between the exit and rotor disk areas is defined as the expansion ratio $\sigma_d = A_e/A_r$. Then, from the conservation of mass,

$$V_\infty = \frac{1}{\sigma_d}V_i. \tag{2.6}$$

With the conservation of momentum, the shrouded rotor thrust T_{SR} could be obtained as

$$T_{SR} = \frac{1}{\sigma_d}\rho A_r V_i^2. \tag{2.7}$$

The subscript SR represents the parameters for the shrouded rotor. The induced velocity and induced power can be expressed as

$$V_i = \sqrt{\frac{\sigma_d T_{SR}}{\rho A_r}}, \tag{2.8}$$

$$P_{i,SR} = \frac{1}{2}\rho A_r V_i V_\infty^2 = \frac{T_{SR}^{3/2}}{\sqrt{4\sigma_d \rho A_r}}. \tag{2.9}$$

From Equation (2.4) and Equation (2.9), the ratio between the shrouded rotor thrust and the open rotor thrust when consuming the same amount of power is

$$\frac{T_{SR}}{T_{OR}} = (2\sigma_d)^{1/3}. \tag{2.10}$$

Both the shroud and the rotor contribute to the thrust of the shrouded rotor. The actuator disk model is used to derive the expression of the thrust provided by the rotor alone. When assuming a certain velocity at the far wake for both open and shrouded rotors, the fraction of rotor thrust T_r to the total thrust T_{SR} is

$$\frac{T_r}{T_{SR}} = \frac{1}{2\sigma_d}. \tag{2.11}$$

For the shrouded rotor, $\sigma_d > 1$, which means $T_{SR}/T_{OR} > 1$, and a shrouded rotor provides greater thrust in hover than the same rotor in open rotor configuration when consuming the same amount of power. This also indicates that the shrouded rotor has higher hovering efficiency than the open rotors, with the ratio of the figure of merit (FM) shown as

$$\frac{FM_{SR}}{FM_{OR}} = \sqrt{2\sigma_d}. \tag{2.12}$$

Hrishikeshavan (2011), Akturk & Camci (2011), and Zhang *et al.* (2021) have compared the performance of shrouded and open rotors and proved this efficiency improvement. The wake velocity profile measurement from Yilmaz *et al.* (2015) have shown the reduction of slipstream contraction and proved its effect on efficiency enhancement.

The presence of the shroud reduces the strength of the tip vortices of the rotor, which also contributes to efficiency improvement. At the tip of the rotor, the pressure difference across the blade tip drives a tip leakage flow from the pressure side to the suction side, forming a vortical flow. Similar to a finite wing, the downwash causes a reduction of the effective angle of attack and leads to a decrease in thrust and an increase in drag in the form of induced drag (Anderson, 2011). Higher induced power would be required to produce the same amount of thrust. Oweis *et al.* (2006) has examined the vortical flow in the tip region of an open and a ducted three-bladed rotor using particle imaging velocimetry (PIV). It is shown that the presence of the duct reduces the strength of the tip vortex and gives rise to efficiency improvement.

In the past decades, extensive research efforts have been conducted further to improve the hover efficiency of the shrouded rotor. Beyond the rotor's geometry, various design parameters of the shroud could affect the hovering performance of the shrouded rotor. Equation (2.12) shows that the hovering efficiency enhances with the increase of σ_d. Table 2.1 presents the results from various studies. It is clear that the measured improvement of FM does not match the theoretical expectations, indicating that other geometric parameters, namely the tip-gap ratio and the inlet lip radius, also have an impact on the performance (Qian *et al.*, 2022).

The rotor diameter is always smaller than the inner diameter for a shrouded rotor, leaving a gap between the tip and the shroud's inner surface. The tip-gap ratio is defined as

$$\delta_d = \frac{D_i - D_r}{D_i} \ , \tag{2.13}$$

where D_i is the diameter of the shroud's inner surface, and D_r is the rotor diameter. The tip-gap ratio affects the tip leakage (tip vortex) of the shrouded rotor, which eventually affects the hovering thrust and efficiency. Martin & Tung (2004) exper-

Table 2.1: Effect of expansion ratio on FM improvement

Author	Expansion Ratio	Theoretical %	Actual %
Misiorowski *et al.* (2018)	1	41	26
Akturk & Camci (2011)	1.12	50	30
Jimenez & Singh (2015)	1.32	62	27
Zhang *et al.* (2021)	1.41	68	57

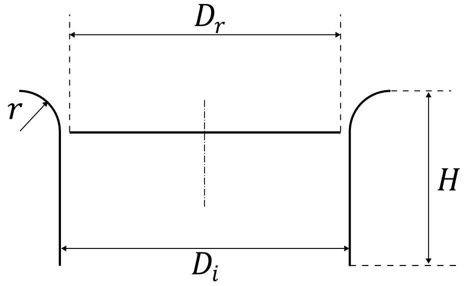

Fig. 2.2: Shrouded rotor parameters

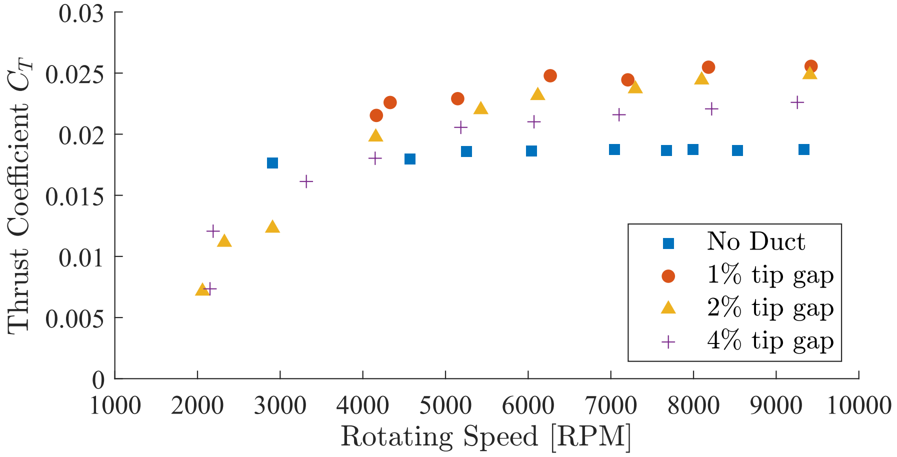

Fig. 2.3: Thrust variation with RPM and tip-gap ratio, adapted from Martin & Tung (2004)

imentally tested the shrouded rotor with different tip-gap ratios and compared the results with the open rotor. As shown in Figure 2.3, the presence of a duct has a negative effect on the hovering thrust at lower rotating speed as viscous losses inside the duct diminish the thrust produced by the duct. Whereas, at higher rotating speed, the duct improves the hovering thrust, and the increase of δ_d causes the thrust to decrease. Akturk & Camci (2011) studied the shrouded rotor with various tip-gap ratios using computational methods and showed that a larger δ_d leads to a larger tip leakage, which reduced the thrust generated near the tip of the blades. By increasing δ_d from 1.71% to 5.17%, a drop of up to 18% on the figure of merit could be observed.

The shroud lip geometry is also an influential factor in hovering performance. For a circular duct lip, a larger lip radius significantly minimized the inlet lip flow separation, thus improving the hovering figure of merit and extending the blade tip flow separation or stall to an even higher thrust level. Sheng *et al.* (2015) performed an experimental parametric study on the shrouded rotor and showed that an increase in the normalized inlet lip radius r/D_i from 4.17% to 8.33% could increase the figure of merit by up to 8%. Cao *et al.* (2021), and Cao *et al.* (2023) performed a numerical simulation on a shrouded tail rotor using a high-fidelity Reynolds-Averaged Navier-Stokes (RANS) solver and investigated the effect of lip radius on the hovering performance. The results indicate that reducing lip radius will increase the peak value of negative pressure in the lip region and make the peak move toward the duct inlet, but the duct with a sharp lip will lose its ability to provide enough thrust. Hrishikeshavan & Chopra (2012) has compared the hovering performance of shrouded rotor with circular lip and elliptical lip and concluded that higher power consumption is necessary to obtain the same amount of thrust.

2.2 Shrouded Rotor with Axial Inflow

During the vertical climbing/descending of UAVs, the shrouded rotors operate with an axial inflow, where the rotor axis is parallel to the freestream direction. Under this flight condition, the advance ratio, defined as $J = \frac{U_\infty}{nD_r}$, is the key factor for the aerodynamic performance. According to the blade element theory, the increase in inflow velocity decreases the effective angle of attack and eventually reduces the rotor thrust (Johnson, 2013). Pereira (2008) measured the shrouded rotor with different advance ratios and found that the thrust coefficient shows a descending trend with the increase of J. Compared with an open rotor, the shrouded rotor exhibits a faster decrease in thrust, indicating that the shroud negatively affects the performance in this flight condition (Jimenez & Singh, 2015). The increase in inflow velocity also reduces the power consumption at a certain rotating speed. The results provided by Yilmaz *et al.* (2015) showed that the efficiency $\eta = \frac{C_T J}{C_P}$ increases at a low advance ratio and decreases at a higher one.

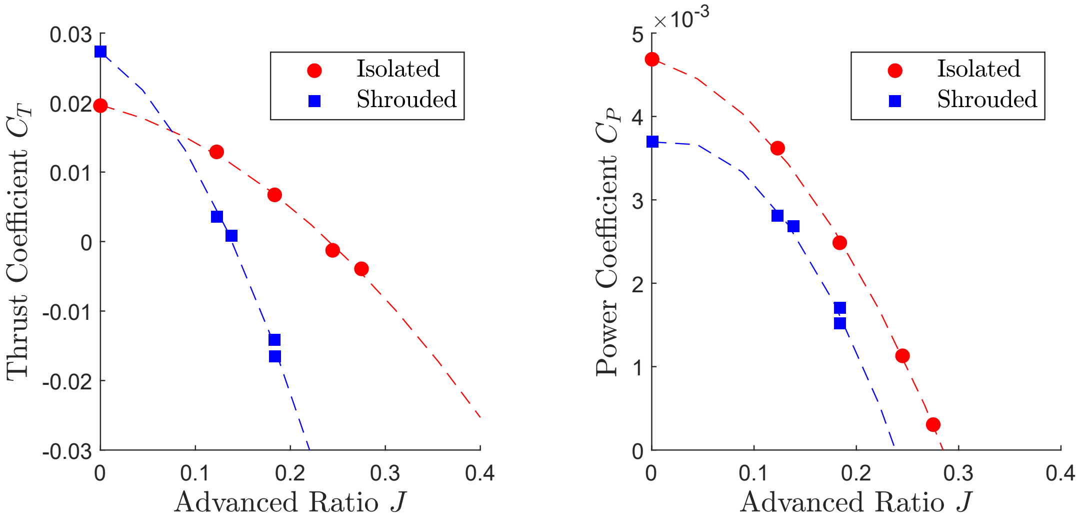

(a) Thrust coefficient C_T (b) Power coefficient C_P

Fig. 2.4: Thrust and power coefficient for shrouded rotor with axial inflow at different advance ratio J (Pereira, 2008)

2.3 Shrouded Rotor in Edgewise Flight

During the helicopter's climbing/descending/cruising period and the forward flight of UAVs, the inflow velocity is perpendicular to the rotor axis. For an open rotor under this flight condition, the blades on the advancing side encounter a velocity exceeding Ωr, while those on the retreating side experience a velocity lower than Ωr. In a part of this side, the flow is in the reverse direction (as shown in Figure 2.5a). The helicopter's main rotor uses cyclic pitch control to mitigate the effect of this reverse flow region. However, the tail rotor, which only has collective pitch control, and UAV rotors, which typically have fixed pitch, experience uneven thrust distribution on the two sides, resulting in a rolling moment.

Glauert (1935) provided the Momentum theory for rotors operating in oblique inflow with velocity U_∞ and incidence angle α. The resultant thrust force of the rotor is

$$T_{edgewise} = 2\rho A_r V_i \sqrt{U_\infty^2 + 2U_\infty V_i \sin\alpha + V_i^2}, \tag{2.14}$$

where V_i is the axial induced velocity on the rotor. In edgewise flight, $\alpha = 0°$, which means that

$$T_{edgewise} = 2\rho A_r V_i \sqrt{U_\infty^2 + V_i^2}. \tag{2.15}$$

From Equation (2.15), it is clear that edgewise velocity U_∞ affects the thrust in this flight condition and that the thrust is lowest for this angle.

During edgewise flight, the presence of a shroud distorts the flow at the inlet. The rotor redirects the flow from the edgewise direction to the axial direction. In the flow visualization shown by Halwick (2012), flow separation can be observed behind the front lip of the shroud. Misiorowski *et al.* (2019a) computationally studied the flow physics of a ducted rotor in edgewise flight by implementing a Spalart-Allmaras RANS model. Compared with the hovering case, the resultant velocity field of the edgewise flight case (Figure 2.6) shows an upwash region formed inside the shroud near the front of the duct. Additionally, recirculation and vortices could be observed near the rotor plane. In hover conditions, the velocity field on the center plane is symmetric about the axis. In edgewise flight, the velocity below the rotor plane became asymmetric and is higher in the region near the rear end.

The flow distortion generates an uneven elemental thrust distribution in the front and rear halves of the rotor (Figure 2.7). The higher elemental thrust at the front end

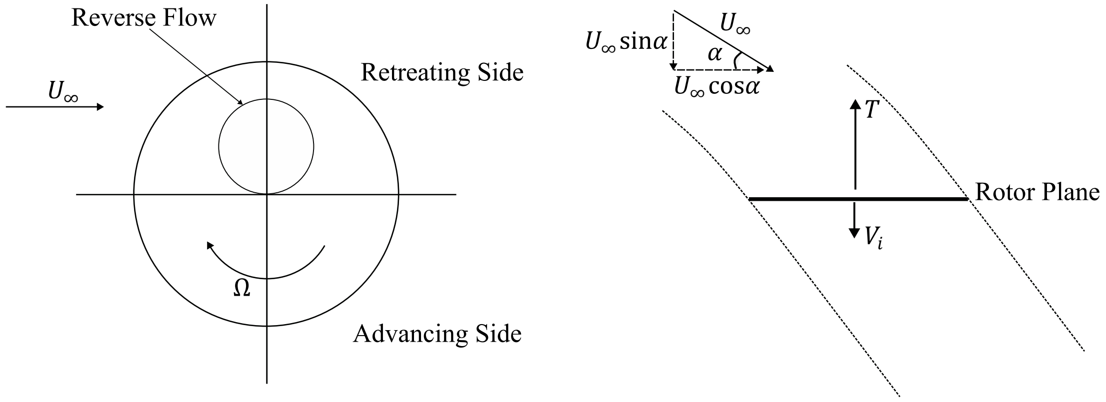

(a) Advancing side and retreating side (b) Momentum theory flow model

Fig. 2.5: Edgewise flight with open rotor

eventually creates a nose-up pitching moment on the shrouded rotor in edgewise flight. Similar to the open rotor in edgewise flight, the elemental thrust on the advancing side is higher than the retreating side. When maintaining a constant rotational speed, an increase in U_∞ results in a greater elemental thrust in the front portion of the rotor, indicating that the pitching moment also increases with edgewise velocity.

The pressure distribution on the shroud's inner surface could also reflect the flow separation at the front and the redirection effect. When the rotor is not spinning, the shroud encloses a circular cylindrical cavity with openings on top and bottom. In this scenario, the flow separation occurs at the front end of the shroud, and the flow slightly turns and enters the cavity. Consequently, the pressure near the rear end is higher than in another region (Hiwada *et al.*, 1983). McCarthy & Ekmekci (2022) and Marsden *et al.* (2012) have shown that the pressure distribution on the cavity inner surface depends only on the height over diameter ratio H/D_i and is independent of inflow velocity.

When the rotor starts rotating, it induces the inflow and further redirects the edgewise inflow to the axial direction. This redirect effect creates a high-pressure stagnation region at the rear end on the shroud's inner surface, and the depth of this stagnation region varies with the edgewise velocity and induced velocity of the rotor

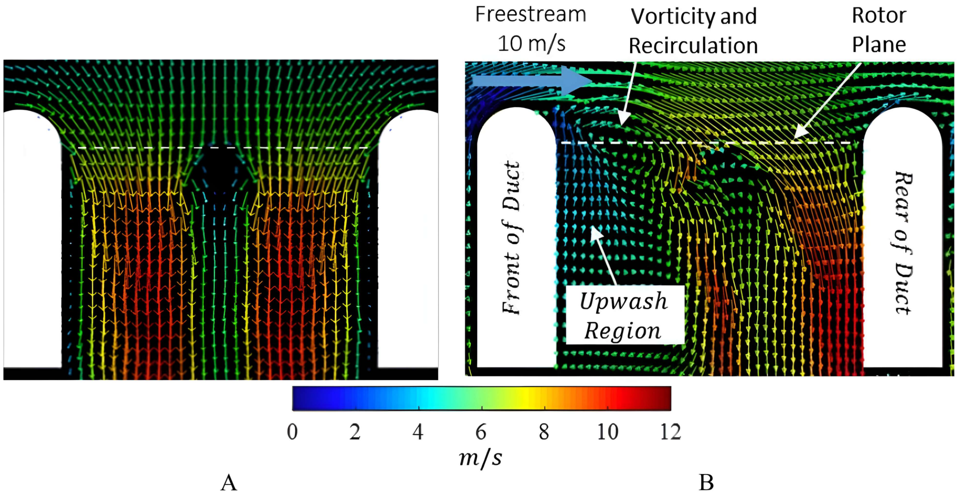

Fig. 2.6: The velocity vectors on the center plane A: Hover; B: Edgewise $U_\infty = 10$ m/s, rotates at 3500 RPM (Misiorowski *et al.*, 2019a)

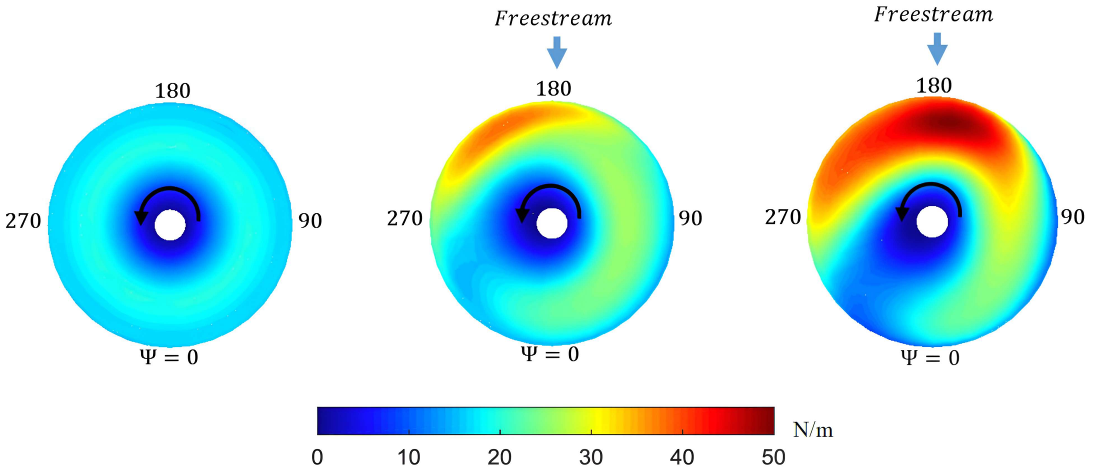

A B C

Fig. 2.7: The elemental thrust distribution on rotor for A: Hover; B: Edgewise $U_\infty =$ 5 m/s; C: Edgewise $U_\infty = 10$ m/s, with rotating speed of 3500 RPM (Misiorowski *et al.*, 2019a)

.

(Misiorowski *et al.*, 2019a). This ram pressure is an additional source of drag for the shrouded rotor in edgewise flight, as it acts in the same direction as the inflow. This pressure drag force could be calculated by integrating the pressure force on the shroud's inner surface. According to the shroud surface pressure measurement shown in Pereira & Chopra (2006) and Yilmaz *et al.* (2015), the pressure at the rotor plane is lower than at other depth locations, which is caused by the high-velocity air leaking through the gap between the blade tips and the shroud wall.

The aerodynamic loads on the shrouded rotor in edgewise flight, including the thrust, drag, and pitching moment, could be affected by the edgewise inflow velocity and the rotating speed of the rotor. Similar to the hovering condition, the rotor and the duct contribute to the total thrust. The thrust decomposition from Misiorowski *et al.* (2019a) demonstrated that both rotor and duct thrust increase with rising edgewise velocity, and the portion of rotor thrust decreased with edgewise velocity. Hrishikeshavan & Chopra (2012) experimentally measured the incremental rotor drag force and pitching moment generated by the edgewise inflow. Their findings indicate that, compared to an unshrouded rotor, the change in drag with edgewise velocity is

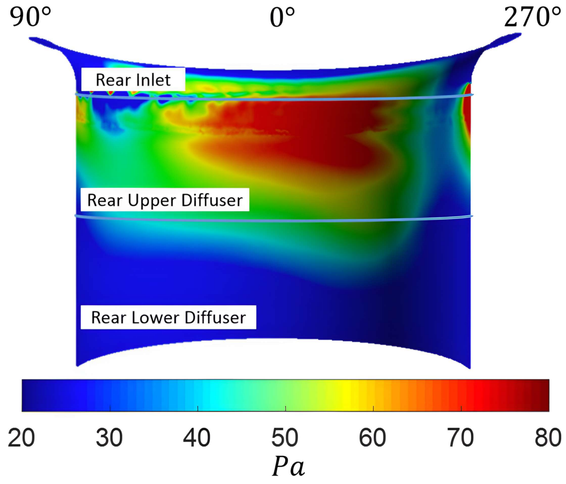

Fig. 2.8: The ram pressure distribution on the shroud's inner surface in edgewise flight with $U_\infty = 10$ m/s, with a rotating speed of 3500 RPM (Misiorowski *et al.*, 2018)

.

more pronounced for the shrouded rotor. Additionally, they showed that the pitching moment increases with both the edgewise inflow velocity and the rotating speed.

Geometric parameters are also crucial factors in the shrouded rotor performance in edgewise flight. Akturk & Camci (2010) measured the total pressure at the exit of the rotor using an array of Kiel probes for the ducted rotor with various tip-gap ratios. Similar to the hovering condition, a smaller tip gap reduces the tip vortex, causing an increase in the total pressure and indicating a higher thrust in edgewise flight. The distortion at the inlet and the lip separation causes the pressure loss in the leading side ($\theta = 0°$), which increases with the edgewise flight velocity. Another pressure loss region could also be observed near the hub and is not dependent on the tip clearance. When keeping the tip clearance constant, the pressure loss at the tip and hub became more significant as the edgewise velocity increased.

Graf *et al.* (2008) found that the leading edge geometry of the shroud inlet is a significant factor for the aerodynamic characteristics of the shrouded rotor. By comparing the shrouded rotor with five different lip geometries, they concluded that the lip shape benefits hovering performance could have a negative effect on the edgewise flight performance. Hook *et al.* (2011) performed experiments on a ducted fan and used flow visualization techniques to confirm that altering the inlet design could reduce the separation region. Akturk & Camcı (2014) developed a double ducted fan design and performed a CFD study on its performance. Their investigation revealed that the double duct design acts as a duct inlet separation control device, which could improve the mass flow rate passing from the duct by 40 % and improve the thrust force obtained from the ducted fan by 56 % relative to the baseline duct in edgewise flight conditions.

The shroud height below the rotor is defined as the diffuser length, and is another important factor of shrouded rotor performance in edgewise flight. Misiorowski *et al.* (2019b) performed a computational parametric study on the diffuser length. The resultant velocity field showed that the flow separation area inside the diffuser and the wake impinging at the rear are larger for the shroud with a longer diffuser length. The thrust of the shrouded rotor is insensitive to the diffuser length. However, as the diffuser length decreases, the elemental thrust increases at the front and decreases at the rear, generating a higher nose-up pitching moment.

2.4 Shrouded Rotor Acoustics

With the increased popularity of vertical takeoff and landing aerial vehicles, the noise produced by rotating blades has been of global scientific interest (Christian & Cabell, 2017). Aeroacoustic measurements on rotary-wing systems were initially conducted by (Gutin, 1948). They showed that the rotary-wing system generates complex sound patterns characterized by varying frequencies and intensities. Rotating blades emit two distinctly different types of acoustic signatures. The first is referred to as tone or harmonic noise and is caused by sources that repeat themselves exactly during each rotation. The second is broadband noise, which is a stochastic, non-periodic signal caused by turbulent flow over the blades (Glegg & Devenport, 2017). The tonal noise is due to the blade's steady force, periodic blade load fluctuations due to blade-vortex interactions, and other periodic blade loading variations (Schmitz & Boxwell, 1976). Broadband noise is significantly contributed to by both turbulent boundary-layer trailing-edge noise and turbulence ingestion noise at the leading edge, and the boundary-layer interactions of the rotor blade with its wake (Jordan *et al.*, 2020; Grande *et al.*, 2022).

An anechoic chamber or wind tunnel is necessary for acoustic measurements to avoid the influence of reflected noise from the wall and the noise from wind tunnel fans. The rotor noise measurement is mainly conducted by arrays of microphones, which have the capability of capturing high-frequency pressure fluctuations. The sound pressure level (SPL) is the main measure of noise and is presented in terms of the frequency-dependent energy content of pressure fluctuations, which is defined as

$$SPL = 10log_{10}(\frac{\phi_{pp}}{p_{ref}^2}). \tag{2.16}$$

ϕ_{pp} is the power spectral density of the measured far-field pressure fluctuations, and p_{ref} is the reference sound pressure. SPL in decibels (dB) shows the noise intensity, with higher SPL indicating more significant noise. In acoustic measurements, microphones are placed at different azimuthal angles around the rotor in order to characterize the propagation of the noise in different directions.

For an open rotor, the inflow angle affects the acoustic performance. Yang *et al.* (2020) conducted an experimental study of a tilted rotor at a constant rotating speed. They showed that increasing the freestream velocity and decreasing the tilting angle intensify the tonal and broadband noise components. Jamaluddin *et al.* (2024) further studied the tilt rotors in edgewise inflow conditions with far-field microphones and PIV flow measurements. The results reveal that a lower tilting angle causes an increase of turbulence energy in the flow and increases the noise of the rotor. The ingestion of atmospheric turbulence into the blade causes turbulence ingestion noise, which is another essential source of broadband rotor noise (Zawodny *et al.*, 2016).

With rotor noise gaining increasing consideration, noise reduction techniques have become a major topic for rotorcraft development. Since all rotor noise mechanisms have a strong velocity dependence, a primary noise reduction technique is the reduction of rotor tip speed. A trade-off for this noise reduction is the reduction of the rotor performance (George, 1978). The shrouded rotor shows the potential of reducing the tail rotor noise while maintaining or even enhancing its operation performance. Enclosing the rotor with a shroud influences the tonal noise generated

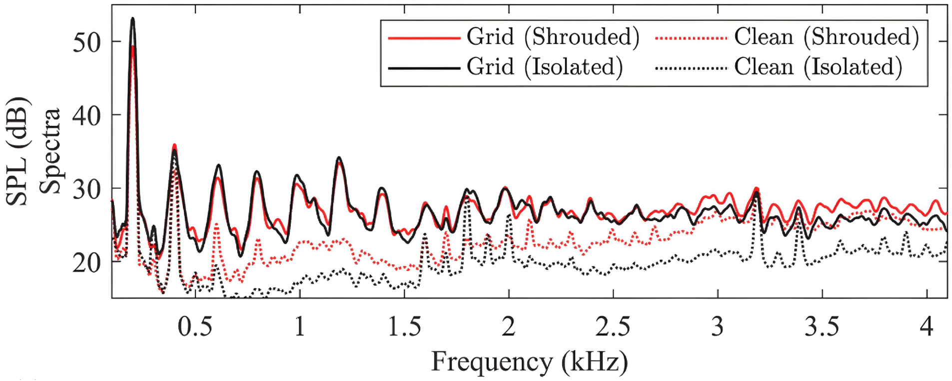

Fig. 2.9: The comparison of SPL spectra for shrouded and isolated rotor with turbulent inflow and clean inflow, adapted from Go *et al.* (2023b)

by the rotor. Lakshminarayan & Baeder (2011) have shown that the shroud altered the steady load, thereby changing the steady loading sources of the rotor blades. Malgoezar *et al.* (2019) experimentally tested the shrouded and isolated rotor at the same rotating speed in an open jet anechoic wind tunnel. From the SPL spectra, they demonstrated that the presence of the shroud caused the absence of the high tonal peaks shown in the open rotor measurements and produced a higher broadband noise level. Go *et al.* (2023a) experimentally and numerically investigated the tonal noise produced by the shrouded rotor in static conditions. The results showed that the shroud reduces the load on the rotor, resulting in a lower tone noise level than the open rotor. From the pressure measurements on the shroud's inner surface, they found that the tonal noise generated by the shroud wall close to the blade tip interfered with the noise radiated from the loading source on the rotor blades, which reduced the noise level below the rotor plane.

The inflow affects the noise generation and propagation of the shrouded rotor. Go *et al.* (2023b) performed an acoustic study on the shrouded rotor with turbulent inflow produced by a passive grid in the axial direction. The flow properties were examined by a hot-wire located upstream of the rotor. The SPL comparison (Figure 2.9) showed that the broadband and tonal components are higher when the rotor operates with turbulent inflow than in clean inflow.

The geometry of the shrouded rotor influences the noise emitted. Canepa *et al.* (2016) has experimentally tested the effect of tip leakage on the noise of the shrouded rotor and stated that the main effect of the tip leakage is a modification in the low-frequency part of the SPL spectrum, including an increase of broadband noise. Jang *et al.* (2003) implemented hot-wire measurements near the tip region of the blades and showed that the tip vortex of the blades is enlarged by the larger tip clearance, inducing the acceleration of the through flow, thus increasing the broadband noise.

2.5 Thesis objectives

Most existing literature about the shrouded rotor focused on the effect of shroud and rotor geometry on performance. Within these studies, the shrouded rotor was only examined at a few discrete inflow velocities and rotating speeds, and the full picture of how these two flight parameters affect the performance was not mentioned. Similar to the axial inflow scenario, edgewise flight performance may also be related to a ratio between these two factors. Therefore, we hypothesize that the non-dimensional tip-to-edgewise velocity ratio could be a decisive parameter for edgewise flight performance. The aim of this thesis is to give a full picture of the effect of the tip-to-edgewise velocity ratio

$$\mu = \frac{V_{tip}}{U_\infty} = \frac{\Omega R_r}{U_\infty} \tag{2.17}$$

on the aerodynamic performance of a shrouded rotor in edgewise flight conditions. A shrouded rotor is designed and tested experimentally in a low-speed wind tunnel. The following aspects are measured and analyzed at various μ:

- the aerodynamic loads acting on the shrouded rotor;
- the mean pressure distribution on the shroud's inner surface;
- the velocity field on the shroud's inlet and outlet;
- the turbulence intensity at the inlet and outlet.

From the high-frequency velocity measurements, the turbulence spectra at different locations on the inlet plane are also obtained and analyzed, which characterizes the turbulence ingestion into the rotor. This information could be utilized for further acoustic analysis.

Chapter 3

Experimental Apparatus & Procedure

In this chapter, the details of the shrouded rotor testing setup and the installed apparatus will be introduced. The rotor is enclosed in an annular-shaped shroud and placed in a low-speed laminar wind tunnel. Various measurement apparatuses were implemented to characterize the aerodynamic performance of the shrouded rotor and the flow around it. The aerodynamic loads, inner surface pressure, and shroud inlet/outlet velocity were assessed across various velocity ratios.

3.1 Wind Tunnel

Experiments were performed in the Newman tunnel in the Aerodynamics Lab at McGill University. The Newman Wind Tunnel is an open circuit tunnel with a rectangular, closed test section with a cross-section of 2 ft × 3 ft and a length of 9ft. A Pitot-static tube connected to a differential pressure sensor was placed in the test section to measure the flow velocity in the tunnel.

The freestream speed U_∞ in the test section follows a linear relation with the rotating speed of the fan assembly. In the experiments, the fan was run from 150 RPM to 400 RPM, giving a freestream velocity $U_\infty \in [5.22, 15.13]$ m/s

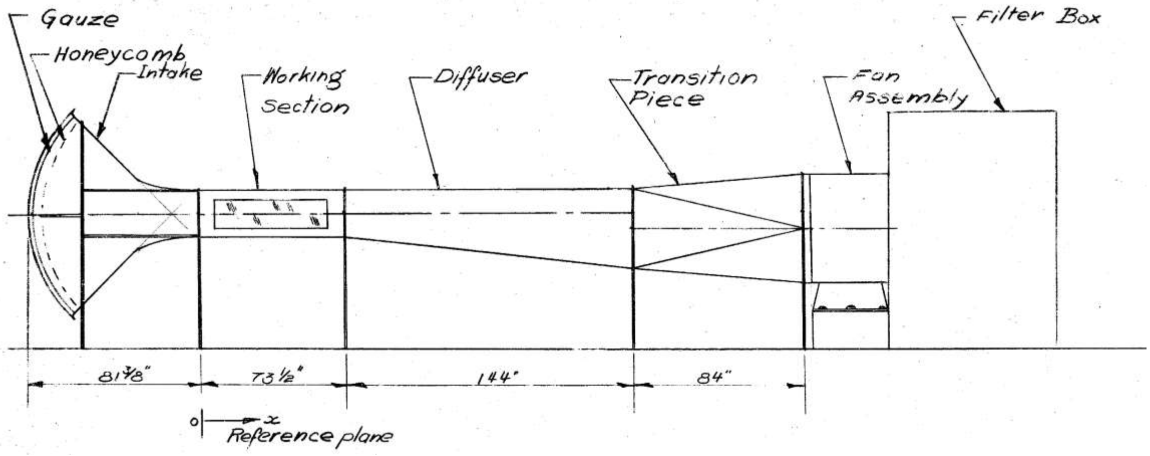

Fig. 3.1: Schematic of Newman wind tunnel, Wygnanski & Newman (1961)

3.2 Setup Design

3.2.1 Rotor & Stator

In all the following experiments, the ISAE 4-bladed rotor was used. This rotor was designed and previously tested by ISAE-Supaero (Gojon *et al.*, 2021). The original version has a diameter of 250 mm. The rotor features a constant twist angle of 10° along the blades and has a NACA 0012 profile with a chord length of 25 mm on all the radial stations of the blades. Restricted by the size of the wind tunnel test section, the rotor was scaled by a ratio of 1:1.667 to avoid the wall effect and ground effect. After scaling, the tip diameter of the rotor is $D_r = 150$ mm. Detailed rotor dimensions are shown in Table 3.1. To ensure the tightness of the rotor and prevent the rotor shoot-out during experiments, four M2 counter-bore holes were added to the hub, and four M2×10 Hex-head screws were used to attach the rotor to the motor. The hub diameter was set to 19.6 mm, the same as the diameter of the motor's top surface.

The stator used in the setup has six blades with a NACA 0024 profile. The stator blade has 0° angle of attack to the rotor axial direction. The tips of the stator blades are connected to an annular ring, which could then be attached to the inner shroud with M2×6 flat head screws. The motor is attached to the stator hub using four

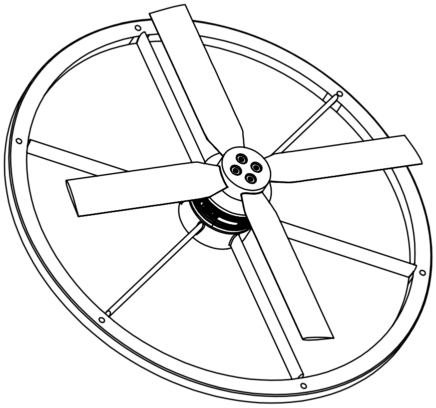

Fig. 3.2: The assembly of rotor, motor, and stator

M3×12 flat head screws. The detailed dimension of the stator is shown in Table 3.1. Figure 3.2 shows the rotor, motor, and stator assembly.

3.2.2 Shroud

The annular shroud comprises two components: the inner shroud and the outer shroud. The outer shroud has a half-elliptic cross-section to reduce the flow separation. The inner shroud encloses a cylindrical cavity with a diameter of $D_i = 156$ mm and a height of $H = 35$ mm. This gives a tip gap ratio of 4% and a H/D_i ratio of 22.4%. Other detailed dimensions are listed in Table 3.2. Drawings for shroud parts are shown in Appendix A.

The shroud is hollow to enable the pressure measurement on the shroud's inner surface. The space inside the shroud is reserved for the rubber tubes that connect the pressure taps and the pressure scanner. Two rectangular slots are designed on

Table 3.1: Dimensions of rotor and stator

Rotor		**Stator**	
Chord	15 mm	Chord	7.6 2mm
Hub Diameter	19.6 mm	Hub Diameter	27.9 mm
Hub Thickness	7.2 mm	Hub Thickness	10.2 mm
Twist Angle	10°	Angle of Attack	0°

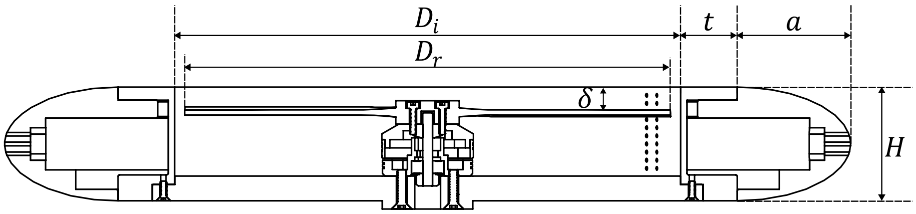

Fig. 3.3: The cross-section view of the shrouded rotor with dimensions

the outer shroud to allow the rubber tubes to come out of the shroud. The two outer shroud parts are attached to the supporting plates using four M5×12 low-profile socket head screws.

On the leading edge of the outer shroud parts, five pressure taps are designed to check the alignment of the setup with respect to the inflow (shown in Figure 3.4). Perfect alignment could be obtained if the stagnation point is at position 5 ($c_p = 1$). Due to the symmetry of the semi-elliptic shape, there should be no pressure difference between 2, 4, and 1, 3.

To enhance the resolution of the pressure measurement, the inner shroud can rotate 360° and can be fixed at 36 different angular positions. Additionally, to maintain the stator blade angle relative to the edgewise flow, the stator itself is also rotatable relative to the inner shroud and can be locked at various angular positions.

Table 3.2: Dimensions of the shrouded rotor

Notation	**Dimension**	**Notation**	**Dimension**
D_i	156mm	H	35mm
D_r	150mm	a	35mm
H/D_i	0.224	t	17.5mm
$(D_i - D_r)/D_i$	0.04	δ	7mm

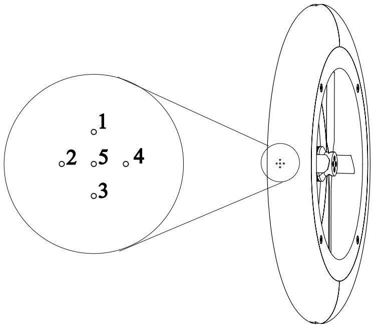

Fig. 3.4: Pressure taps for alignment check

3.2.3 Motor and Electric Speed Controller

A KDE-Direct 2304XF-2350 brushless motor is used to rotate the four-bladed rotor. The motor was powered by a 15V DC power supply. A Sitela BL20A electric speed controller (ESC) was implemented to control the rotating speed of the rotor. The ESC converts 50 Hz pulse-width modulated (PWM) duty cycle signals from the counter on the NI-USB 6363 data acquisition unit into a percentage throttle signal to the motor. The ESC needs to be calibrated before the first experiment, and the LabVIEW program *Calibrate ESC.vi* is used in the calibration process.

The LabVIEW program *=Shrouded_Rotor_Test=.vi* controls the rotation of the rotor and data acquisition. Once the ESC is calibrated, with the throttle setting from 4% to 12%. At a certain throttle, the power consumption of the motor remains constant. With this setup, the rotor could rotate from 3000 RPM to 7700 RPM.

3.2.4 Rotating Speed Measurement

During measurements, the drag force and axial torque on the rotor blades vary with inflow conditions, causing a change in rotating speed at the same throttle setting. Therefore, a rotating speed-measuring device is necessary. Similar to the working principle of the tachometer, a laser pen, and a four-terminal Uxcell photosensitive diode sensor are installed to measure the rotating speed of the rotor. A 5V DC power is connected to the diode sensor, and the NI-USB 6363 data acquisition unit reads the voltage output. When the diode sensor detects the light from the laser, a

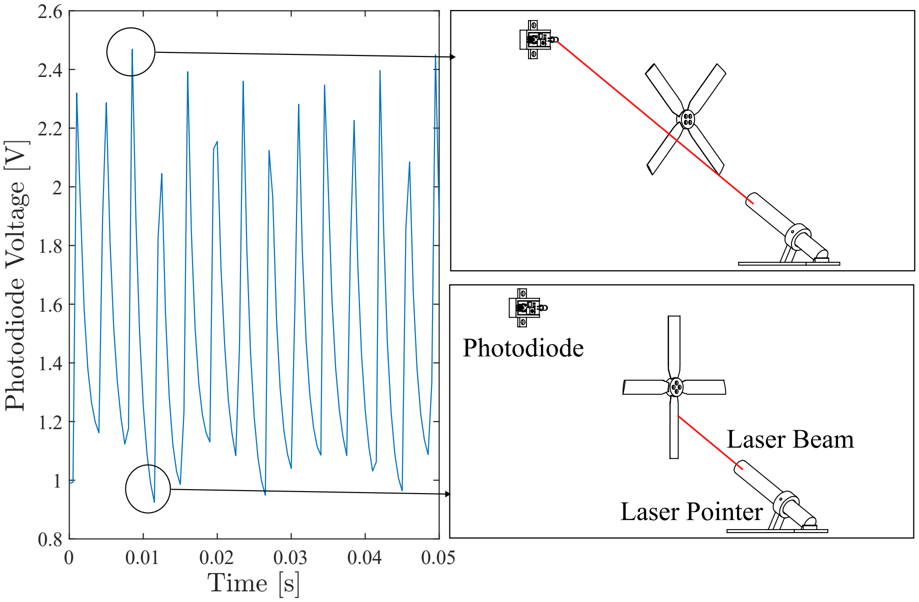

Fig. 3.5: Laser pointer and photosensitive diode sensor setup for rotating speed measurement

high voltage level can be measured. As shown in Figure 3.5, when the rotor rotates, the laser is periodically blocked by the rotor blades, causing the voltage to switch periodically between high and low levels. The signal was stored and analyzed using Fast-Fourier Transforms (FFT). From the frequency spectra shown in Figure 3.6, the spikes referred to as the blade passing frequency and its harmonics, and the rotating speed of the rotor in RPM can be obtained by

$$RPM = 60(\frac{BPF}{4}) \tag{3.1}$$

In the experiments, the maximum rotating speed is less than 10000RPM, which gives a BPF of 667 Hz. The sampling frequency should, therefore, be higher than 1333 Hz to prevent aliasing - the misidentification of frequencies in spectra due to insufficient sampling rate. In the aerodynamic load measurements and pressure measurements, the sampling frequency is set to 2000 Hz. In velocity measurements, the sampling frequency was set to 20 kHz to match the sampling rate of the hot-wire sensor.

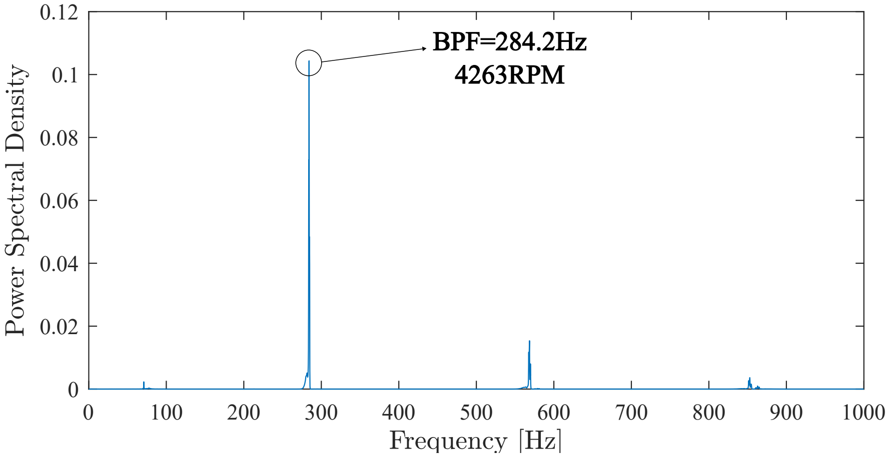

Fig. 3.6: Get BPF and rotating speed by applying FFT to voltage data

3.3 Experiment 1: Aerodynamic Loads Measurements

In hovering conditions, the thrust and torque on the rotor are the only two aerodynamic loads acting on the shrouded rotor. In edgewise flight conditions, an extra drag, a pitching moment, and a rolling moment are also expected.

The setup was placed on an ATI Gamma IP68 six-axis force/torque sensor (F/T sensor) to measure the aerodynamic load acting on the shrouded rotor. The F/T sensor provides voltage data in a 6×1 matrix for each sample, which can be converted into force components (F_x, F_y, F_z) and torque components (M_x, M_y, M_z) by applying a calibration matrix of size 6×6. Figure 3.7 illustrates the experimental setup and coordinate configuration. The aerodynamic Thrust (T), Drag (D), Pitching Moment (M_{Pitch}), and Rolling Moment (M_{Roll}) are defined as

$$\begin{aligned} T &= -F_y; \\ D &= F_x; \\ M_{Pitch} &= M_z; \\ M_{Roll} &= -F_y L - M_x. \end{aligned} \tag{3.2}$$

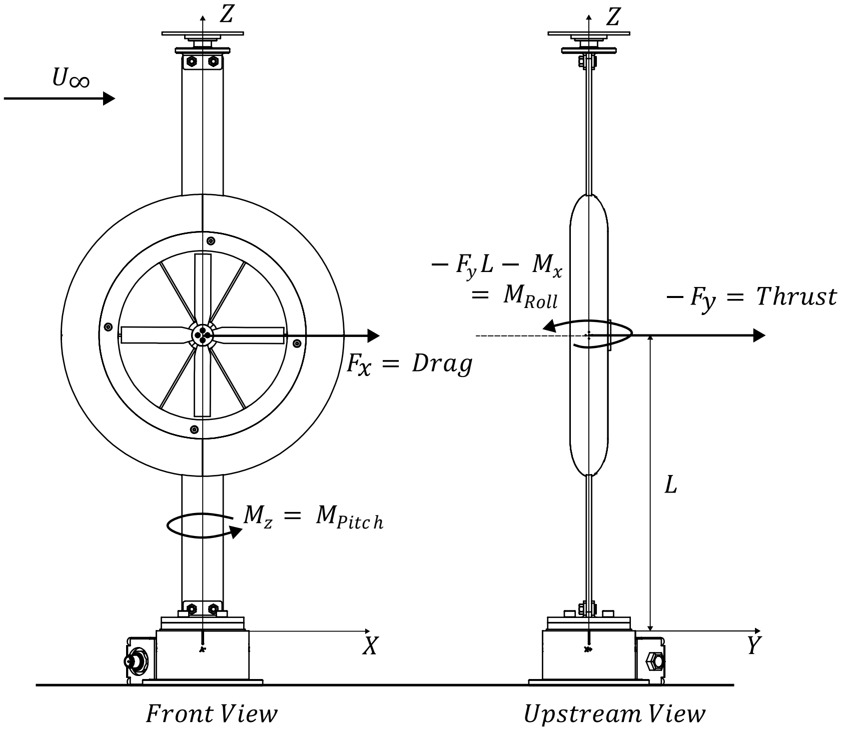

Fig. 3.7: The coordinate and configuration of Force/Torque measurements

In this study, an offset measurement was taken with the rotor stationary at a given edgewise velocity. By subtracting this offset from the measured results, the aerodynamic loads generated by the rotor's rotation can be obtained. Therefore, the measured loads indicate the change in aerodynamic performance due to the rotation of the blades. The sampling frequency was set to 2000 Hz, and the sampling period was set to 10s.

3.4 Experiment 2: Inner Surface Pressure Measurements

To measure pressure on the shroud's inner surface, pressure taps were designed on the surface at different depths and angular locations (Shown in Figure 3.8). The two columns of pressure taps have an angular increment of 5°. Each column has ten pressure taps, with a depth increment of 2.5 mm starting at $y = -2.5$ mm. By rotating the inner shroud and locking it at 36 different locations, a pressure map with 5° angular resolution and 2.5 mm depth resolution could be obtained.

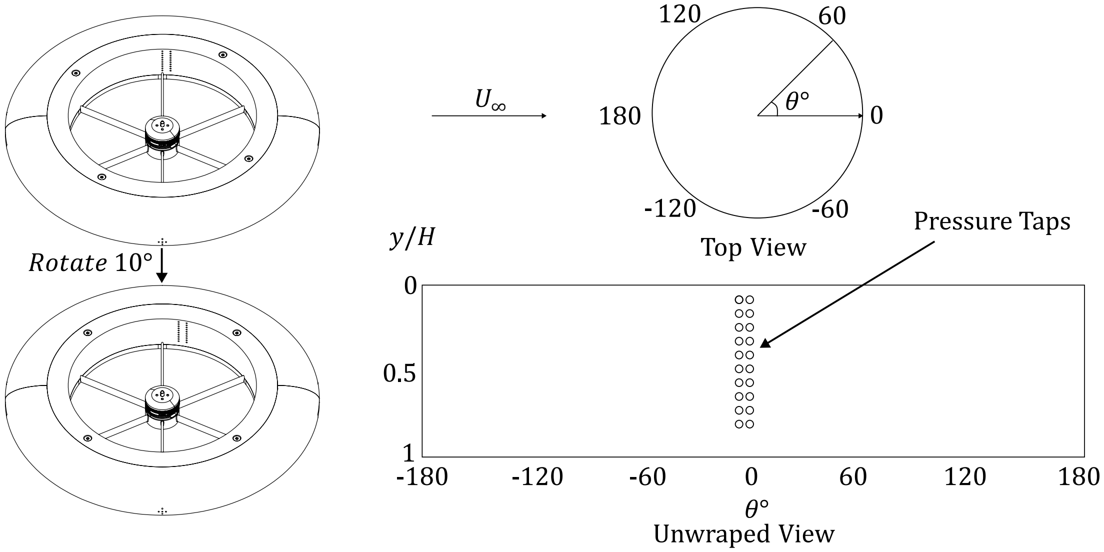

Fig. 3.8: Pressure measurement setup

The mean pressure on the shroud's inner surface was measured using a 64-channel MPS4264 miniature pressure scanner. The pressure scanner measures the difference between the pressure measured at channels 1-64 and the reference pressure. The pressure scanner has a measuring uncertainty of ±2 Pa. Stainless steel tubes with an inner diameter of 0.5 mm and outer diameter of 1mm are placed in the pressure taps, and these stainless-steel tubes are connected to channels 1-20 of the pressure scanner using 1-meter rubber tubes.

In this study, the air density ρ and viscosity μ are assumed to be constant in all measurements. The static pressure of the Pitot-static tube P_∞ is considered the reference pressure of the scanner. The pressure readings from channels 1-20 are the differential pressure at each location compared to the reference pressure $(P - P_\infty)$. Channel 64 measures the pressure difference between the Pitot-stagnation and the reference pressure $(P_t - P_\infty)$. Thus, the pressure coefficient could be calculated as:

$$c_p = \frac{P - P_\infty}{P_t - P_\infty}. \tag{3.3}$$

The edgewise velocity could be calculated as

$$U_\infty = \sqrt{\frac{2(P_t - P_\infty)}{\rho}}. \tag{3.4}$$

Due to the filtering effect of the rubber tubes, the sampling frequency was limited in the measurement. The scanner's sampling frequency was set to 500 Hz, and the sampling period was set to 60 seconds. This experiment setting gives 30000 pressure readings for each pressure tap. The pressure data was collected using the LabVIEW program *MPSLink.vi.*

3.5 Experiment 3: Inlet/Outlet Velocity Measurements

The freestream velocity in the wind tunnel was measured using the pressure scanner and the Pitot tube upstream of the setup. The high-frequency velocity measurement at the inlet and outlet surface of the shroud was measured using hot-wire anemometry.

3.5.1 Hot-wire Anemometry

Hot-wire anemometry is a high-frequency response measurement technique used to measure fluid flow velocity (Jørgensen (2001)). The hot-wire is connected to the constant temperature anemometer (CTA) through a holder and a BNC cable. Heat convection takes removed heat when it passes by the wire. The CTA has a feedback system to maintain a constant temperature on the thin wire exposed to the flow. The wire is assumed to be a circular cylinder, and the heat loss on the wire is

$$q = h_c dl(T - T_{ref}) = (a + bU^n)d_w l_w (T_w - T_{ref}), \tag{3.5}$$

where h_c is the heat transfer coefficient, T_{ref} is the environment temperature, d_w and l_w are the diameter and length of the wire. When connected to a CTA, the Joule heat generated by the wire resister (R_w) balances the heat loss. Therefore, the relation between the voltage across the wire (E_w) and the flow velocity is

$$E_w^2 = (a + bU^n)d_w l_w R_w (T_w - T_{ref}). \tag{3.6}$$

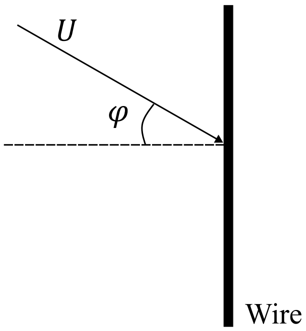

Fig. 3.9: Effective cooling velocity on the wire

This relationship could be simplified as the Simplified King's Law, described as

$$E_w^2 = (A + BU^n). \tag{3.7}$$

In all the derivations above, the flow velocity direction is assumed to be normal to the wire. The alignment effect of hot-wire measurement occurs when the flow direction is not perpendicular to the wire (shown in Figure 3.9). The normal velocity component and longitudinal component of the velocity affect the cooling of the wire. The effective cooling velocity U_{eff} under this circumstance is

$$U_{eff}^2 = U^2(\cos\psi^2 + k^2 \sin\psi^2), \tag{3.8}$$

where ψ is the yaw angle, and k is the yaw factor and $k^2 \in (0.02, 0.20)$. By reversing the process of finding U_{eff}, the yaw angle could be determined, which allows the two-dimensional and three-dimensional velocity measurement by adding more wires to the probe at different angles. The X-wire probe could accomplish two-dimensional measurements, and the Tri-wire probe could do three-dimensional measurements.

For this study, to measure velocity in both streamwise (U) and axial (V) directions, the Dantec 55P61 straight miniature X-wire probe was used. The X-wire probe has two platinum-plated tungsten wires with $5\mu m$ diameter in two parallel planes with tiny spaces in between. The wires are mounted at $\pm 45°$, which allows the probe to conduct two-dimensional velocity measurements. The probe was held by Dantec

55H25 long straight probe support and connected to two Dantec 90C10 CTA modules with two 4 m long Dantec A1863 BNC cables. The analog-to-digit converter (A/D converter) and data acquisition card was a National Instruments NI PCIe-6363 card and connected with the CTA using another two BNC cables. The A/D converter is a 16-bit card with ±10 V voltage input range.

The hot-wire operated at an overheat ratio $a = 0.8$ in all velocity measurements. The sample frequency was set to 20 kHz. At each measuring position, the sample time was set to 20 seconds. The calibration and measurement process was done using the Streamline Pro software.

3.5.2 X-wire Calibration and Velocity Conversion

The X-wire calibration consists of two parts: velocity calibration and direction calibration. The Dantec Automated Calibrator was used in the calibration process. The calibrator, connected to compressed air, could generate a jet with a velocity from 0.5 m/s to 60 m/s. In velocity calibration, the voltages E_1 and E_2 were measured with the two wires placed in a small jet of known velocities. Two fourth-order polynomials were used instead of the King's Law to fit the velocity-voltage curves.

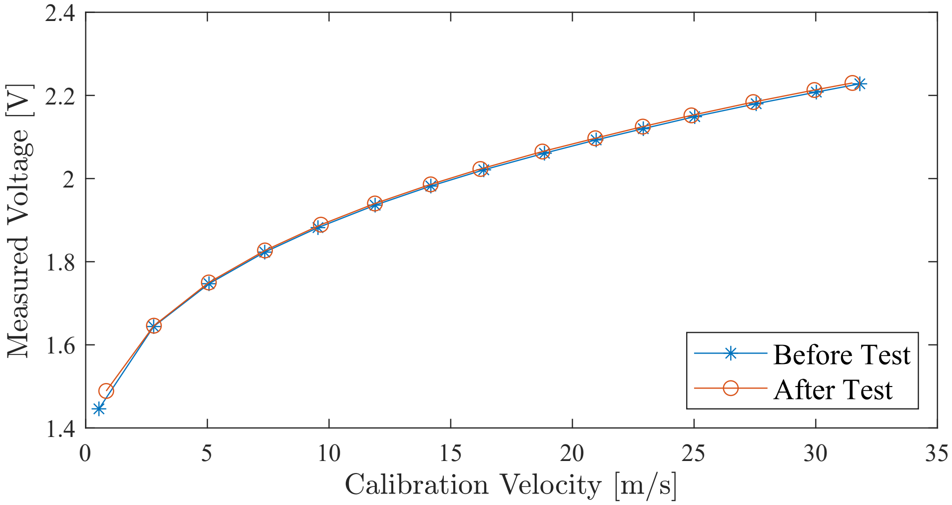

Fig. 3.10: The velocity calibration before and after a test (80 minutes in between)

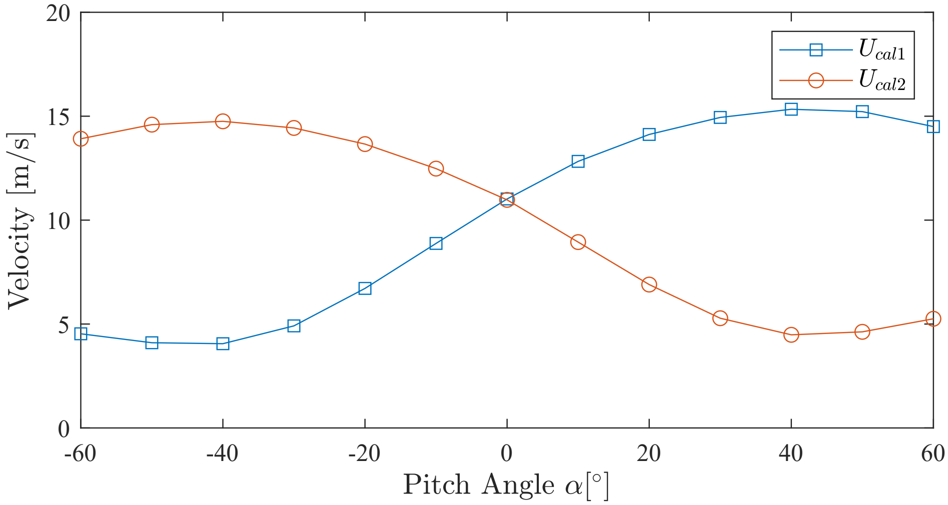

Fig. 3.11: The directional calibration gave squared yaw factor $k_1^2 = 0.024$ and $k_2^2 = 0.083$

The hot-wire measurement is highly sensitive to the temperature of the flow. The temperature of the flow could vary with time in the experiments. Without the thermal sensor that could perform the temperature correction in the measurement, multiple calibrations were necessary to mitigate the effect of temperature drift. Figure 3.10 compares calibration curves before and after an 80-minute experiment.

For the direction calibration, The Dantec calibration module has an attachment that can move the probe to different angles with respect to the oncoming flow. In this thesis, an angle range of -40° to 40° was used. The calibration process gives two yaw factors ${k_1}^2$ and ${k_2}^2$. Figure 3.11 shows the voltages versus yaw angle plot for a directional calibration process.

By using the 4^{th} order polynomial curve fit, the voltage E_1, E_2 could be converted to U_{cal1} and U_{cal2}. The velocity U_1 and U_2 in the wire-coordinate system can be obtained by Equation (3.9).

$$\begin{aligned} U_1 &= \frac{\sqrt{2}}{2}\sqrt{(1+k_2^2)U_{cal2}^2 - k_2^2 U_{cal1}^2} \\ U_2 &= \frac{\sqrt{2}}{2}\sqrt{(1+k_1^2){U_{cal1}}^2 - k_1^2 U_{cal2}^2} \end{aligned} \tag{3.9}$$

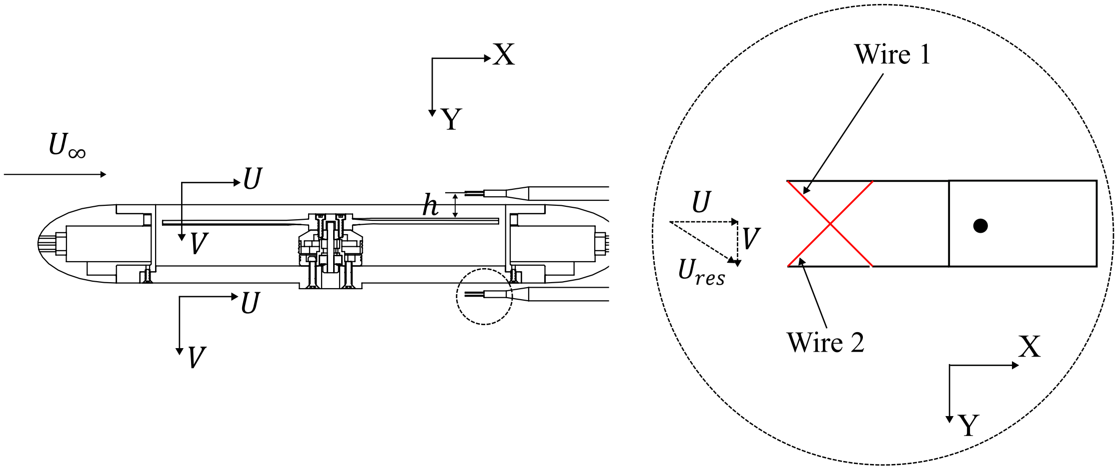

Fig. 3.12: The configuration of hot-wire coordinate. Positive V always goes from inlet to exit

The velocities U and V in the probe coordinate system can be calculated using Equation (3.10).

$$U = \frac{\sqrt{2}}{2}U_1 + \frac{\sqrt{2}}{2}U_2$$

$$V = \frac{\sqrt{2}}{2}U_1 - \frac{\sqrt{2}}{2}U_2 \tag{3.10}$$

Figure 3.12 shows the probe coordinate system and its relative location to the shrouded rotor. In the experiment, the closest distance from the wire and rotor is set to $h = 12$ mm to avoid damaging the wire while moving the traverse. In this coordinate, positive V indicates velocity entering the shroud at the inlet, whereas, at the outlet, it means flow exiting the shroud.

3.5.3 Linear Positioning System and Velocity Measurement Grid

Figure 3.13 shows the linear positioning system used in this measurement. Two Velmex XN12 traverses move the hot-wire in X and Z directions. The XN12 traverses were powered by Velmex PK266 Motor. The traverse system was controlled by the Velmex VMX controller. Two 1.5-inch-travel-distance Velmex manually operated Unislide A15 linear traverse were attached to a 3D printed plate and connected to the Z traverse cart. The UniSlide traverse gives mobility in the Y direction, which

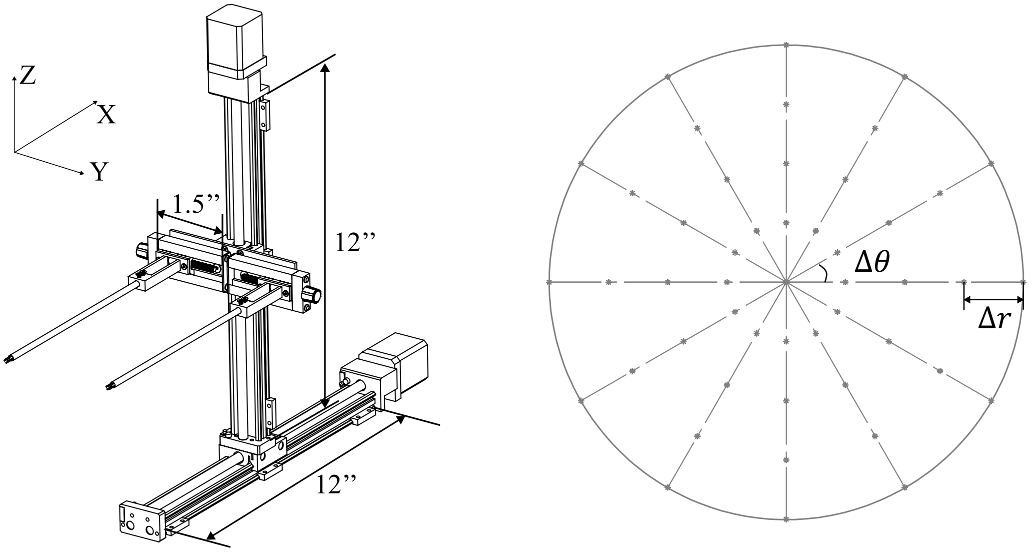

Fig. 3.13: The linear positioning system for velocity measurements and the measure grid. Left: The assembly of linear traverses, hot-wire holders, and hot-wire probes. Right: the polar grid used in the velocity measurements with $\Delta\theta = 30°$ angular increment and $\Delta r = 19.5$mm radial increment.

could change the distance between the probe to the inlet and outlet surface of the shroud.

A total of 49 measuring points, arranged in a polar grid shown in Figure 3.13, were employed to measure the velocity at the inlet and outlet plane of the shrouded rotor. The data recording starts 10 seconds after the traverse stops at each point. The grid generation and the control of the linear traverses were built into the LabVIEW program named *=Shrouded_Propeller_Test=.vi* (see Appendix B).

Chapter 4

Results and Discussion

The results of the three experiments are presented in this chapter. The ISAE-4 rotor was characterized, and the aerodynamic loads of hovering and edgewise flight conditions were compared. The shrouded rotor performance in edgewise flight was analyzed with respect to the velocity ratio μ. The mean pressure distribution on the shroud's inner surface for edgewise flight cases was measured to assess the pressure drag. The velocity distribution at the inlet and outlet planes was also measured, enabling the calculation of the resultant elemental thrust distribution of the rotor. The turbulence intensity and spectra at the shroud inlet plane were also analyzed.

4.1 Shrouded Rotor Aerodynamic Load

The aerodynamic loads of the shrouded rotor were tested under hovering and edgewise flight conditions. For the hovering condition, an offset was measured with a stationary rotor, whereas for the edgewise flight condition, the offsets were taken with the wind tunnel running and a stationary rotor. Therefore, the results shown in this section are the difference in thrust, drag, pitching moment, and rolling moment acting on the entire test rig caused by the rotation of the rotor. Ten different throttles were set for the motor in the tests, giving a rotating speed from 3500 RPM to 7500 RPM. Five edgewise velocities were set from 5 m/s to 13 m/s for the edgewise tests. Five repeated tests were performed at each measured condition, and the mean values were recorded. The uncertainty of the force measurement is less than ±0.02 N, and the

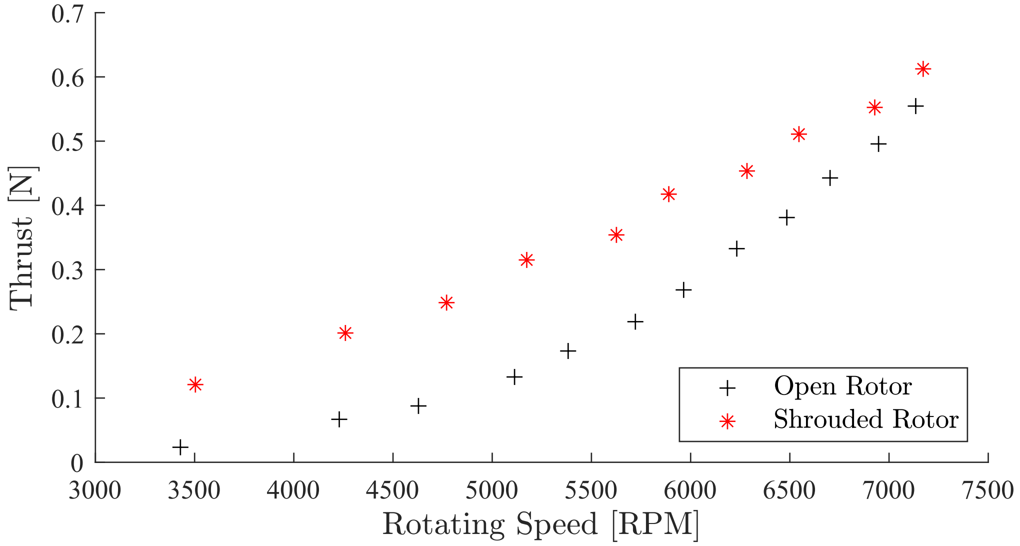

Fig. 4.1: Thrust force of shrouded and open rotor in hover

uncertainty for the moment measurements is less than $\pm 1.7 \times 10^{-3}$ Nm. The rotating speed variation between repeated runs is lower than ±40 RPM. The error bars are smaller than the size of the marker and, therefore, are not shown in the figures in this section.

4.1.1 Thrust

The hovering thrust from the shrouded and open rotors is measured and compared. As shown in Figure 4.1, at all rotating speeds, the thrust from the shrouded rotor is greater than that provided by the open rotor. This result is consistent with the finding of Pereira (2008) and proves that the presence of the shroud enhances the total hovering thrust.

Figure 4.2 shows the thrust force at different inflow conditions. The shrouded rotor consistently produces greater thrust during edgewise flight than hovering across all rotor rotation speeds. Moreover, it is shown that the thrust force generated at a certain rotation speed increases with the rise of edgewise velocity U_∞.

The thrust ratio TR and the thrust coefficient C_T were used as non-dimensional thrust and examined with respect to the velocity ratio μ. The thrust ratio is defined as

$$TR = \frac{T_{Edgewise}}{T_{Hover}}, \tag{4.1}$$

where $T_{Edgewise}$ and T_{Hover} are the thrust force at the same rotating speed. The thrust values are obtained by linear interpolation and extrapolation from measured data points for each edgewise velocity. It shows in Figure 4.3 that with this normalization, the thrust ratio at different U_∞ collapse onto a single curve with respect to μ and shows a descending trend of thrust ratio with increasing μ. This indicates that the edgewise flow generates less incremental thrust with the increase of μ.

The thrust coefficient C_T is defined as

$$C_T = \frac{T}{\rho n^2 {D_r}^4}, \tag{4.2}$$

where n is the rotating speed of the rotor in rev/s and D_r is the diameter of the rotor. From the C_T versus μ plot shown in Figure 4.4, it is clear that the data points collapse to a single curve. Data points with similar velocity ratio μ are close to each other on the plot even with different U_∞ and rotating speed. This also clearly demonstrates that the change in performance is independent of the Reynolds number, whether it

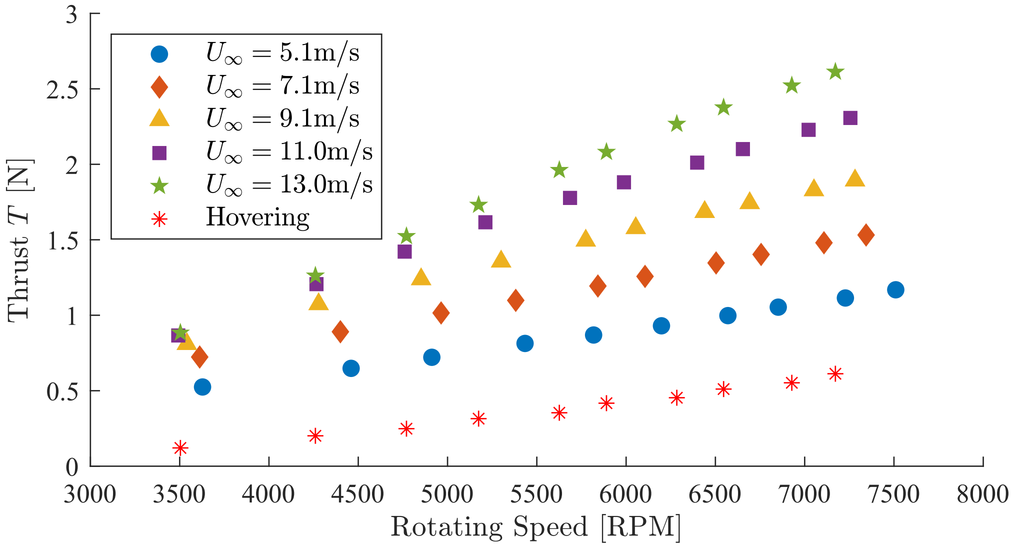

Fig. 4.2: Thrust force of the shrouded rotor in hovering and edgewise flight

be defined using the chord or diameter and the edgewise, rotational, or resultant velocity. This indicates that μ is an essential parameter for the thrust performance of the shrouded rotor in edgewise flight. Within this testing range, a 6^{th} polynomial of the form

$$\begin{split}C_T(\mu) = -3.8\times10^{-6}\mu^6 + 1.9\times10^{-4}\mu^5 - 3.7\times10^{-3}\mu^4 \\ + 3.7\times10^{-2}\mu^3 - 1.9\times10^{-1}\mu^2 + 4.4\times10^{-1}\mu + 2.9\times10^{-6}\end{split} \quad (4.3)$$

was found to fit the data well. The thrust coefficient exhibits a decreasing trend as the velocity ratio increases within the defined μ interval. The thrust of the hovering cases within this rotating speed range is shown as the red band on the plot. As μ approaches infinity (representing the hover case), the C_T curve converges towards this band.

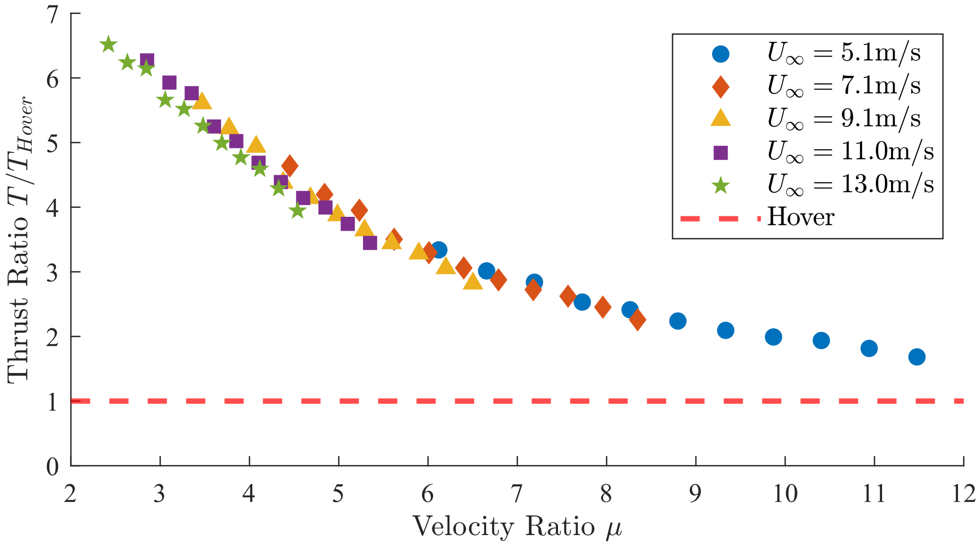

Fig. 4.3: Thrust ratio TR at various velocity ratio μ

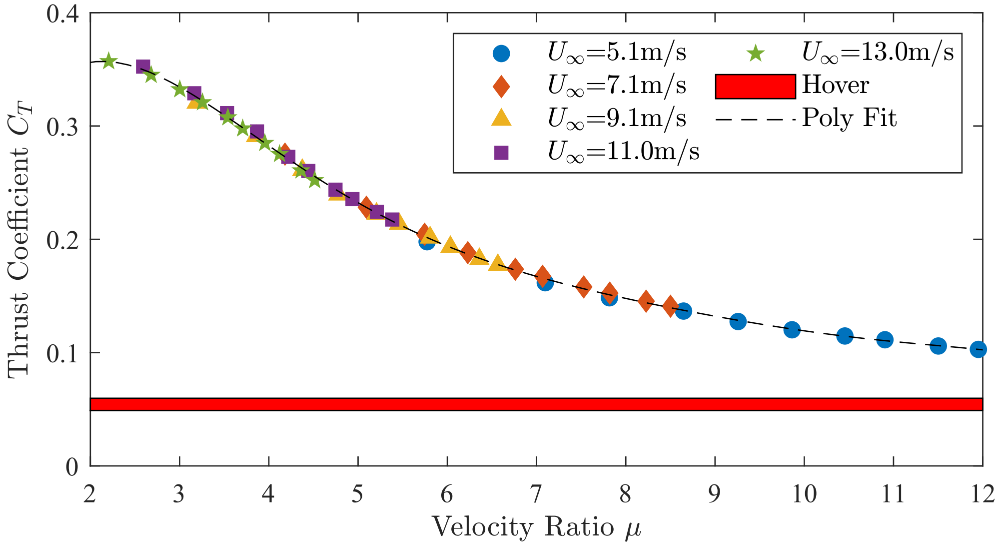

Fig. 4.4: Thrust coefficient C_T at various velocity ratio μ. The red band means the thrust coefficient of the hovering rotor, data points with different U_∞, and rotating speeds collapse to the same curve.

4.1.2 Drag

For the drag force measurement, the load cell measured the global drag force acting on the shrouded rotor stand, which consists of six components

$$D_{Total} = D_{Support} + D_{InnerShroud} + D_{OuterShroud} + D_{Rotor} + D_{Stator} + D_{Hub}. \tag{4.4}$$

All of these components could be affected by the rotation of the rotor and the edgewise inflow. An offset was taken with a stationary rotor at each edgewise velocity. By subtracting this offset, the resultant drag force represents the incremental drag created solely by the rotation of the rotor. This incremental drag $\hat{D}$ is defined as

$$\hat{D} = D_{Total}\big|_{U_\infty \neq 0}^{\Omega \neq 0} - D_{Total}\big|_{U_\infty \neq 0}^{\Omega = 0}. \tag{4.5}$$

Figure 4.5 shows the incremental drag force acting on the shrouded rotor. The incremental drag force stays constant at zero for the hovering cases, indicating that no extra drag was generated when the rotor started rotating. In edgewise flight

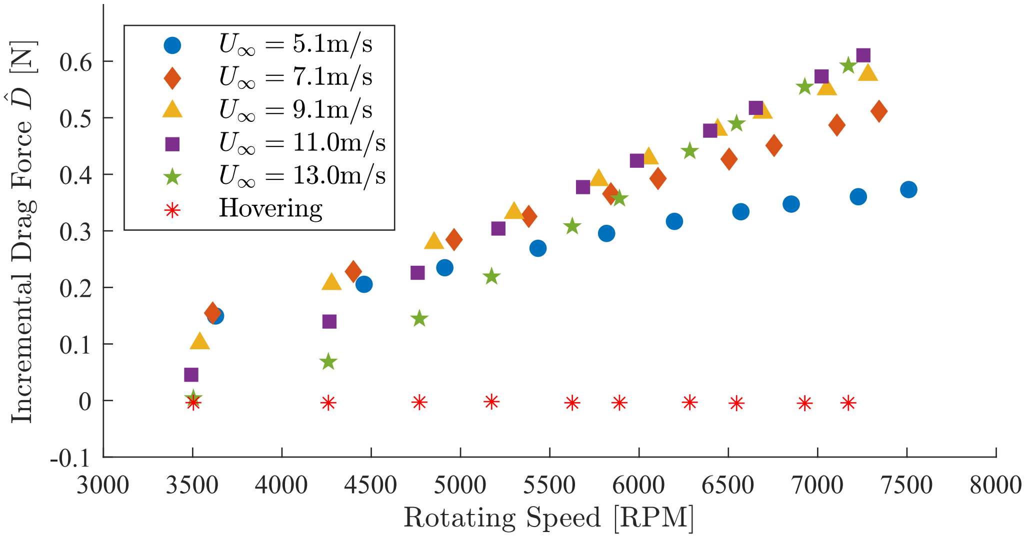

Fig. 4.5: Incremental drag force caused by rotation of the rotor at different edgewise velocity and rotating speed

conditions, the rotation of the rotor introduces extra drag force on the test stand. the drag force increases with the rotating speed regardless of U_∞. Higher U_∞ gives a lower drag force at low rotating speed, while the trend is the opposite for high rotating speed cases.

Similar to thrust, the incremental drag force is also normalized to incremental drag coefficient $C_{\hat{D}}$ analyzed with respect to various velocity ratios. The drag coefficient is defined as

$$C_{\hat{D}} = \frac{\hat{D}}{\rho n^2 {D_r}^4}. \tag{4.6}$$

Figure 4.6 shows $C_{\hat{D}}$ versus μ plot. It is noticeable that all $C_{\hat{D}}$ data points collapse onto the same curve, proving that the velocity ratio μ is a crucial parameter for the drag performance of the shrouded rotor in edgewise flight. Unlike the thrust ratio, $C_{\hat{D}}$ increases with μ when $\mu < 4.40$ and decreases when μ further increases and eventually converges to the hover case with μ approaches infinity. Maximum drag coefficient is observed at $\mu = 4.40$ with $C_{\hat{D},max} = 0.059$. Within this testing range, the incremental

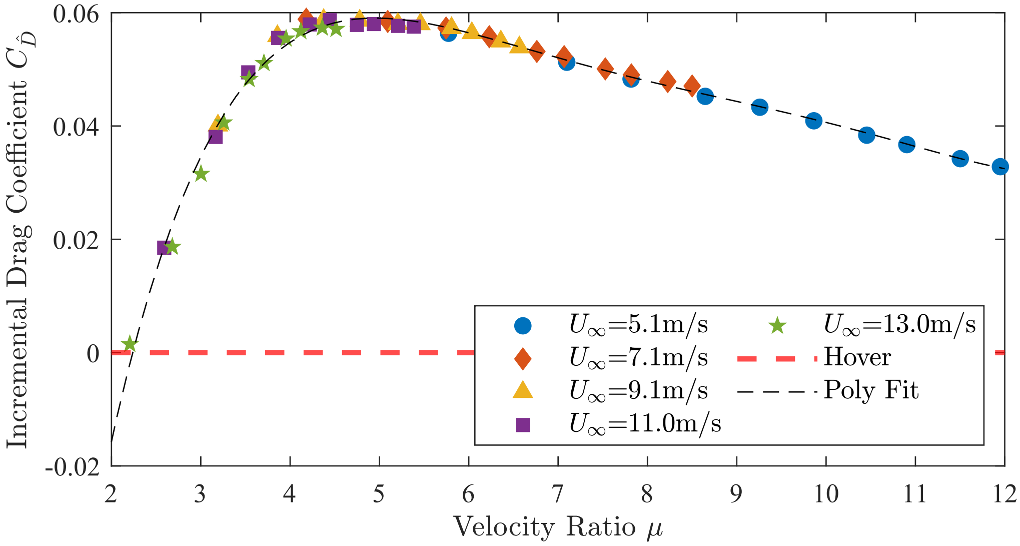

Fig. 4.6: Incremental drag coefficient $C_{\hat{D}}$ at various velocity ratio μ. The red dashed line shows the drag coefficient of the hovering case, and data points with different U_∞ and rotating speeds collapse to the same curve.

drag coefficient could be fitted by a 5^{th} order polynomial

$$C_{\hat{D}}(\mu) = 8.8 \times 10^{-6}\mu^5 - 3.9 \times 10^{-4}\mu^4 + 6.7 \times 10^{-3}\mu^3 - 5.6 \times 10^{-2}\mu^2 + 2.3 \times 10^{-1}\mu - 2.9 \times 10^{-1}. \quad (4.7)$$

4.1.3 Pitching & Rolling Moment

The pitching moment is shown in Figure 4.7, and is non-zero for all edgewise flight cases and increases with rotating speed and edgewise velocity. Unlike the hovering condition, edgewise flow creates a nose-up pitching moment M_{Pitch}, which tends to lift the front part of the shrouded rotor. This indicates that the thrust is not uniformly distributed and suggests that the elemental thrust generated by the front half of the rotor is higher than the rear half.

Additionally, a rolling moment M_{Roll} occurs in edgewise flight conditions due to the advancing and retreating effect of the rotor. As shown in Figure 4.8, M_{Roll} increases with rotating speed for all edgewise velocities.

The pitching and rolling moment could be normalized to the pitching coefficient C_{Pitch} and rolling coefficient C_{Roll}, which are defined as

$$C_{Pitch} = \frac{M_{Pitch}}{\rho n^2 {D_r}^5}, \tag{4.8}$$

$$C_{Roll} = \frac{M_{Roll}}{\rho n^2 {D_r}^5}. \tag{4.9}$$

Figure 4.9 shows C_{Pitch} and C_{Roll} at various μ. Like the thrust and drag coefficients, the pitching and rolling coefficients collapse. When the velocity ratio μ increases, these two non-dimensional moments have different trends. The pitching coefficient first increases and then decreases, with a peak point at $\mu = 4.18$ with maximum $C_{Pitch} = 0.052$. The rolling coefficient increases when μ increases. The pitching and rolling coefficient in this testing range could be fitted by 6^{th} order polynomial:

$$\begin{aligned} C_{Pitch}(\mu) &= 6.2 \times 10^{-7}\mu^6 - 2.2 \times 10^{-5}\mu^5 + 2.9 \times 10^{-4}\mu^4 \\ &\quad - 1.4 \times 10^{-3}\mu^3 - 1.3 \times 10^{-3}\mu^2 + 2.6 \times 10^{-2}\mu + 9.2 \times 10^{-6}, \end{aligned} \tag{4.10}$$

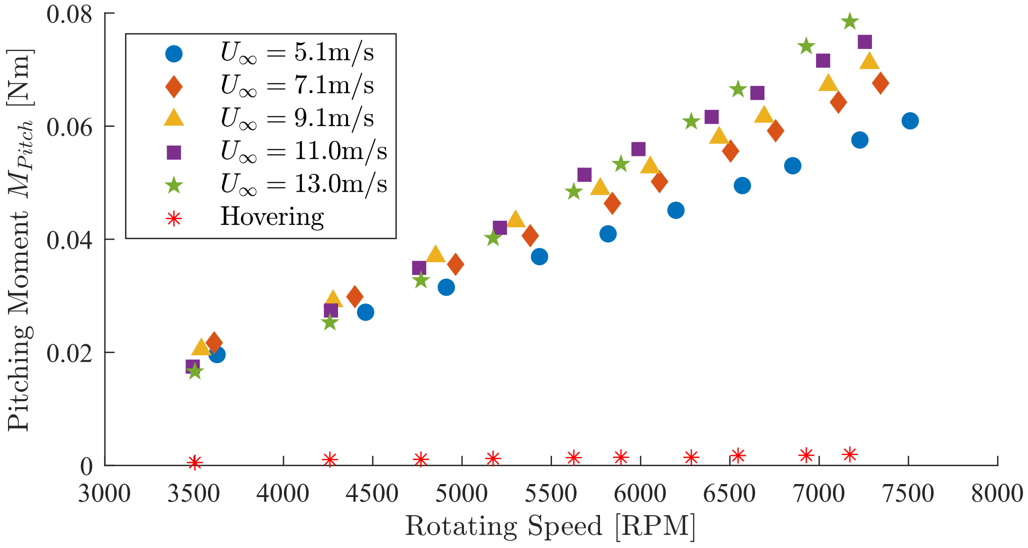

Fig. 4.7: Pitching moment of the shrouded rotor in hovering and edgewise flight

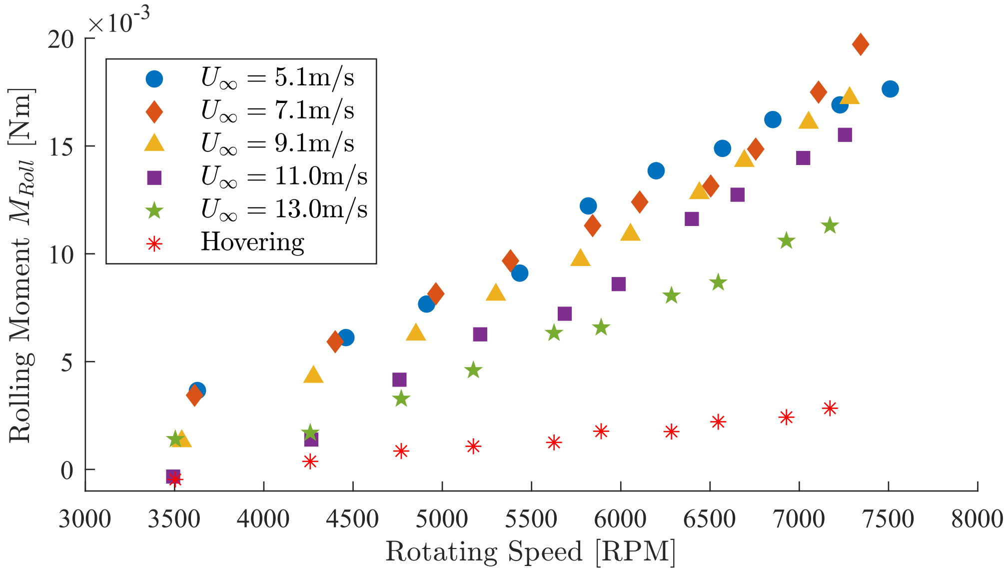

Fig. 4.8: Rolling moment of the shrouded rotor in hovering and edgewise flight

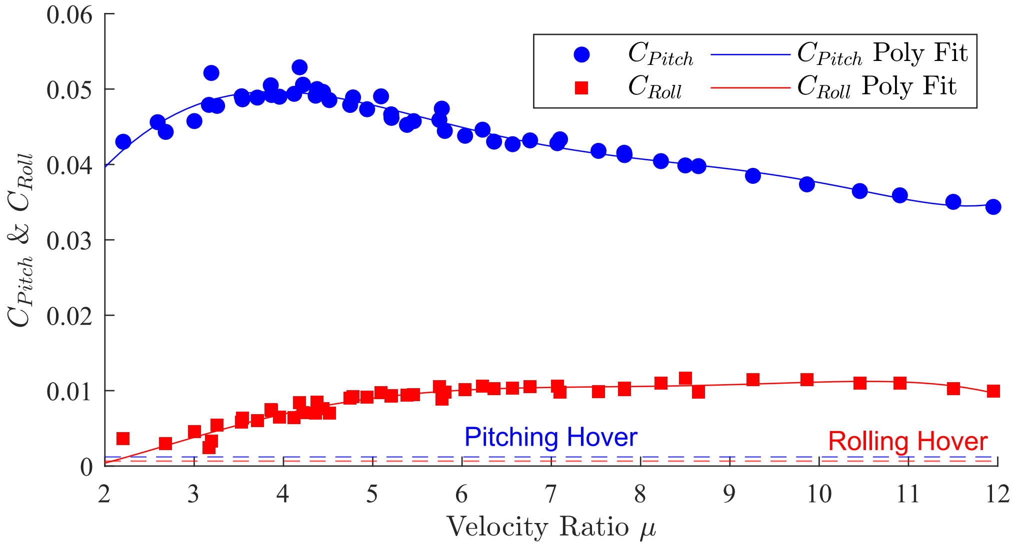

Fig. 4.9: Pitching and rolling moment coefficient at different velocity ratio μ

$$C_{Roll}(\mu) = 2.4 \times 10^{-8}\mu^6 - 2.8 \times 10^{-6}\mu^5 + 7.7 \times 10^{-5}\mu^4 - 8.6 \times 10^{-4}\mu^3 + 4.1 \times 10^{-3}\mu^2 - 5.1 \times 10^{-2}\mu + 6.9 \times 10^{-5}. \quad (4.11)$$

At all velocity ratios, C_{Pitch} is larger than C_{Roll}, which indicates that the nose-up pitching moment is more significant than the rolling moment on the shrouded rotor in edgewise flight.

The fact that there is a non-zero pitching and rolling moment would therefore suggest that the location where the resultant thrust is acting is in the lower left quadrant of the inflow plane, or $-180° \leq \theta \leq -90°$ (see Figure 3.8). This will be verified later in the thesis via the velocity measurements across the inlet plane.

4.2 Shroud's Inner Surface Pressure Measurement

4.2.1 Mean Pressure

The mean pressure distribution on the shroud's inner surface was measured at three different motor throttles, giving a rotating speed of approximately 4200 RPM, 5700 RPM, and 6700 RPM. Five edgewise velocities (U_∞) were set in the experiment, ranging from 5 m/s to 15 m/s. The cases with stationary rotors were also tested as a baseline case in the pressure drag calculation, where non-zero U_∞ and zero V_{tip} give a velocity ratio of $\mu = 0$.

A spline 2D interpolation was applied to the mean pressure data to obtain a pressure map on a fine grid with 361 angular locations and 51 depth locations. Figures 4.10 to 4.12 show the unwrapped pressure contour on the shroud's inner surface at different velocity ratios. The airfoil profiles in the plots show the stator blades' location. The black line at $y/H = -0.2$ shows the height of the rotor disk plane. According to the definition of c_p shown in Equation (3.3), a negative c_p indicates that the pressure is lower than the reference pressure (Pitot-static pressure).

For the cases with stationary rotor ($\mu = 0$), the pressure on the inner surface is lower than the Pitot-static pressure at all angular and depth locations. The pressure

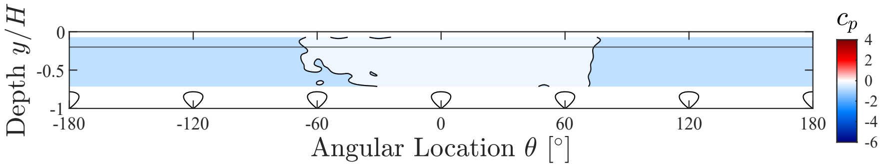

Fig. 4.10: Pressure distribution on the unwrapped inner shroud surface at $\mu = 0$

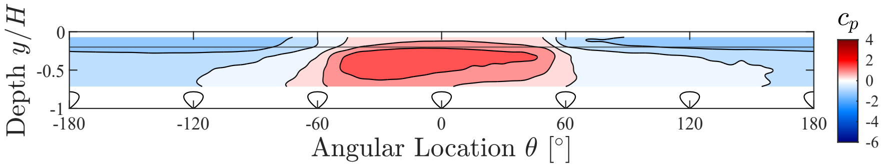

(a) $U_\infty = 9.16$m/s, 5685 RPM, $\mu = 4.77$

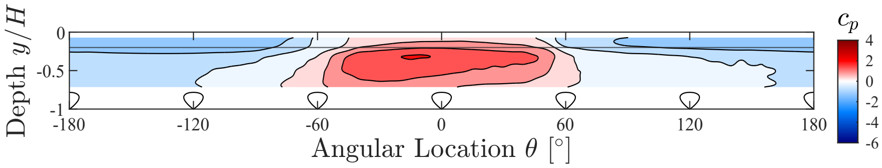

(b) $U_\infty = 11.07$m/s, 6732 RPM, $\mu = 4.87$

Fig. 4.11: Pressure distribution on the unwrapped inner shroud surface at similar velocity ratio μ but different rotating speed and U_∞

between $\theta = 60°$ and $\theta = -60°$ is higher than the rest angular locations. Figure 4.11 shows the unwrapped mean pressure contour of two test cases with similar μ but with different rotating speeds and edgewise velocities. A similar pressure distribution emphasizes that the velocity ratio μ is a decisive parameter to characterize the flow.

Figure 4.12 shows the results for three of the 15 edgewise flight cases. For all edgewise flight cases, a higher-pressure region is formed near the rear end of the shroud (near $\theta = 0°$). The high-pressure region indicates that the flow is redirected and attached to the shroud's inner surface near the rear end of the shroud. In Figure 4.12b and 4.12c, the pressure at the depth of the rotor plane ($y/H = -0.2$) is lower than the other depth locations. Meanwhile, there is no apparent difference between the pressure at that height and the surrounding heights for stationary rotor cases. This difference indicates that this low-pressure region is related to the rotation of the rotor.

Figure 4.13 helps visualize the change of mean pressure coefficient with respect to depth locations at the front end ($\theta = 180°$). The pressure for the stationary rotor case does not vary with height, which indicates that flow separates within the measuring depth interval. For all $\mu \neq 0$ cases, the lowest pressure occurs at approximately the same depth location slightly above the rotor plane. A lower-pressure region is located at a similar height in the high-pressure region, as shown in Figure 4.12c. When setting the sampling frequency to 800 Hz (the upper limit of the pressure scanner), a spike

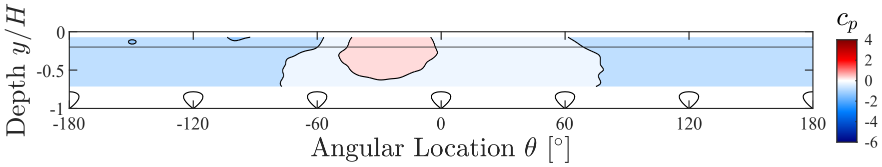

(a) $\mu = 2.15$

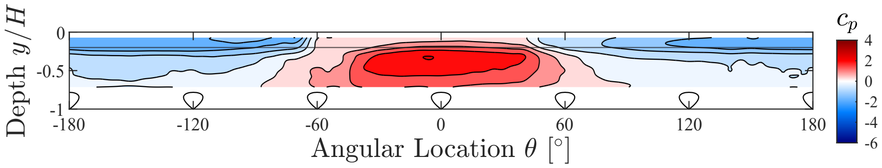

(b) $\mu = 6.31$

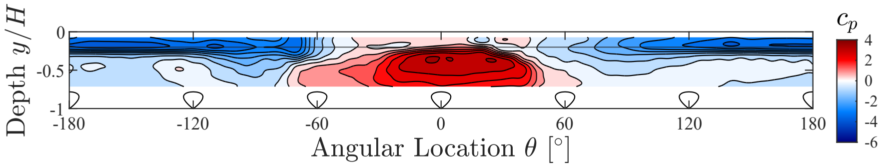

(c) $\mu = 10.27$

Fig. 4.12: Pressure distribution on the unwrapped inner shroud surface at different velocity ratio μ

in the blade passing frequency could be observed on the pressure spectrum. This indicates that this low-pressure zone could result from the rotor's tip vortices (tip leakage) and needs higher frequency pressure measurements to validate.

With the change of μ, the depth location and magnitude of the high-pressure region vary. Figure 4.14 shows a clear trend that with the increase of μ, the maximum c_p on the surface increases, and the minimum c_p decreases to a further negative value. Additionally, the high-pressure region moves towards the shroud outlet ($y/H = 1$). Figure 4.15 shows that the height of the peak pressure point (y_{peak}/H) moves towards the outlet of the shroud with the increase of μ. Furthermore, the maximum c_p, minimum c_p, and y_{peak}/H at similar μ are close to each other.

4.2.2 Pressure Drag

Similar to the grazing flow over a circular cylindrical cavity (Hiwada *et al.*, 1983; McCarthy & Ekmekci, 2022), the pressure on the shroud's inner surface generates

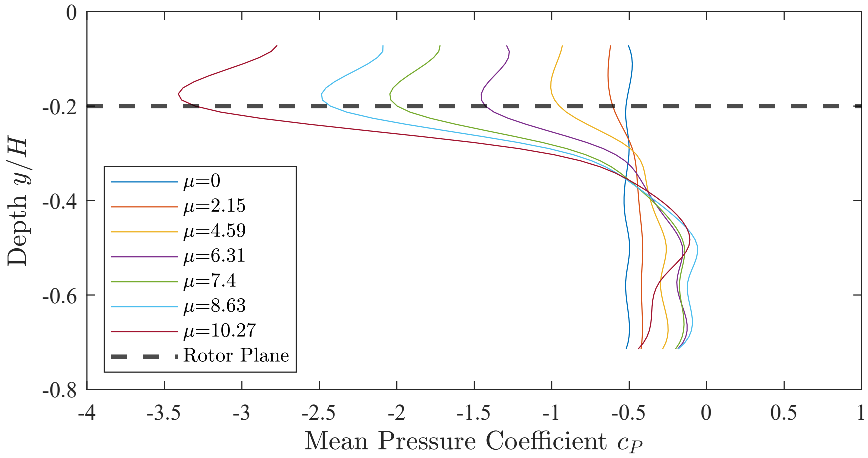

Fig. 4.13: The change of mean pressure coefficient with depth at $\theta = 180°$

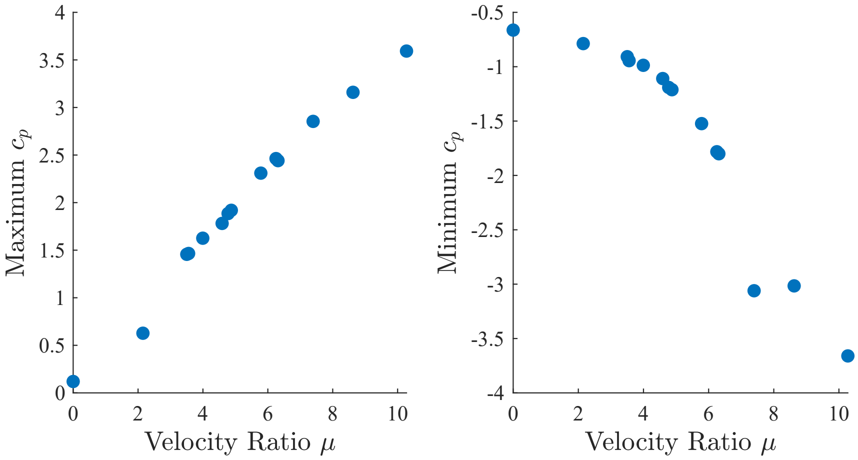

Fig. 4.14: Maximum and minimum c_p at different velocity ratio μ

drag force. The drag force acts in the positive X direction; therefore, only the X component of the pressure force contributes to the pressure drag. The pressure drag coefficient could be resolved by integrating the mean pressure coefficient over the inner surface area

$$C^p_{\hat{D},0} = \frac{1}{A}\int c_p \cos\theta \, dA, \tag{4.12}$$

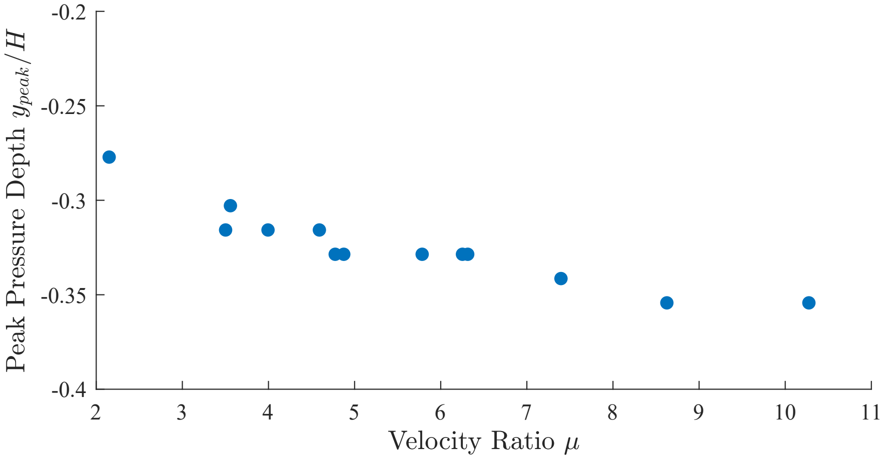

Fig. 4.15: Height of peak pressure coefficient y_{peak}/H at different velocity ratio μ

where $A = \pi D_i H$ is the surface area of the inner shroud surface and θ is the angular location. The differential area dA is defined as

$$dA = \frac{D_i}{2} d\theta dy. \tag{4.13}$$

The discrete form of Equation (4.12) is

$$C^p_{\hat{D},0} = \frac{1}{2\pi H} \sum_{i=1}^{72} \sum_{j=1}^{10} c_p^{i,j} \cos\theta_i (\theta_{i+1} - \theta_i)(y_{j+1} - y_j). \tag{4.14}$$

In this definition, the pressure drag force is normalized using the edgewise velocity U_∞ and the shroud inner surface area. The normalization is different from the normalization defined in Equation (4.6), which utilized the tip velocity of the rotor V_{tip} and the disk area of the rotor. To compare the two sets of results, a conversion of normalization is necessary. The incremental pressure drag coefficient $C^p_{\hat{D}}$ is defined as

$$C^p_{\hat{D}} = C^p_{\hat{D},0} \frac{U^2_\infty}{V^2_{tip}} \frac{\pi^2 H D_i}{D^2_r} = \frac{C^p_{\hat{D},0}}{\mu^2} \frac{\pi^2 H D_i}{D^2_r}. \tag{4.15}$$

The pressure distribution for cases with nonzero edgewise velocity and a stationary rotor was taken as an offset for the pressure drag calculation. Figure 4.16 compares the two drag coefficients. The plot shows that both drag coefficients have the trend

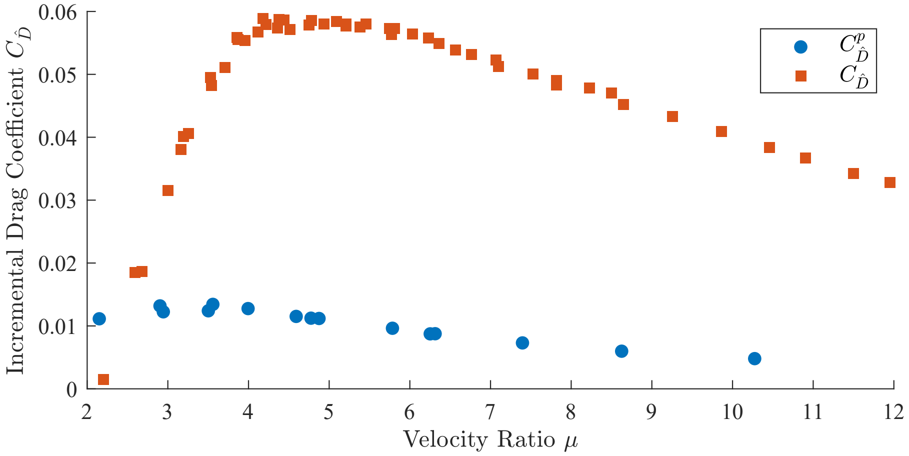

Fig. 4.16: Drag coefficient from pressure and F/T measurement at different velocity ratio μ

of first increasing and then decreasing with the increasing μ. It is also shown that except in the lower μ region ($\mu <= 2.5$), $C_{\hat{D}}$ is consistently larger than $C^p_{\hat{D}}$. The difference between the two drag coefficients indicates that the pressure drag on the inner surface of the shroud is just one of the components of the drag acting on the entire shrouded rotor. When $\mu < 2.5$, the incremental pressure drag on the shroud's inner surface dominates the total incremental drag, while with μ further increases, other components become dominant.

By splitting the shroud's inner surface as the front half and rear half with the plane go through $\theta = -90°$ and $\theta = 90°$, the pressure drag caused by the front and rear half of the shroud inner surface could be analyzed. As shown in Figure 4.17, $C^p_{D,Front}$ follows the trend of $C^p_{D,WholeShroud}$ and dominants the total pressure drag, while $C^p_{D,Rear}$ increases with μ, and starts to dominant when $\mu \geq 11$. This indicates that the flow separation at the front half of the shroud dominates the drag formation at lower μ; meanwhile, at high μ, the stagnation at the rear of the shroud's inner surface contributes more to drag formation.

4.2.3 Pressure at Leading Edge of the Shroud

During the edgewise flight test, pressure from the five pressure taps at the leading edge of the outer shroud is recorded. When the rotor rotates, the pressure reading

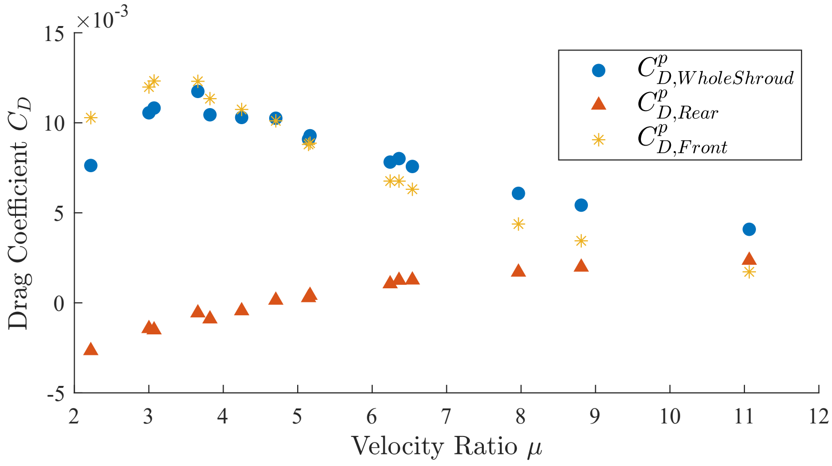

Fig. 4.17: Pressure drag coefficient on the front, rear half, and the whole inner shroud

at location 2 is always lower than location 4 (see Figure 4.18a for nomenclature), indicating that the stagnation point is closer to the exit plane. The stagnation point could be obtained by applying quadratic polynomial fitting for the pressure at 2, 5, and 4. As is shown in Figure 4.18, the angle of the stagnation point α varies with μ; as μ increases, the stagnation point is closer to the exit plane.

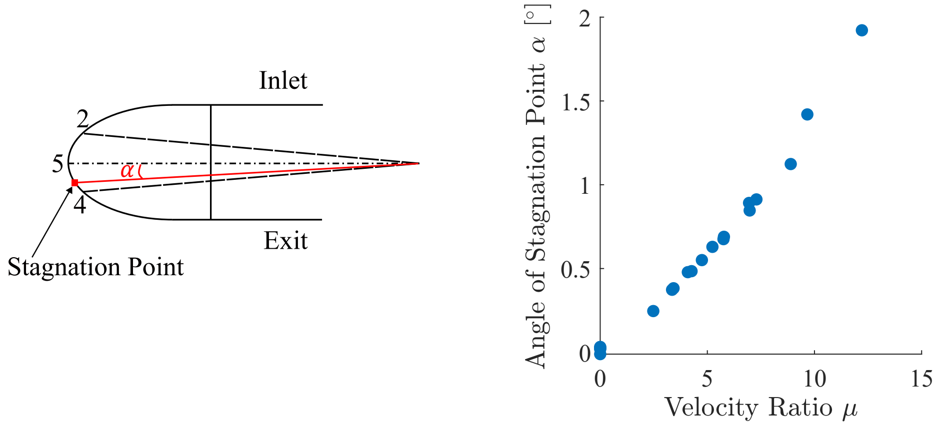

(a) Schematics

(b) α vs μ

Fig. 4.18: Stagnation points movement

The movement of the stagnation point gives rise to an angle of attack on the semi-elliptical leading edge and generates lift. This lift force affects the thrust and pitching moment on the shrouded rotor. An extra load cell could be implemented between the stator hub and motor to measure the loads on the rotor, which is left as a potential future investigation.

4.3 Velocity Measurements at Shroud Inlet and Exit

The axial (V) and streamwise (U) velocities at the shroud's inlet and outlet were measured at different velocity ratios. The experiment set the edgewise velocities as U_∞ = 6.7 m/s, 8.8 m/s, 10.2 m/s, and 14.0 m/s. Three different motor throttles were set in the experiment, giving a rotating speed of 4300 RPM, 5900 RPM, and 7300 RPM. The cases with stationary rotors were also tested to evaluate the shroud's effect on the flow. The U_∞ and rotating speed settings gave a velocity ratio range of $2.45 \leq \mu \leq 8.87$, which covers most of the testing range of the aerodynamic load measurements. Therefore, the impact of μ on the estimated aerodynamic loads, especially the trends of thrust and pitching moment, could be compared with the force/torque measurement results.

The output of the hot-wire anemometer provided a velocity time series, which can be used for turbulence analysis. The sampling time was set to $t_s = 20$ s and sampling frequency $f_s = 20$ kHz, which gave a time series of t_i with $i = 1, 2, ...20000$. The velocity outputs at time step t_i can be decomposed into mean and fluctuation components:

$$\begin{aligned} U(t_i) &= \overline{U} + U'(t_i), \\ V(t_i) &= \overline{V} + V'(t_i). \end{aligned} \tag{4.16}$$

The mean velocity distribution ($\overline{U}$ and $\overline{V}$) illustrates how the flow enters and exits the shroud, providing insights into the elemental thrust distribution and explaining the formation of the nose-up pitching moment.

The turbulent intensity (I) is used to characterize the level of turbulent fluctuation in the flow.

$$I_U = \frac{U_{rms}}{U_\infty}; \qquad U_{rms} = \sqrt{\frac{1}{N}\sum_{i=1}^{N} U'(t_i)^2}$$

$$I_V = \frac{V_{rms}}{U_\infty}; \qquad V_{rms} = \sqrt{\frac{1}{N}\sum_{i=1}^{N} V'(t_i)^2} \tag{4.17}$$

The turbulent intensity distribution at different velocity ratios was calculated to quantify the fluctuation of the flow.

4.3.1 Inlet Mean Velocity Distribution

The mean axial and streamwise velocity distribution of the case with a stationary rotor ($\mu = 0$) is shown in Figure 4.19. Both velocity components are symmetric about the centerline ($0° - 180°$ line). The axial component shows that the flow enters the shroud even without the rotation of the rotor, with the maximum $\overline{V}$ at $r/R = 0.6$ and $\theta = \pm 90°$. The distribution is highly independent of edgewise velocity. The streamwise component distribution shows that $\overline{U} > U_\infty$ in the front half of the rotor and $\overline{U} < U_\infty$ in the rear half with $\theta \in [-60°, 60°]$. Minimum $\overline{U}$ could be obtained at $r/R = 0.7$ and $\theta = 0°$.

Figure 4.20 shows the mean axial velocity $\overline{V}$ distribution at the inlet plane at three different velocity ratios. Compared to the case with the stationary rotor, the area of $\overline{V} > 0$ is enlarged due to the rotation of the rotor, indicating that more flow was redirected into the shroud. Unlike in hovering conditions, the axial velocity distribution is asymmetric about the rotor axis in edgewise flight cases. The axial velocity is higher in the front half and the advancing side of the rotor compared to other regions. This distribution varies with the velocity ratio. When μ is low, the velocity near the front end is negative, indicating that the flow is not entering the shroud in that region. Similar to the $\mu = 0$ case, this may be due to shear layer separation at the front of the shroud. As μ increases, the positive velocity region expands, accompanied by an increase in the maximum axial velocity. Moreover, as μ rises, the high-velocity region shifts towards the front end of the inlet ($\theta|_{\overline{V}_{max}}$ approaches $-180°$ as shown in Table 4.1).

Table 4.1: Summary of the effect of μ on the angular location of the maximum points of $\overline{V}$, β, dT and the center of thrust force at the shroud inlet

μ	$\theta\vert_{\overline{V}_{max}}[^\circ]$	$\theta\vert_{\beta_{max}}[^\circ]$	$\theta\vert_{dT_{max}}[^\circ]$	$\theta\vert_{thrust\_center}[^\circ]$
2.45	-76	-74	-70	-54
5.79	-143	-143	-97	-142
8.87	-173	-125	-175	-157

Figure 4.21 demonstrates the distribution of mean streamwise velocity on the inlet plane of the shroud at three different μ. The mean streamwise velocity is normalized as $\frac{\overline{U}-U_\infty}{U_\infty}$ to show whether the flow is accelerated or decelerated relative to the edgewise flow. It is shown that for all edgewise cases, the mean streamwise velocity is symmetric about the centerline ($0^\circ - 180^\circ$ line). $\overline{U}$ is relatively higher near the front end ($\theta = 180^\circ$). For lower μ cases, $\overline{U}$ is lower than U_∞ at $\theta = \pm 60^\circ$. As the velocity ratio μ increases, the velocity in the front half increases, and the two lower velocity regions disappear.

When examining cases with different rotational speeds and edgewise velocities, the axial and streamwise mean velocity distributions are similar at similar velocity ratios. These results indicate that μ is a decisive factor for the velocity field at the inlet of the shrouded rotor in edgewise flight.

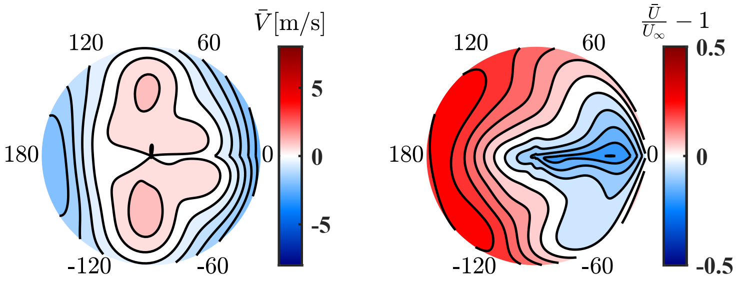

(a) Axial (b) Streamwise

Fig. 4.19: Mean axial and streamwise velocity distribution at shroud inlet plane with $\mu = 0$. (a)Red area means velocity into the shroud, and blue means velocity out. (b)Red area means velocity higher than U_∞, blue means lower. U_∞ from left to right.

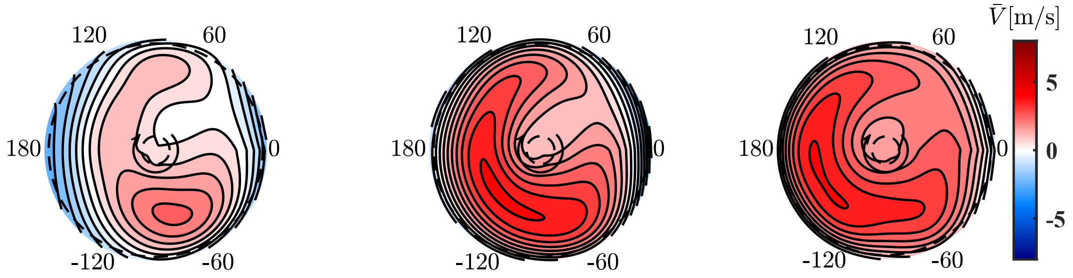

(a) $\mu = 2.45$ (b) $\mu = 5.79$ (c) $\mu = 8.87$

Fig. 4.20: Mean axial velocity distribution at shroud inlet plane with different μ. The arrows show the clockwise rotation of the rotor, and the two dashed circles indicate the hub and tip of the rotor.

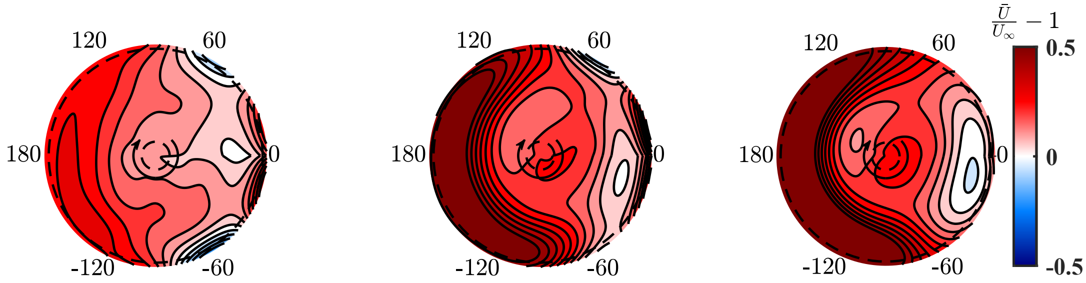

(a) $\mu = 2.45$ (b) $\mu = 5.79$ (c) $\mu = 8.87$

Fig. 4.21: Mean streamwise velocity distribution at shroud inlet plane with different μ.

Table 4.2: Summary of the effect of μ on overall $\overline{V}$, β, K/U_∞^2 (averaged over the testing grid) at the shroud inlet

μ	$\tilde{V}$ [m/s]	$\tilde{\beta}$[°]	$\tilde{K}/U_\infty^2$
2.45	0.71	2.54	0.356
5.79	1.98	8.65	0.079
8.87	2.44	15.59	0.044

With the axial and streamwise velocity measurements, the velocity angle β with respect to the edgewise direction could be computed as

$$\beta = \tan^{-1}\left(\frac{\overline{V}}{\overline{U}}\right). \tag{4.18}$$

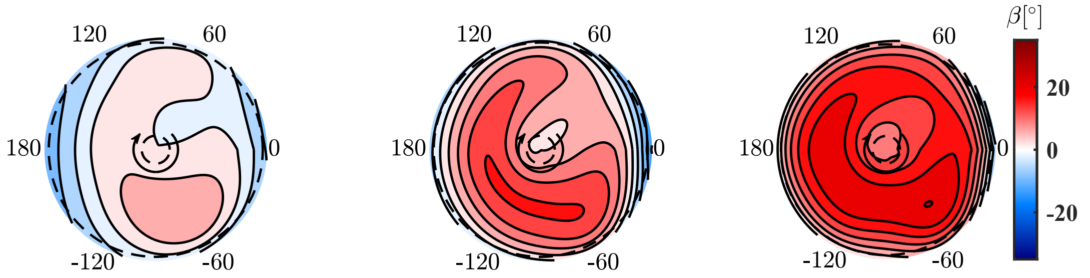

(a) $\mu = 2.45$ (b) $\mu = 5.84$ (c) $\mu = 8.87$

Fig. 4.22: Velocity angle distribution on the shroud inlet plane with different μ. Positive β indicates flow entering the shroud, and negative β means flow exiting the shroud.

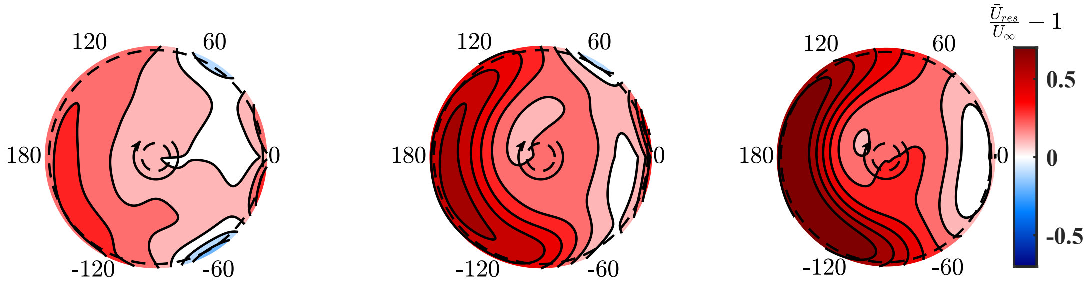

(a) $\mu = 2.45$ (b) $\mu = 5.79$ (c) $\mu = 8.87$

Fig. 4.23: Mean resultant velocity distribution at shroud inlet plane with different μ.

Figure 4.22 illustrates the velocity angle distribution at the shroud inlet plane. Except for the region close to the edge of the shroud, β is positive in most parts of the inlet. At low μ, higher β are observed on the advancing side. As μ increases, the high-β region shifts towards the front ($\theta|_{\beta_{max}}$ tends to $-180°$ in Table 4.1). To visualize the overall effect of μ on the mean velocities at the inlet, we define the average of the velocity angle and mean axial velocity on the measuring plane as $\tilde{\beta}$ and $\tilde{V}$, respectively. As shown in Table 4.2, both parameters increase with the increase of μ, indicating that more flow is redirected into the axial direction.

Figure 4.23 shows the distribution of mean resultant velocity $\overline{U}_{res} = \sqrt{\overline{U}^2 + \overline{V}^2}$ on the shroud inlet plane. The resultant velocity is normalized by U_∞. The contour reveals that the flow is accelerated at the inlet except for two small regions near $\theta = \pm 60°$. The resultant velocity is higher near the front than at the rear, and it increases with respect to μ.

4.3.2 Exit Mean Velocity Distribution

The exit mean velocity measurement was taken on the plane 5 mm below the shroud's exit plane. The axial and streamwise mean velocity distribution with a stationary rotor ($\mu = 0$) are shown in Figure 4.24. The distribution of the two velocity components is symmetric about the $180° - 0°$ line. The mean axial velocity distribution is similar to the inlet, with the flow entering the shroud at around $\theta = \pm 90°$. This similarity shows that the flow around the shroud with a stationary rotor is symmetric about the half-height plane of the shroud ($y/H = -0.5$). The mean streamwise velocity is higher than U_∞ in most of the region at the exit except the portion near the rear. The low-$\overline{U}$ region is smaller at the exit than the inlet.

Figure 4.25 demonstrates the mean axial velocity distribution at three different μ. For edgewise flight conditions, the flow exits the shroud in the rear half, and the

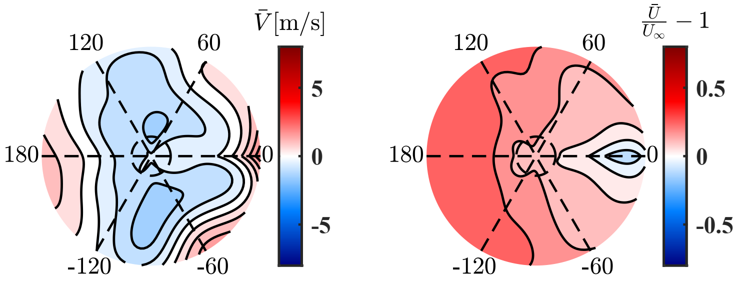

(a) Axial (b) Streamwise

Fig. 4.24: Mean axial and streamwise velocity distribution at shroud exit plane with $\mu = 0$. (a)Red area means velocity out of the shroud, blue means velocity in. (b)Red area means velocity higher than U_∞, and blue means lower. The dashed line and circle are the stator blades and hub. The velocity distribution is viewed from the shroud inlet (-ve Y direction) and U_∞ from left to right.

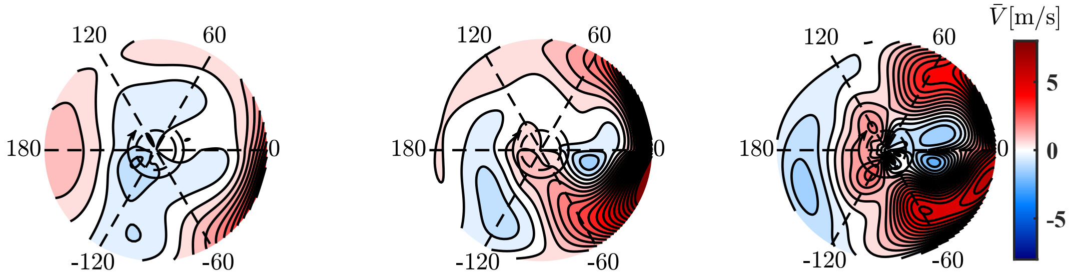

(a) $\mu = 2.45$ (b) $\mu = 5.69$ (c) $\mu = 8.85$

Fig. 4.25: Mean axial velocity distribution at shroud exit plane with different μ. The arrow indicates the clockwise rotation of the rotor.

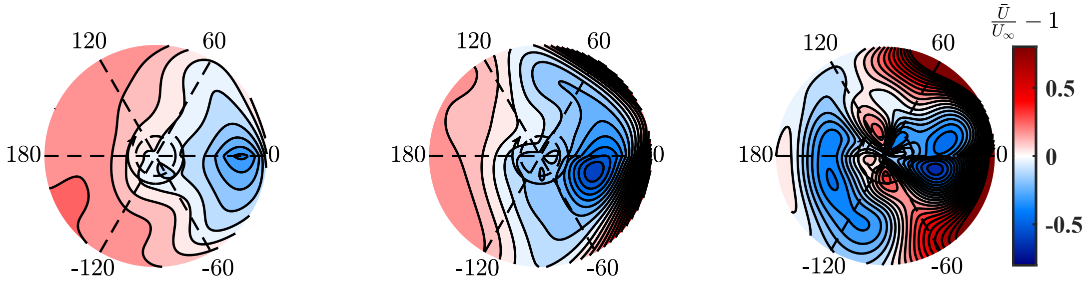

(a) $\mu = 2.45$ (b) $\mu = 5.69$ (c) $\mu = 8.85$

Fig. 4.26: Mean streamwise velocity distribution at shroud exit plane with different μ.

outflow velocity increases with the increase of μ. This indicates that the flow follows the rear part of the shroud's inner surface and exits near the rear. The flow enters the shroud from the plane in the front half, and this region shifts further towards the front end with the increase of μ. There is also a negative $\overline{V}$ region formed at $r/R = 0.5$, $\theta = 0°$, showing that the flow enters the shroud from the exit plane, which, we postulate, could be originated from the 3D recirculation in the wake zone of the hub (shown in Figure 4.27). Further flow visualization and measurements could be taken to verify this idea.

The mean streamwise velocity distribution at the shroud exit is shown in Figure 4.26. In the edgewise flight condition, this distribution stays symmetric about

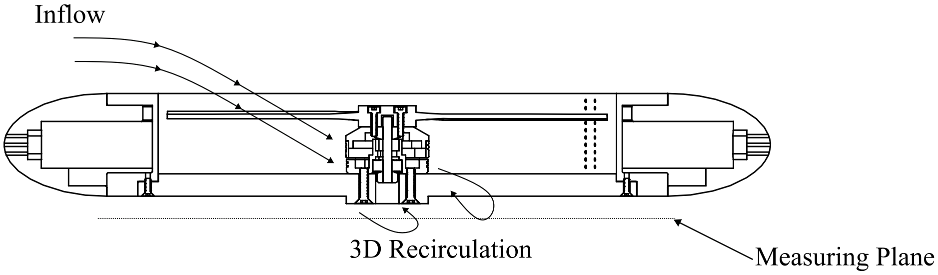

Fig. 4.27: The schematic of the wake of the hub

the centerline. With the increase of μ, the lower velocity region expands in the rear half until $\mu = 5.84$. With a further increase of μ, the low-velocity region is split into two parts, one in the rear and the other in the front.

4.3.3 Inlet Turbulence Intensity and Turbulence Kinetic Energy Distribution

Figure 4.28 shows the axial and streamwise turbulence intensity distribution on the shroud inlet plane when the rotor is stationary ($\mu = 0$). The distribution is symmetric about the centerline, with lower turbulence intensity at the front and higher turbulence intensity near the rear. The maximum I_V and I_U are observed near the rotor hub, with a magnitude of I_V =20% and I_U =25%. Comparing the two subplots indicates that the turbulence intensity is higher in the streamwise direction than in the axial direction.

Figure 4.29 and Figure 4.30 show the turbulence intensity distribution of the axial and streamwise velocities at the inlet plane. In edgewise flight, the distribution remains symmetric about the centerline, and the turbulence intensity over the measuring plane decreases with increasing μ. In the low μ regime, the maximum axial and streamwise velocity fluctuations occur at $\theta = \pm 60°$ near the edge of the shroud inlet. The turbulence intensity near the center tends to be lower for both velocity components than the outer region, except at very low μ. As μ increases, the I_V distribution becomes more axisymmetric about the rotor axis, indicating that the increasing dominance of the rotor-induced flow reduces the asymmetry generated by the edgewise inflow. This distribution should be completely axisymmetric in the hovering case, where μ approaches ∞. Comparing Figure 4.29 and 4.30 reveals that in edgewise flight, the turbulence intensity in the streamwise component is lower than in the axial component.

Given that velocity fluctuations are present in a turbulent flow, one can define the energy of the fluid based on these fluctuations, known as turbulent kinetic energy, shown in Equation (4.19).

$$K = \frac{1}{2}[\overline{(U')^2} + \overline{(V')^2}]. \tag{4.19}$$

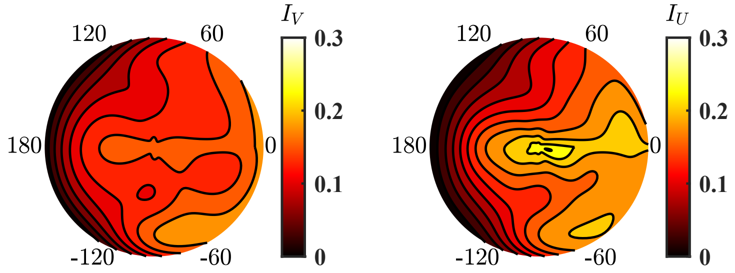

(a) Axial (b) Streamwise

Fig. 4.28: Axial and streamwise turbulence intensity distribution at shroud inlet plane with $\mu = 0$.

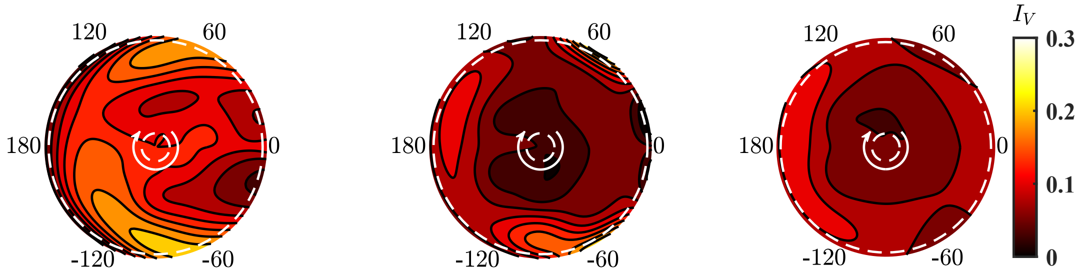

(a) $\mu = 2.45$ (b) $\mu = 5.79$ (c) $\mu = 8.87$

Fig. 4.29: Distribution of axial turbulent intensity at shroud inlet plane with different μ.

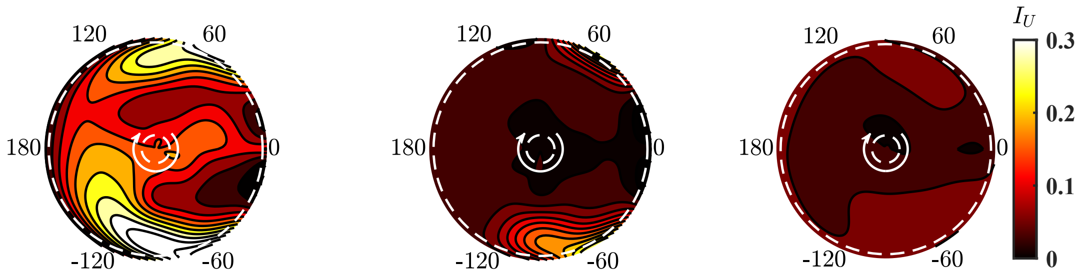

(a) $\mu = 2.45$ (b) $\mu = 5.79$ (c) $\mu = 8.87$

Fig. 4.30: Distribution of streamwise turbulent intensity at shroud inlet plane with different μ.

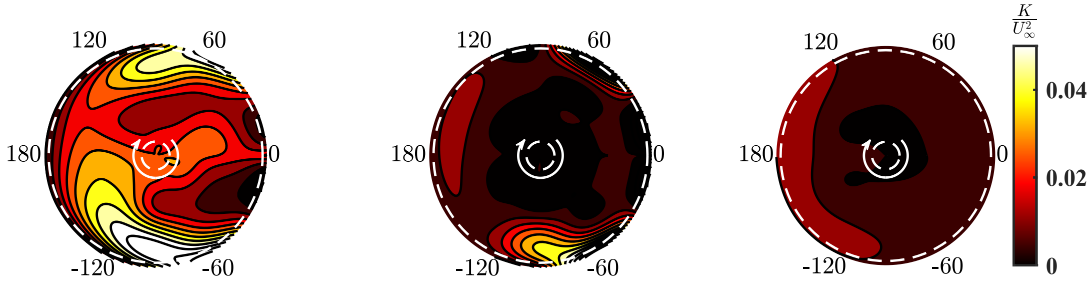

(a) $\mu = 2.45$ (b) $\mu = 5.79$ (c) $\mu = 8.87$

Fig. 4.31: Distribution of turbulence kinetic energy at shroud inlet plane with different μ.

where $\overline{(U')^2}$ and $\overline{(V')^2}$ are the variance of U and V, respectively. The turbulent kinetic energy was normalized by U_∞^2. Figure 4.31 illustrates the distribution of normalized K at the inlet. Similar to the turbulent intensities, the distribution of K is mostly symmetric about the $180° - 0°$ line and is slightly higher on the advancing side. When μ is low, higher K could be observed at $\theta = \pm 60°$. With the increase of μ, the overall turbulent kinetic energy on the measuring plane reduces, and the distribution becomes more axisymmetric about the rotor axis with lower K near the hub. As shown in Table 4.2, the averaged K/U_∞^2 over the measuring grid at the inlet $\tilde{K}/U_\infty^2$ exhibits a descending trend with respect to μ.

4.3.4 Elemental Thrust Distribution

The elemental thrust could be resolved based on Glauerts' momentum theory (Glauert, 1935) for a propeller in oblique inflow. The elemental thrust on the rotor is defined as

$$dT = 2\rho\overline{V}(r,\theta)\sqrt{\overline{U}(r,\theta)^2 + \overline{V}(r,\theta)^2}dA, \tag{4.20}$$

where

$$dA = rdrd\theta. \tag{4.21}$$

To apply this theory, the velocity measured is assumed to be the velocity on the rotor plane.

Figure 4.32 illustrates the elemental thrust (dT) distribution for three test cases with different μ. Unlike the hovering cases, the dT is not uniform at a specific radial location. At low μ, the elemental thrust is higher on the advancing side of the rotor. With μ increases, the high dT region shifts towards the front half of the shroud, and the magnitude of dT increases. This elemental thrust distribution indicates that the front and advancing halves of the rotor generate higher thrust than the other regions, giving rise to a nose-up pitching moment and a rolling moment on the rotor. With the increase of μ, the high dT region shifts towards the front end ($\theta|_{dT_{max}}$ tends to $-180°$ in Table 4.1). The non-uniform distribution of elemental thrust moves the center of thrust to the lower-left quadrant ($180° \leq \theta \leq -90°$) on the rotor plane except for low μ cases (when $\mu \leq 3.36$, the thrust center in the lower-right quadrant), and it shifts further to the front when μ increases ($\theta|_{thrust\_center}$ tends to $-180°$ in Table 4.1).

An estimation of rotor thrust could be obtained by summing dT on the rotor disk area.

$$T^V = \int_0^{2\pi}\int_0^R 2\rho\overline{V}(r,\theta)\sqrt{\overline{U}(r,\theta)^2 + \overline{V}(r,\theta)^2}r\,drd\theta. \tag{4.22}$$

The estimated thrust coefficient C_T^V could also be obtained by normalizing the thrust estimated thrust force by the tip velocity and the disk area of the rotor. As shown in Figure 4.33, the estimated thrust coefficient from velocity measurement has a descending trend with respect to μ. This trend is consistent with the results from the aerodynamic load measurement. The distance between the measuring and rotor planes could contribute to the disparity between the estimated and measured results.

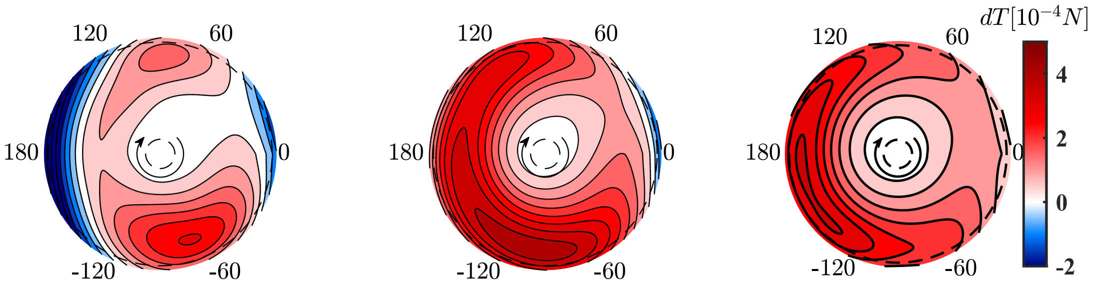

(a) $\mu = 2.45$ (b) $\mu = 5.79$ (c) $\mu = 8.87$

Fig. 4.32: Elemental thrust distribution with different μ. The color shows the direction of axial velocity: red area means velocity into the shroud, blue means velocity out of the shroud

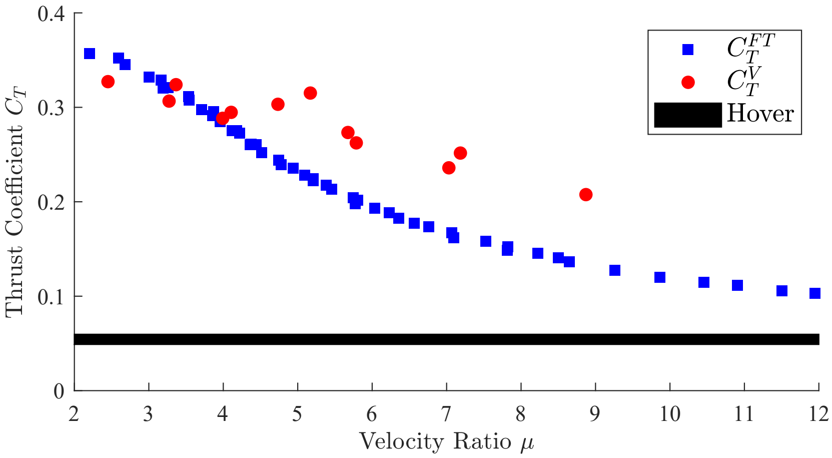

Fig. 4.33: Estimated and measured thrust coefficient at various μ

This difference could potentially be mitigated by moving the hot-wire probe closer to the rotor plane.

The nose-up pitching moment could be estimated by summing xdT over the measuring grid. The estimated pitching moment could be calculated as

$$M^V_{Pitch} = \int_0^{2\pi} \int_0^R 2\rho\overline{V}(r,\theta)\sqrt{\overline{U}(r,\theta)^2 + \overline{V}(r,\theta)^2} r^2 cos(\theta)\, dr d\theta \qquad (4.23)$$

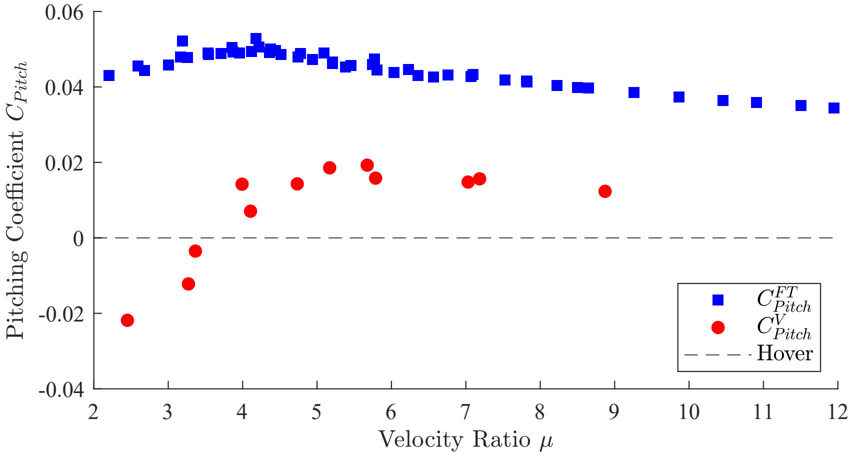

Fig. 4.34: Estimated and measured pitching moment coefficient at various μ

The estimated pitching moment coefficient C^V_{Pitch} at various μ is shown in Figure 4.34. C^V_{Pitch} exhibits an increasing trend at low μ and decreases afterward, similar to the trend observed in aerodynamic load measurements (C^{FT}_T and C^{FT}_{Pitch}). The estimated thrust coefficient decreases with a lower slope and is higher than the measured results except when $\mu < 4$. The estimated pitching coefficient is consistently lower than the measured results at all tested μ and is negative (nose-down pitch) when $\mu < 4$. This nose-down pitch estimation could originate from the negative axial velocity measurement near the front end for low μ cases. The distance between the measuring and rotor planes could contribute to the disparity between the estimated and measured results. This difference could potentially be mitigated by moving the hot-wire probe closer to the rotor plane. Additionally, performing velocity measurements at various distances above the rotor plane and curve-fitting the results could improve the estimation accuracy.

4.4 Spectra

The high-frequency response of the hot-wire measurements allows us to conduct spectral analysis of the velocity field. This analysis reveals the energy cascade of the flow with respect to frequency, offering insights into flow structure and turbulence characteristics. With a sampling frequency of $f_s = 20$ kHz and a sampling period of

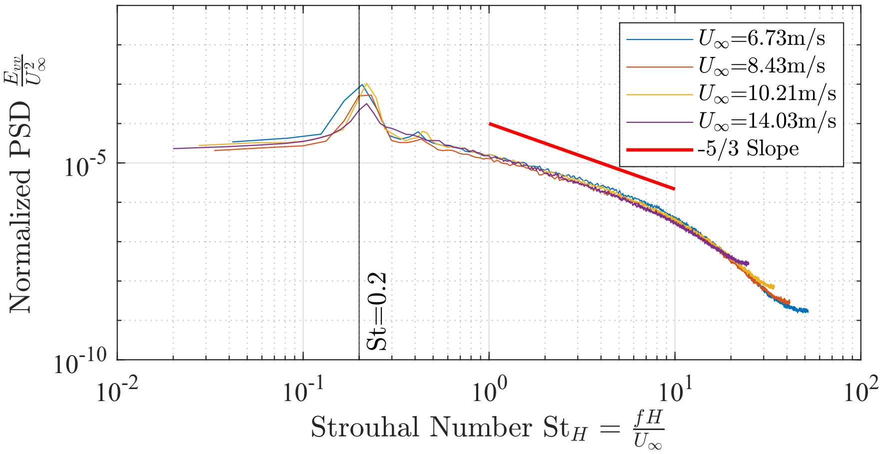

Fig. 4.35: Power spectral density versus Strouhal number at the center point $r/R = 0.5$ $\mu = 0$

$t_s = 20$ s, the power spectral density (PSD) can be obtained by applying the Fourier transform to the velocity data.

Figure 4.35 shows the power spectra of the streamwise velocity with a stationary rotor ($\mu = 0$) at $r/R = 0.5$, $\theta = 0°$. The PSD is normalized by U_∞^2. The Strouhal Number ($\mathrm{St}_H = \frac{fH}{U_\infty}$) is frequency normalized by the shroud height H and edgewise velocity U_∞. At all four edgewise velocities, PSD plateaus at low frequency, and the power cascades follow the $-5/3$ power law in the inertial subrange, which indicates that the flow has turbulence characteristics. The spectra also have a spike at $\mathrm{St}_H \approx 0.2$. Similar spectra could also be obtained at all the axial and streamwise velocities measuring points. This Strouhal number is consistent with vortex shedding type instabilities, which in this case are created by the separation of the shear layer from the inner front of the shroud.

For the edgewise flight condition, the spikes could be observed at the blade passing frequency (BPF) and its harmonics for all velocity ratios. Figure 4.36 demonstrates the power density spectra at $r/R = 0.5$, $\theta = 0°$ with three different velocity ratios. At $\mu = 2.45$, the energy cascade still shows a -5/3 slope in the inertial subrange and is superimposed with spikes at BPFs. However, when μ increases to 5.79 and 8.87, the spectra no longer follow the -5/3 power law and are less turbulent. The PSD level in the low-frequency range decreases with increasing μ. For all three cases, the hump

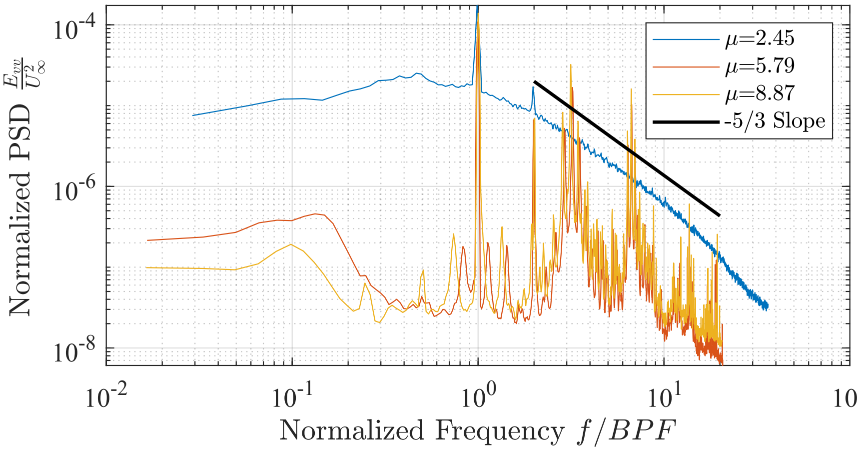

Fig. 4.36: Power spectral density versus f/BPF at $r/R = 0.5$ $\theta = 0°$ at three different μ

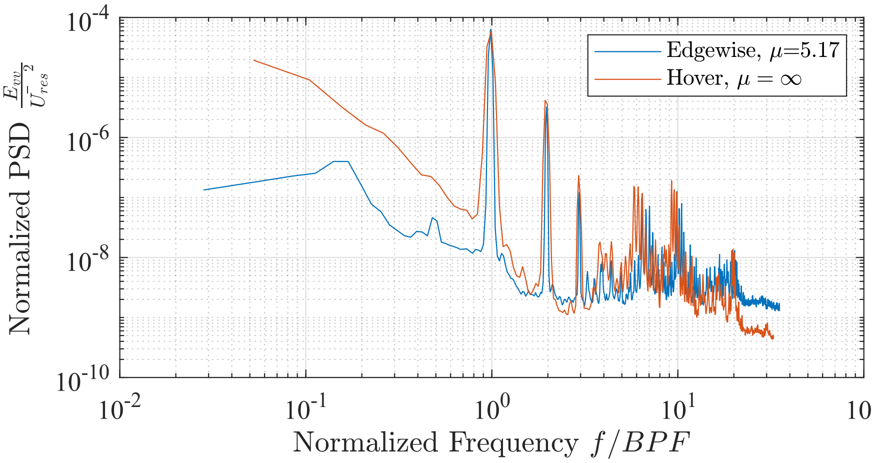

Fig. 4.37: Power spectral density at $r/R = 0.5$ for hover and edgewise flight

caused by vortex shedding in $\mu = 0$ case does not occur at $\mathrm{St}_H \approx 0.2$, indicating that the shed vortex structure is either not present in this measuring plane when the rotor rotates or has disappeared entirely. The latter is more likely, given that the flow at higher μ is dominated by axial effects induced by the rotor, which do not have any means of creating a vortex-shedding type flow.

High-frequency features could be observed in the spectra plots when the rotation of the rotor dominates the flow (high μ). To investigate the source of these high-

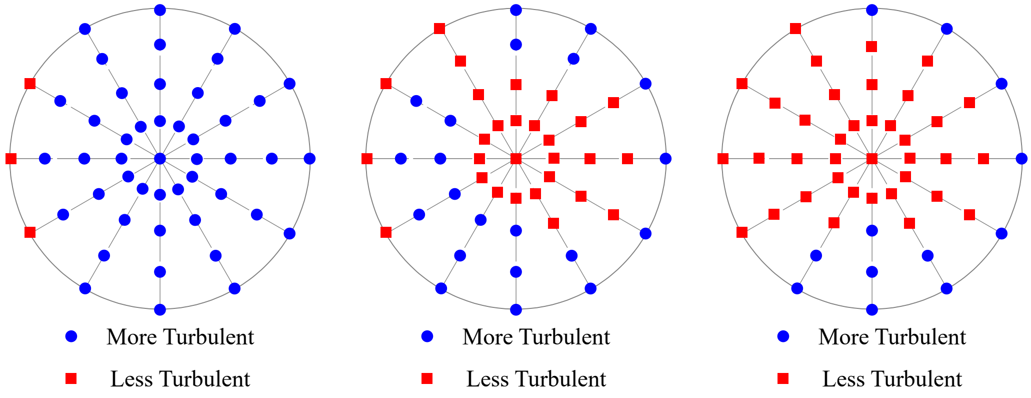

(a) $\mu = 2.45$ (b) $\mu = 5.79$ (c) $\mu = 8.87$

Fig. 4.38: Phase map showing if the flow is more turbulent for different μ

frequency features, we performed a velocity measurement on the same grid for the shrouded rotor hovering at 4590 RPM. For comparison, the mean resultant velocity $\overline{U}^2_{res}$ was used to normalize the PSD. As shown in Figure 4.37, the PSD curves in the high-frequency regime occur at similar frequencies and collapse. Additionally, Figure 4.39 indicates that these humps appear at all measuring locations within a similar frequency range. These findings suggest that the vibration of the testing rig and wind tunnel structure was transmitted to the traverse, causing the hot-wire probe to vibrate during the measurement. This vibration likely introduced a source of error in the experiment. To mitigate this issue, we recommend adding a damper under the traverse to further enhance the experimental setup.

The turbulence spectra at the inlet vary with the velocity ratios and locations. Figure 4.39 shows the spectra of all 49 measuring locations at $\mu = 2.45$, 5.79, and 8.87. Clear differences are observed among spectra at different measuring locations. At $\mu = 2.45$, most locations have spectra with a -5/3 slope in the inertial subrange, which could be considered a more turbulent flow (similar to the $\mu = 2.45$ case in Figure 4.36). As the rotor-induced flow becomes dominant (μ increases), more spectra exhibit less turbulence, with the -5/3 slope disappearing (similar to the $\mu = 8.87$ case in Figure 4.36).

Figure 4.38 presents a phase diagram for classifying these two types of spectra on the measuring plane. This classification, based on visual inspection, suggests a trend where the increase in μ leads to the diminishing of turbulent regions. At $\mu = 5.79$ and 8.87, the flow tends to be less turbulent near the hub, consistent with the turbulent intensity and turbulent kinetic energy distribution (Figures 4.29 and 4.31), indicating reduced flow fluctuations in that region. A final interesting observation is that the regions that remain turbulent as μ increases are located towards the outer edge of the shroud and where the blade is rotating directly into the edgewise flow i.e., $\theta = -90°$. The results consistently indicate that there is a transition between edgewise-dominated flow (lower μ), where the inflow is highly turbulent due to flow shedding from the edge of the shroud, and axial-dominated flow at higher μ, where the flow has less turbulent kinetic energy and does not exhibit turbulent like spectra.

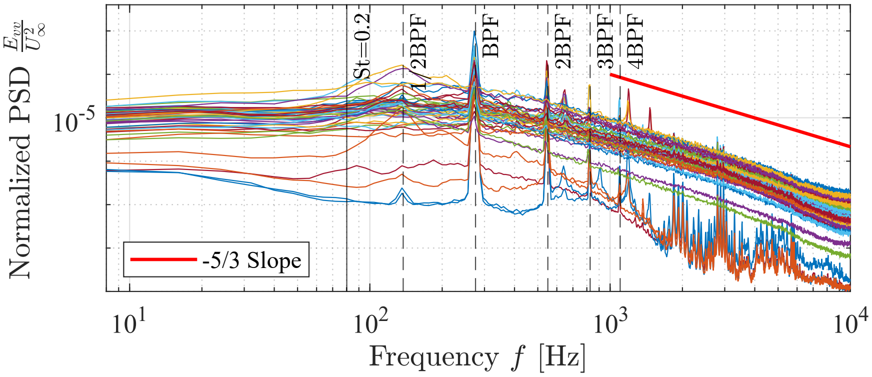

(a) $\mu = 2.45$

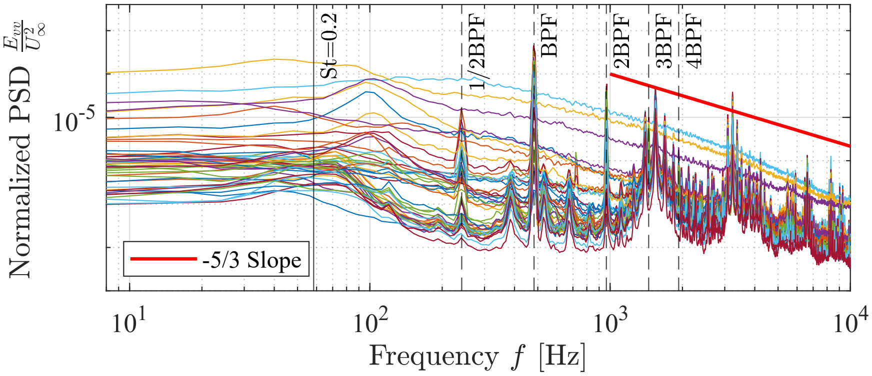

(b) $\mu = 5.79$

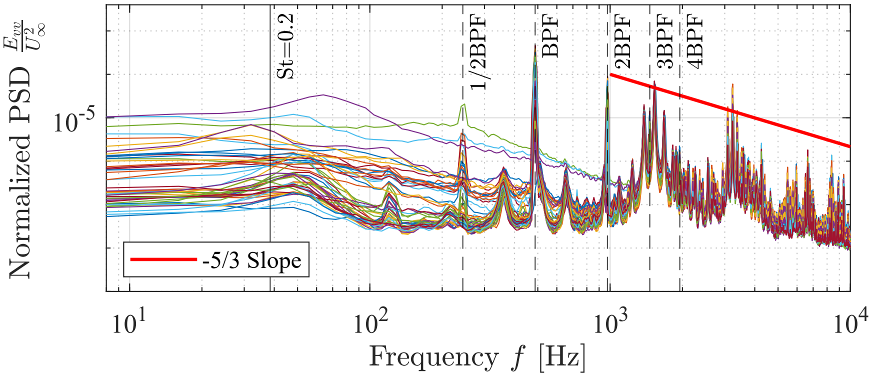

(c) $\mu = 8.87$

Fig. 4.39: Power spectral density at all 49 measuring positions with different μ

Chapter 5

Future Work

The objective of the thesis was to investigate how the aerodynamic performance of a shrouded rotor changed as the ratio between the edgewise velocity and the rotor velocity increased. Additional tests focusing on both aerodynamics and aeroacoustics could be conducted using the current setup. Further aerodynamic measurements could aim to separate the loads between the shroud and the rotor. For acoustic measurements, two key areas could be investigated: the wall pressure spectra on the shroud's inner surface and the sound pressure levels around the shrouded rotor.

5.1 Wall-Pressure Spectra

The wall-pressure spectra on the shroud's inner surface provide crucial information for acoustic modeling of the far-field noise. However, the sampling frequency of mean pressure measurements is limited due to the filtering effect of rubber tubes and the pressure scanner. To overcome this limitation, remote microphone sensing techniques can be implemented for high-frequency pressure measurements.

Microphones are widely used to measure pressure fluctuations because of their high sampling frequency (Guan *et al.* (2016)). These probes need to be placed close to the sensing area. However, due to size limitations, microphones often cannot access surfaces on scaled wind tunnel models with complex geometry and curvature. The remote microphone sensing technique addresses this issue by relocating the microphone away from the sensing surface using a miniature metal tube and a 1-meter section

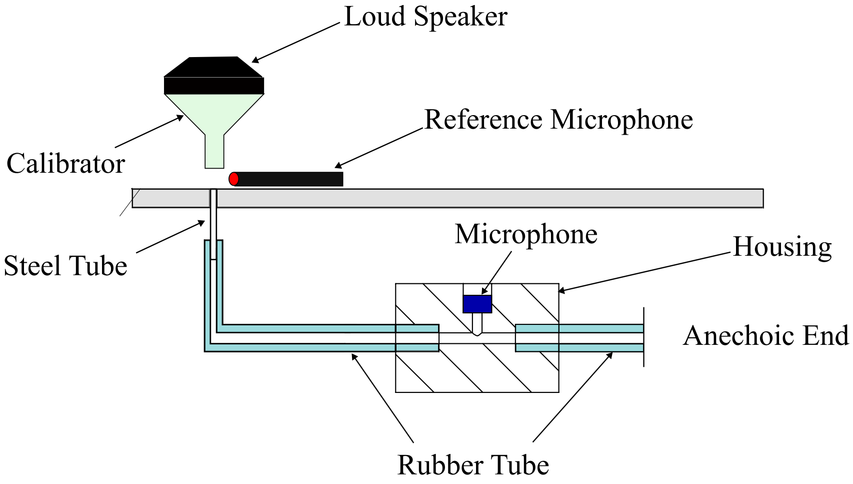

Fig. 5.1: The schematics of remote microphone sensing calibration (adapted from Botero-Bolívar *et al.* (2023))

of rubber tube. These tubes are connected to a probe housing with a Knowles FG 23329-P07 microphone installed. The anechoic end of the tube can be connected to a pressure scanner using a 3-meter rubber tube. With this setup, the microphone can achieve a sampling frequency of up to 10 kHz, facilitating high-frequency pressure measurements on challenging surfaces.

Due to the distance between the sensing probe and the measuring surface, there would be a phase lag and a magnitude change in the readings. Therefore, a transfer function must be determined in the calibration process (Botero-Bolívar *et al.* (2023)). A GRAS 40HP free-field microphone is used as a reference, and an FR8 loudspeaker acts as a noise source and provides white noise in the calibration process. Figure 5.1 shows the schematics of the calibration. The noise from the loudspeaker goes through the converging cone and reaches the pressure hole at the measuring location. The reference and measuring microphone sense the same noise simultaneously, and the transfer function could be obtained by comparing the two signals.

The pressure taps on the shroud could be used in the wall-spectra measurement in the future.

5.2 Acoustic Measurements in Edgewise Flight

The setup could be placed in an anechoic wind tunnel and conduct acoustic measurements. Similar to the setup Go *et al.* (2023a) used in their study, a microphone array could be implemented around the shrouded rotor to measure the sound pressure level (SPL). By characterizing the spectra, the tonal and broadband noise signal could be analyzed and compared with the hovering cases and the open rotor cases. Combined with the wall pressure spectra, the noise sources on the shrouded rotor in edgewise flight could be studied.

Chapter 6

Conclusions

This study investigated the impact of the velocity ratio on both the performance and flow dynamics of a shrouded tail rotor during edgewise flight. To maintain consistency, the shroud, rotor, and stator geometry remained unchanged throughout the experiments. By comparing the hovering thrust of shrouded and open rotors, it was observed that the shroud enhances thrust performance during hover.

The aerodynamic load measurements demonstrated that the velocity ratio $\mu = \frac{V_{tip}}{U_\infty}$ is a decisive factor for the edgewise flight as the non-dimensional thrust, drag, pitching, and rolling moment collapse onto the same curve with respect to μ. The thrust coefficient C_T decreases with μ and approaches the hovering C_T at μ tends to ∞. The ratio between the thrust in edgewise flight and hovering thrust at specific rotating speeds has a descending trend with a horizontal asymptotic line of $TR = 1$. The drag caused by the rotation of the rotor was measured, and the non-dimensional drag coefficient C_D has an ascending trend at low μ, peaks at $\mu = 4.3$, and descends afterward. A nose-up pitching moment was observed in edgewise flight conditions and increases with the edgewise velocity U_∞ and the rotating speed. The pitching moment coefficient C_{Pitch} increases with $\mu < 4$ and decreases with higher μ. The rolling moment generated by the uneven thrust distribution on the advancing and retreating sides was also observed in the edgewise flight cases. The rolling moment coefficient C_{Roll} increases with μ and is insignificant compared with the pitching moment.

The pressure distribution on the shroud's inner surface was investigated. The mean pressure pattern has a clear trend with respect to μ. For all edgewise flight cases, a high-pressure region could be observed near the rear end of the shroud, and with the increase of μ, the depth location of the peak c_P point shifted towards the shroud exit, indicating that the redirect of the flow caused by the rotating of the rotor is stronger with higher μ. The maximum c_P magnitude also has an increasing trend with respect to μ. The tip leakage flow could be observed near the rotor plane, which is represented as a region with lower pressure than other heights at the same azimuthal location. The pressure in this region also decreases with the increase of μ. Furthermore, the investigation extended to the pressure drag exerted on the shroud's inner surface. The pressure drag coefficient follows a similar trend as the drag coefficient from the aerodynamic load measurements and is smaller in magnitude except when $\mu < 2.5$. The azimuthal distribution of the pressure drag shows that when $\mu < 11$, the pressure drag exerted on the front half of the shroud's inner surface dominates, and when $\mu > 11$, the rear half contributed more significantly to drag.

The velocities at the shroud's inlet and outlet surfaces were measured and analyzed. Unlike the hovering cases, the axial velocity at the inlet is higher in the front than in the rear half. The distribution of the axial component is also higher on the advancing side than on the retreating side. With the increase of μ, the region with higher axial velocity shifts towards the front end, and the magnitude of axial velocity increases. The streamwise component of velocity is higher near the front end as well, and the magnitude of this velocity component further increases with μ. At the shroud exit, the axial velocity enters the shroud near the front end and exits the shroud near the rear. The streamwise component of the exit velocity is lower in the rear half, which could be caused by the blockage of the stator hub and motor. The maximum axial and streamwise turbulence intensity is at $\theta = \pm 60^\circ$, and as μ increases, I_V distribution becomes more axisymmetric about the rotor axis. The elemental thrust distribution was also analyzed based on the inlet velocity and Glauerts' momentum theory. At low μ, dT is higher on the advancing side. With μ increases, the high dT region shifts towards the front end. The thrust and pitching moment were estimated by summing dT and xdT over the measuring grid, and the results showed the same trend as the aerodynamic load measurements. The distance between the measuring and rotor plane could contribute to the difference between the estimated and measured results.

The high-frequency velocity measurements allow the spectral study. For the stationary rotor cases, the power cascades follow the -5/3 power low and have spikes at a Strouhal number of $St_H = 0.2$, indicating a vortex shedding or shear-layer separation from the front of the shroud. The spikes are at the blade pass frequency (BPF) and its harmonics for the edgewise flight cases. The spectra vary with measuring locations and the velocity ratios. At low μ, when the edgewise flow dominates, most spectra have the -5/3 slope and are considered more turbulence. With the increase of μ, the spectra at more measuring locations became less turbulent.

The summary of this thesis can assist helicopter pilots in selecting optimal control inputs to enhance flight performance during edgewise flight conditions. Practically, for a helicopter in a climbing flight requiring a specific amount of tail rotor thrust to counteract the torque from its main rotor, the pilot has various options for adjusting the rotating speed and climbing speed. To minimize drag penalties and unwanted moments on the rotor during edgewise flight, a preferable solution is to reduce the μ value, which involves either decreasing the rotor's rotating speed or increasing the climbing velocity. This adjustment can also reduce the tip vortex and mitigate the movement of the stagnation point on the shroud's leading edge. However, it will result in the shrouded rotor ingesting more turbulent flow, potentially leading to unsteady loads on the rotor and increased noise emissions (Yao *et al.*, 2020).

References

AKTURK, ALI, & CAMCI, CENGIZ. 2010. Influence of tip clearance and inlet flow distortion on ducted fan performance in VTOL UAVs. *Pages 1443–1453 of: Annual Forum Proceedings-AHS International*, vol. 2. American Helicopter Society.

AKTURK, ALI, & CAMCI, CENGIZ. 2011. Tip clearance investigation of a ducted fan used in vtol uavs: Part 1—baseline experiments and computational validation. *Pages 331–344 of: Turbo Expo: Power for Land, Sea, and Air*, vol. 54679.

AKTURK, ALI, & CAMCI, CENGIZ. 2014. Lip separation and inlet flow distortion control in ducted fans used in VTOL systems. *Page V01AT01A027 of: Turbo Expo: Power for Land, Sea, and Air*, vol. 45578. American Society of Mechanical Engineers.

ANDERSON, JOHN. 2011. *EBOOK: Fundamentals of Aerodynamics (SI units)*. McGraw hill.

BOTERO-BOLÍVAR, LAURA, DOS SANTOS, FERNANDA L, VENNER, CORNELIS H, & DE SANTANA, LEANDRO D. 2023. Study of the development of a boundary layer using the remote microphone probe technique. *Experiments in Fluids*, **64**(4), 88.

CANEPA, EDWARD, CATTANEI, ANDREA, ZECCHIN, FABIO MAZZOCUT, MILANESE, GABRIELE, & PARODI, DAVIDE. 2016. An experimental investigation on the tip leakage noise in axial-flow fans with rotating shroud. *Journal of Sound and Vibration*, **375**, 115–131.

Cao, Chenkai, Zhao, Guoqing, Zhao, Qijun, & Wang, Bo. 2021. Numerical investigation and optimization for interior duct shape of ducted tail rotor. *Aerospace Science and Technology*, **115**, 106778.

Cao, Chenkai, Wang, Bo, Zhao, Guoqing, & Zhao, Qijun. 2023. Optimization of duct shape for improving aerodynamic performance of ducted tail rotor. *International Journal of Aeronautical and Space Sciences*, **24**(2), 341–357.

Christian, Andrew W, & Cabell, Randolph. 2017. Initial investigation into the psychoacoustic properties of small unmanned aerial system noise. *Page 4051 of: 23rd AIAA/CEAS aeroacoustics conference.*

Froude, Robert Edmund. 1889. On the part played in propulsion by differences of fluid pressure. *Trans. Inst. Naval Architects*, **30**, 390.

George, A Re. 1978. Helicopter noise: State-of-the-art. *Journal of Aircraft*, **15**(11), 707–715.

Glauert, Hermann. 1935. Airplane propellers. *Aerodynamic theory*, 169–360.

Glegg, Stewart, & Devenport, William. 2017. *Aeroacoustics of low Mach number flows: fundamentals, analysis, and measurement.* Academic Press.

Go, Sung Tyaek, Kingan, Michael J, Wu, Yan, & Sharma, Rajnish N. 2023a. Experimental and numerical investigation of the sound field produced by a shrouded UAV propeller. *Applied Acoustics*, **211**, 109523.

Go, Sung Tyaek, Kingan, Michael J, McKay, Ryan S, & Sharma, Rajnish N. 2023b. Turbulent inflow noise produced by a shrouded propeller. *Journal of Sound and Vibration*, **542**, 117366.

Gojon, Romain, Jardin, Thierry, & Parisot-Dupuis, Hélène. 2021. Experimental investigation of low Reynolds number rotor noise. *The Journal of the Acoustical Society of America*, **149**(6), 3813–3829.

Graf, Will, Fleming, Jonathan, & Ng, Wing. 2008. Improving ducted fan UAV aerodynamics in forward flight. *Page 430 of: 46th AIAA aerospace sciences meeting and exhibit.*

Grande, Edoardo, Romani, Gianluca, Ragni, Daniele, Avallone, Francesco, & Casalino, Damiano. 2022. Aeroacoustic investigation of a propeller operating at low Reynolds numbers. *AIAA Journal*, **60**(2), 860–871.

Guan, Yaoyi, Berntsen, Carl R, Bilka, Michael J, & Morris, Scott C. 2016. The measurement of unsteady surface pressure using a remote microphone probe. *JoVE (Journal of Visualized Experiments)*, e53627.

Gutin, L. 1948. On the sound field of a rotating propeller. *Physikalische Zeitschrit der Sowjetinion: Physical magazine of the Soviet Union volume 9 number 1*, **9**(NACA-TM-1195).

Halwick, Jason Michael. 2012. Implementation of blade element theory in CFD analysis of edgewise ducted fan vehicles.

Hiwada, Munehiko, Kawamura, Takao, MABUCHI, Ikuo, & KUMADA, Masaya. 1983. Some characteristics of flow pattern and heat transfer past a circular cylindrical cavity. *Bulletin of JSME*, **26**(220), 1744–1752.

Hook, R, Myers, L, & McLaughlin, D. 2011. Investigation on Flow Physics of Edgewise Ducted rotor Air Vehicles. *In: American Helicopter Society 67th Annual Forum, Virginia Beach, VA.*

Hrishikeshavan, Vikram. 2011. *Experimental investigation of a shrouded rotor micro air vehicle in hover and in edgewise gusts.* University of Maryland, College Park.

Hrishikeshavan, Vikram, & Chopra, Inderjit. 2012. Performance, flight testing of a shrouded rotor micro air vehicle in edgewise gusts. *Journal of Aircraft*, **49**(1), 193–205.

Jamaluddin, Nur Syafiqah, Celik, Alper, Baskaran, Kabilan, Rezgui, Djamel, & Azarpeyvand, Mahdi. 2024. Aerodynamic noise analysis of tilting rotor in edgewise flow conditions. *Journal of Sound and Vibration*, 118423.

Jang, Choon-Man, Fukano, Tohru, & Furukawa, Masato. 2003. Effects of the tip clearance on vortical flow and its relation to noise in an axial flow fan. *JSME International Journal Series B Fluids and Thermal Engineering*, **46**(3), 356–365.

Jimenez, Benjamin G, & Singh, Rajneesh. 2015. Effect of duct-rotor aerodynamic interactions on blade design for hover and axial flight. *Page 1030 of: 53rd AIAA Aerospace Sciences Meeting.*

Johnson, Wayne. 2013. *Rotorcraft aeromechanics.* Vol. 36. Cambridge university press.

Jordan, William A, Narsipur, Shreyas, & Deters, Robert. 2020. Aerodynamic and aeroacoustic performance of small uav propellers in static conditions. *Page 2595 of: AIAA AVIATION 2020 FORUM.*

Jørgensen, Finn E. 2001. How to measure turbulence with hot-wire anemometers: a practical guide.

Lakshminarayan, Vinod K, & Baeder, James D. 2011. Computational investigation of microscale shrouded rotor aerodynamics in hover. *Journal of the American Helicopter Society*, **56**(4), 1–15.

Leishman, Gordon J. 2006. *Principles of helicopter aerodynamics with CD extra.* Cambridge university press.

Malgoezar, Anwar MN, Vieira, Ana, Snellen, Mirjam, Simons, Dick G, & Veldhuis, Leo LM. 2019. Experimental characterization of noise radiation from a ducted propeller of an unmanned aerial vehicle. *International Journal of Aeroacoustics*, **18**(4-5), 372–391.

Marsden, Olivier, Bailly, Christophe, Bogey, Christophe, & Jondeau, Emmanuel. 2012. Investigation of flow features and acoustic radiation of a round cavity. *Journal of Sound and Vibration*, **331**(15), 3521–3543.

Martin, Preston, & Tung, Chee. 2004. Performance and flowfield measurements on a 10-inch ducted rotor VTOL UAV.

McCarthy, PW, & Ekmekci, A. 2022. Flow features of shallow cylindrical cavities subject to grazing flow. *Physics of Fluids*, **34**(2).

Misiorowski, Matthew, Gandhi, Farhan, & Oberai, Assad. 2018. Computational Analysis of Isolated and Embedded Ducted Rotors in Edgewise Flight. *Page 1527 of: 2018 AIAA Aerospace Sciences Meeting*.

Misiorowski, Matthew P, Gandhi, Farhan S, & Oberai, Assad A. 2019a. Computational analysis and flow physics of a ducted rotor in edgewise flight. *Journal of the American Helicopter Society*, **64**(4), 1–14.

Misiorowski, Matthew P, Gandhi, Farhan S, & Oberai, Assad A. 2019b. Computational study of diffuser length on ducted rotor performance in edgewise flight. *AIAA Journal*, **57**(2), 796–808.

Mouille, Rene, & Bourquardez, Gaston. 1970 (Apr. 14). *Helicopter steering and propelling device*. US Patent 3,506,219.

Oweis, Ghanem F, Fry, David, Chesnakas, Chris J, Jessup, Stuart D, & Ceccio, Steven L. 2006. Development of a tip-leakage flow part 2: comparison between the ducted and un-ducted rotor.

Pereira, J, & Chopra, I. 2006. Surface Pressure Measurements on an MAV-Scale Shrouded Rotor in Hover. *Page 1536 of: ANNUAL FORUM PROCEEDINGS-AMERICAN HELICOPTER SOCIETY*, vol. 62. AMERICAN HELICOPTER SOCIETY, INC.

Pereira, Jason L. 2008. *Hover and wind-tunnel testing of shrouded rotors for improved micro air vehicle design*. University of Maryland, College Park.

Qian, YuPing, Luo, YiWei, Hu, XuanYang, Zeng, ZeZhi, & Zhang, YangJun. 2022. Improving the performance of ducted fans for VTOL applications: A review. *Science China Technological Sciences*, **65**(11), 2521–2541.

Rankine, William John Macquorn. 1865. On the mechanical principles of the action of propellers. *Transactions of the Institution of Naval Architects*, **6**.

Schmitz, Fredric H, & Boxwell, Donald A. 1976. In-Flight Far-Field Measurement of Helicopter Impulsive Noise. *Journal of the American Helicopter Society*, **21**(4), 2–16.

Sheng, Chunhua, Zhao, Qiuying, & Bi, Naipei P. 2015. Numerical investigations of ducted fan hover performance for FIW applications. *Page 1935 of: 53rd AIAA Aerospace Sciences Meeting.*

Weisgerber, M, & Neuwerth, G. 2003. Influence of a helicopter tail rotor shroud on the interaction noise due to the main rotor vortices.

Wygnanski, I, & Newman, BG. 1961. General description and calibration of the McGill 3ft x 2ft low speed wind tunnel.

Yang, Yannian, Liu, Yu, Li, Yu, Arcondoulis, Eilas, & Wang, Yong. 2020. Aerodynamic and aeroacoustic performance of an isolated multicopter rotor during forward flight. *AIAA Journal*, **58**(3), 1171–1181.

Yao, Haoyu, Cao, Linlin, Wu, Dazhuan, Yu, Faxin, & Huang, Bin. 2020. Generation and distribution of turbulence-induced forces on a propeller. *Ocean Engineering*, **206**, 107255.

Yilmaz, Serdar, Erdem, Duygu, & Kavsaoglu, Mehmet S. 2015. Performance of a ducted propeller designed for UAV applications at zero angle of attack flight: An experimental study. *Aerospace Science and Technology*, **45**, 376–386.

Zawodny, Nikolas S, Boyd Jr, D Douglas, & Burley, Casey L. 2016. Acoustic characterization and prediction of representative, small-scale rotary-wing unmanned aircraft system components. *In: American Helicopter Society (AHS) Annual Forum.*

Zhang, T, Qiao, G, Smith, DA, Barakos, GN, & Kusyumov, A. 2021. Parametric study of aerodynamic performance of equivalent ducted/un-ducted rotors. *Aerospace Science and Technology*, **117**, 106984.

Appendix A

CAD Drawing of Setup

A.1 Explosive View of Shrouded Rotor Setup

Fig. A.1 shows the explosive view of the shrouded rotor setup. Fig. A.2 presents the bill of material of the setup, including the machined parts, 3D printed parts, fasteners, and a ball bearing. The shrouded rotor setup could be fixed to the ATI-Gamma load cell using four 18mm long M6 screws. The load cell is attached to the wind tunnel floor using four 12mm long M5 screws.

A.2 Detailed Drawing of Shrouded Rotor Parts

Fig. A.3 to A.10 present the detailed drawing of the machined and 3D printed parts. The machined parts are 6061-T6 aluminum alloy, and the 3D-printed parts are made of PLA filament.

A.3 Hotwire Positioning System

Fig. A.11 shows the detailed drawing of the support of the Dantec 55H25 hotwire probe holder. The probe holder is fastened to the support using two 6mm long M3 screws. The support attaches to the Unislide A15 linear traverse using two 6-32 × 1-4 screws. The two Unisilde A15 traverses connect with the X-Z traverse with a plate shown in Fig. A.12.

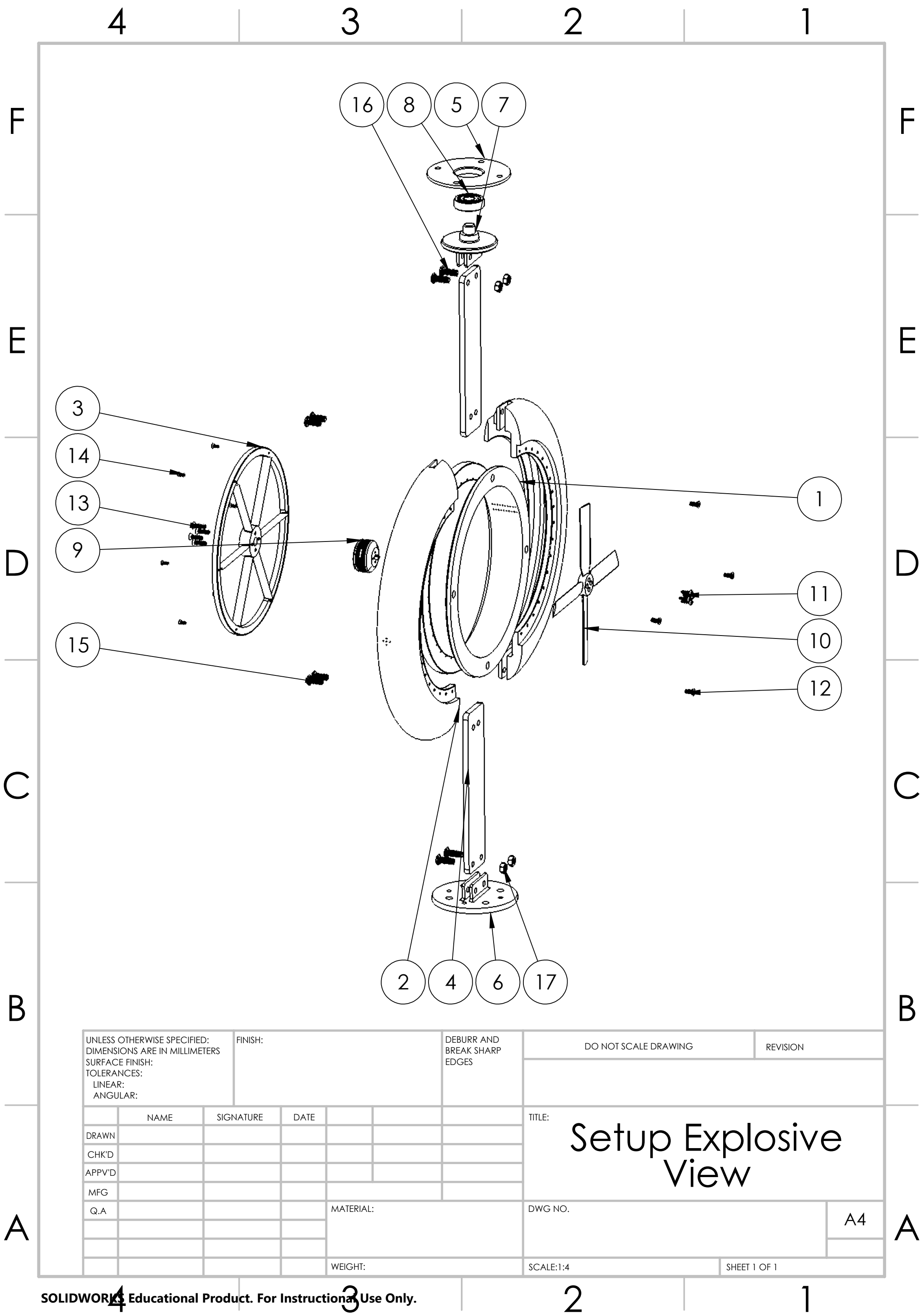

Fig. A.1: Shrouded Rotor Setup Explosive Drawing

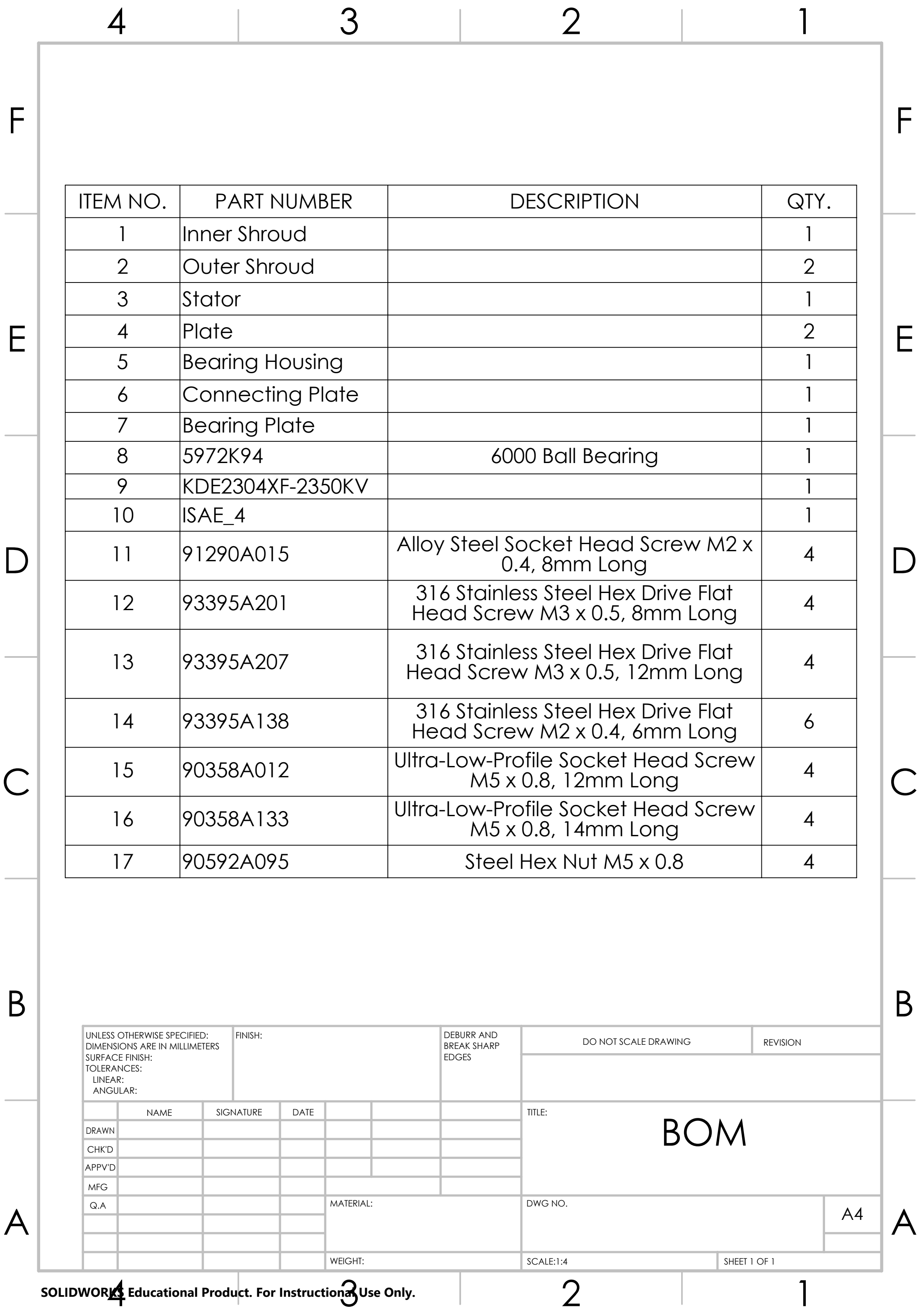

ITEM NO.	PART NUMBER	DESCRIPTION	QTY.
1	Inner Shroud		1
2	Outer Shroud		2
3	Stator		1
4	Plate		2
5	Bearing Housing		1
6	Connecting Plate		1
7	Bearing Plate		1
8	5972K94	6000 Ball Bearing	1
9	KDE2304XF-2350KV		1
10	ISAE_4		1
11	91290A015	Alloy Steel Socket Head Screw M2 x 0.4, 8mm Long	4
12	93395A201	316 Stainless Steel Hex Drive Flat Head Screw M3 x 0.5, 8mm Long	4
13	93395A207	316 Stainless Steel Hex Drive Flat Head Screw M3 x 0.5, 12mm Long	4
14	93395A138	316 Stainless Steel Hex Drive Flat Head Screw M2 x 0.4, 6mm Long	6
15	90358A012	Ultra-Low-Profile Socket Head Screw M5 x 0.8, 12mm Long	4
16	90358A133	Ultra-Low-Profile Socket Head Screw M5 x 0.8, 14mm Long	4
17	90592A095	Steel Hex Nut M5 x 0.8	4

UNLESS OTHERWISE SPECIFIED:
DIMENSIONS ARE IN MILLIMETERS
SURFACE FINISH:
TOLERANCES:
LINEAR:
ANGULAR:

FINISH:

DEBURR AND
BREAK SHARP
EDGES

DO NOT SCALE DRAWING

REVISION

	NAME	SIGNATURE	DATE
DRAWN			
CHK'D			
APPV'D			
MFG			
Q.A			

TITLE: BOM

MATERIAL:

DWG NO.

A4

WEIGHT:

SCALE:1:4

SHEET 1 OF 1

SOLIDWORKS Educational Product. For Instructional Use Only.

Fig. A.2: Bill of Material

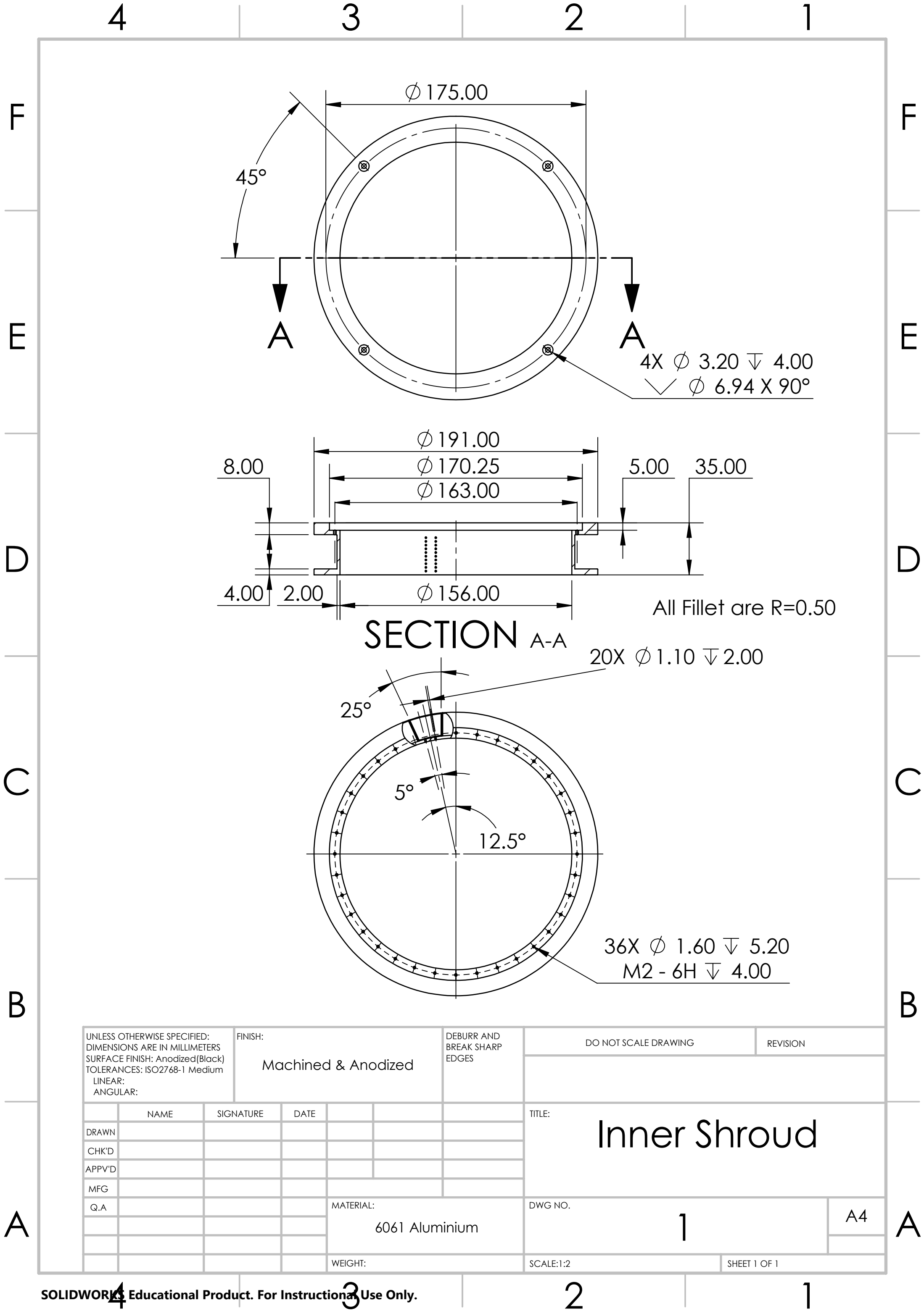

Fig. A.3: Inner Shroud
]

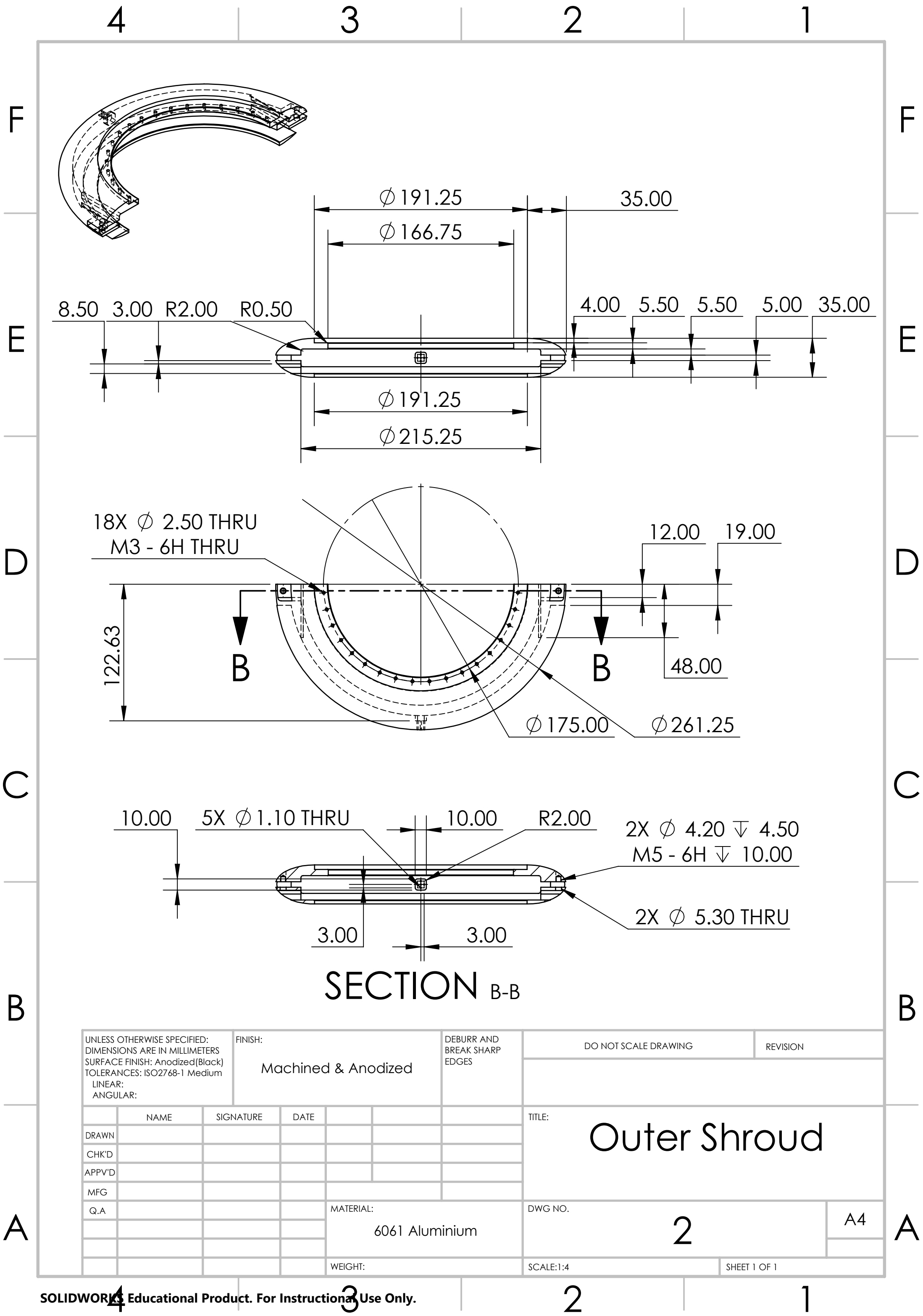

Fig. A.4: Outer Shroud

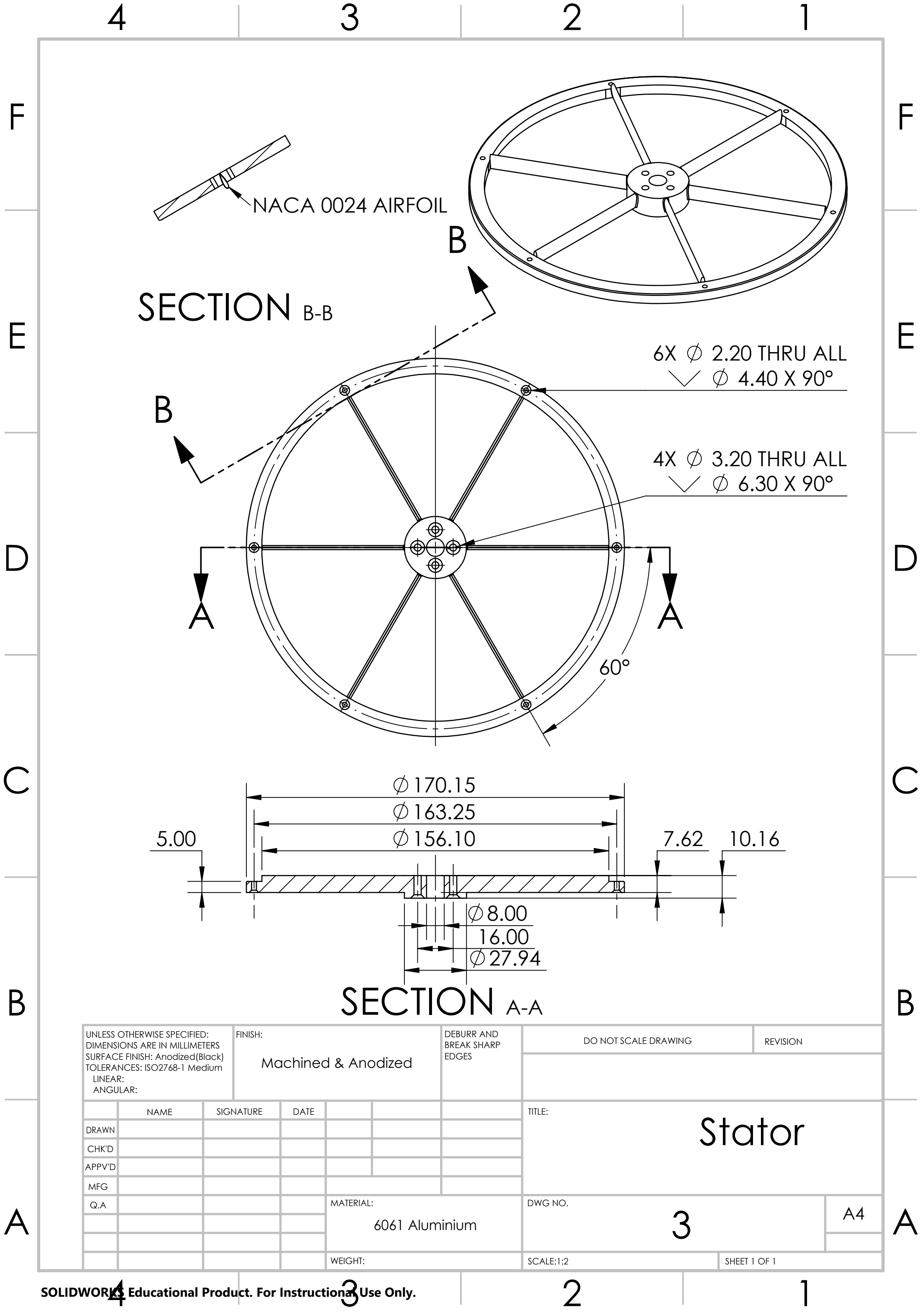

Fig. A.5: Stator

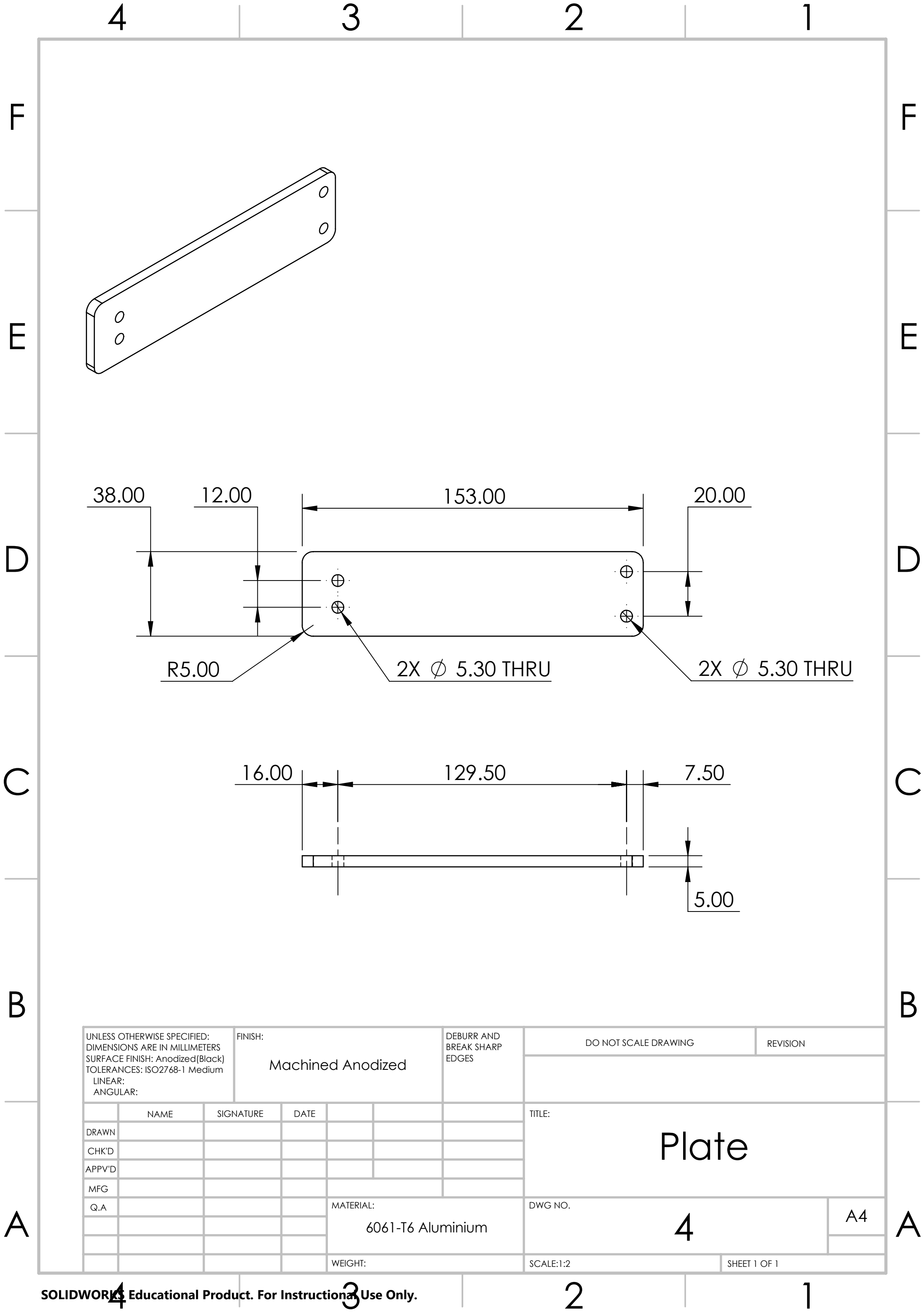

UNLESS OTHERWISE SPECIFIED:
DIMENSIONS ARE IN MILLIMETERS
SURFACE FINISH: Anodized(Black)
TOLERANCES: ISO2768-1 Medium
LINEAR:
ANGULAR:

FINISH: Machined Anodized

DEBURR AND BREAK SHARP EDGES

DO NOT SCALE DRAWING

REVISION

	NAME	SIGNATURE	DATE
DRAWN			
CHK'D			
APPV'D			
MFG			
Q.A			

TITLE: Plate

MATERIAL: 6061-T6 Aluminium

DWG NO. 4

A4

WEIGHT:

SCALE:1:2

SHEET 1 OF 1

Fig. A.6: Supporting Plate

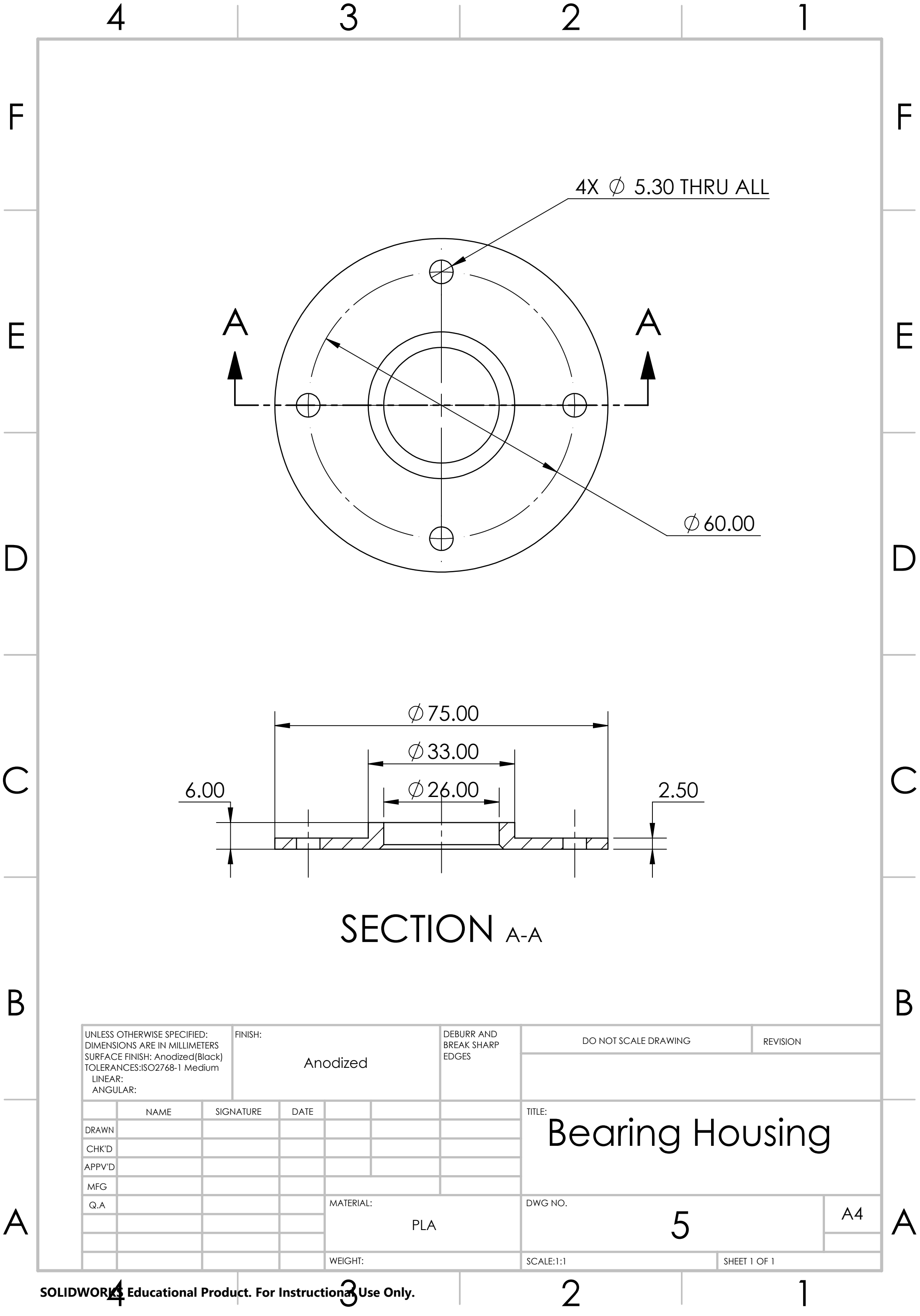

UNLESS OTHERWISE SPECIFIED:
DIMENSIONS ARE IN MILLIMETERS
SURFACE FINISH: Anodized(Black)
TOLERANCES:ISO2768-1 Medium
LINEAR:
ANGULAR:

FINISH: Anodized

DEBURR AND BREAK SHARP EDGES

DO NOT SCALE DRAWING

REVISION

	NAME	SIGNATURE	DATE
DRAWN			
CHK'D			
APPV'D			
MFG			
Q.A			

TITLE: Bearing Housing

MATERIAL: PLA

DWG NO. 5

A4

WEIGHT:

SCALE:1:1

SHEET 1 OF 1

Fig. A.7: Bearing Housing

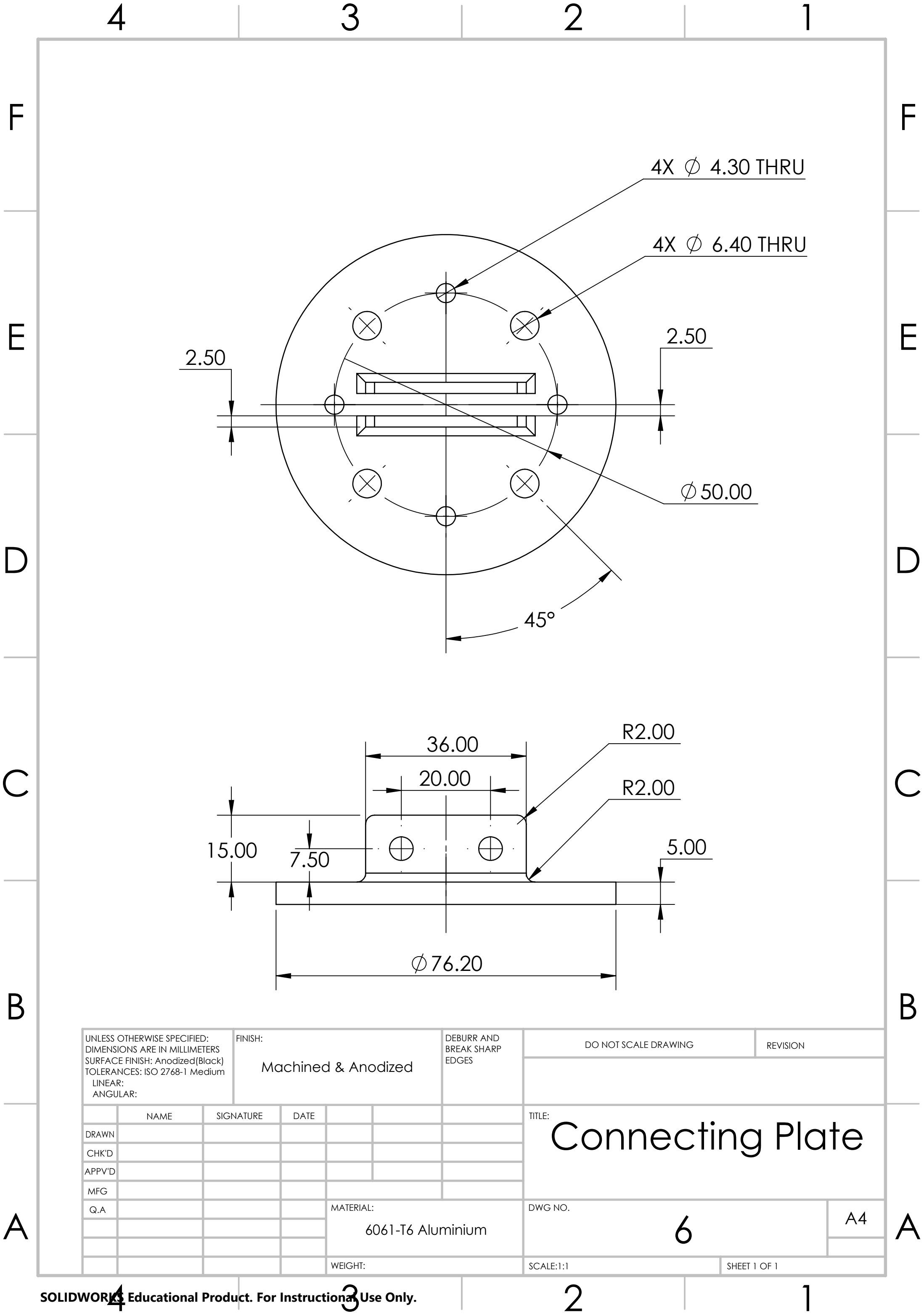

Fig. A.8: Connecting Plate

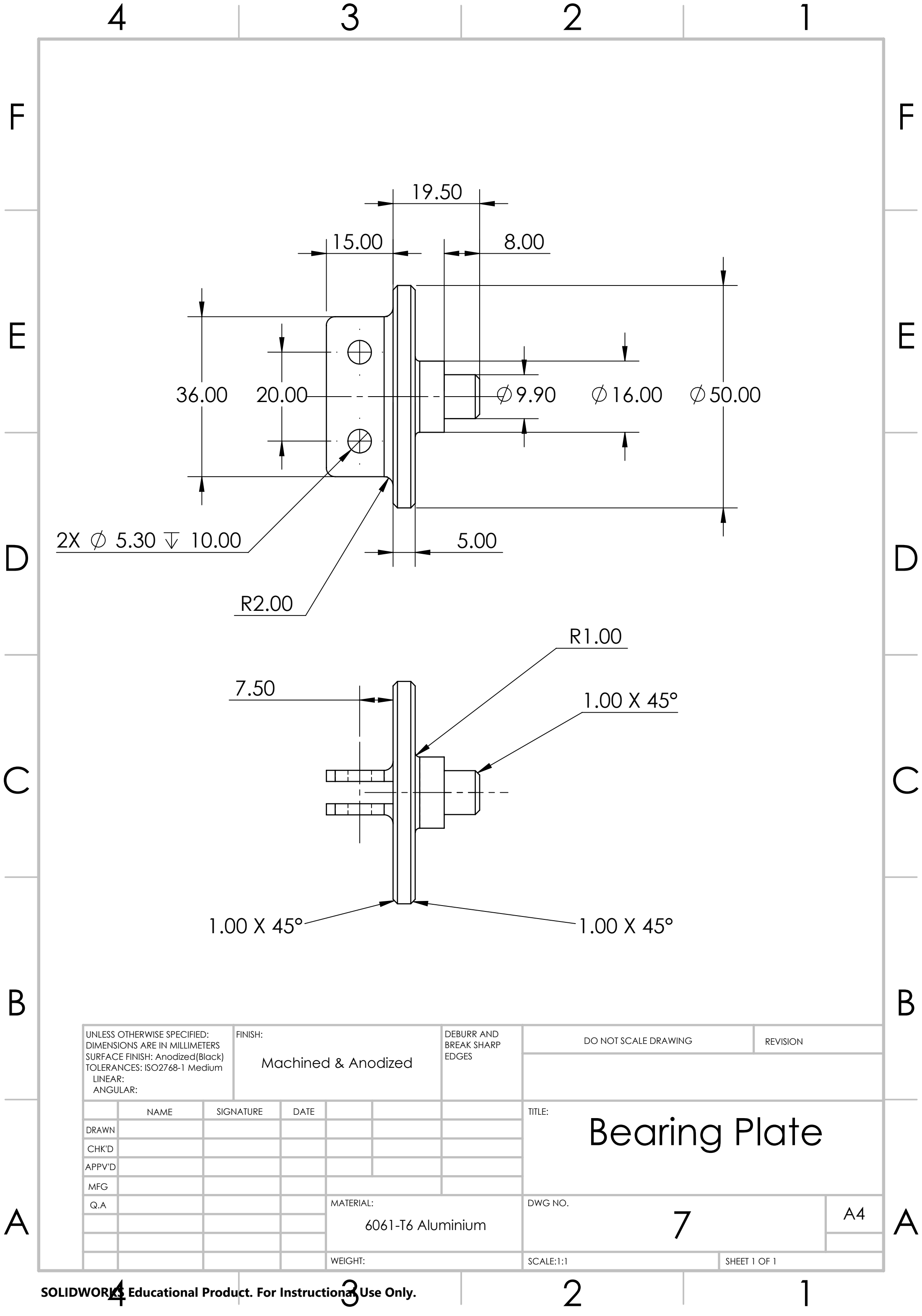

Fig. A.9: Connecting Plate for Bearing Side

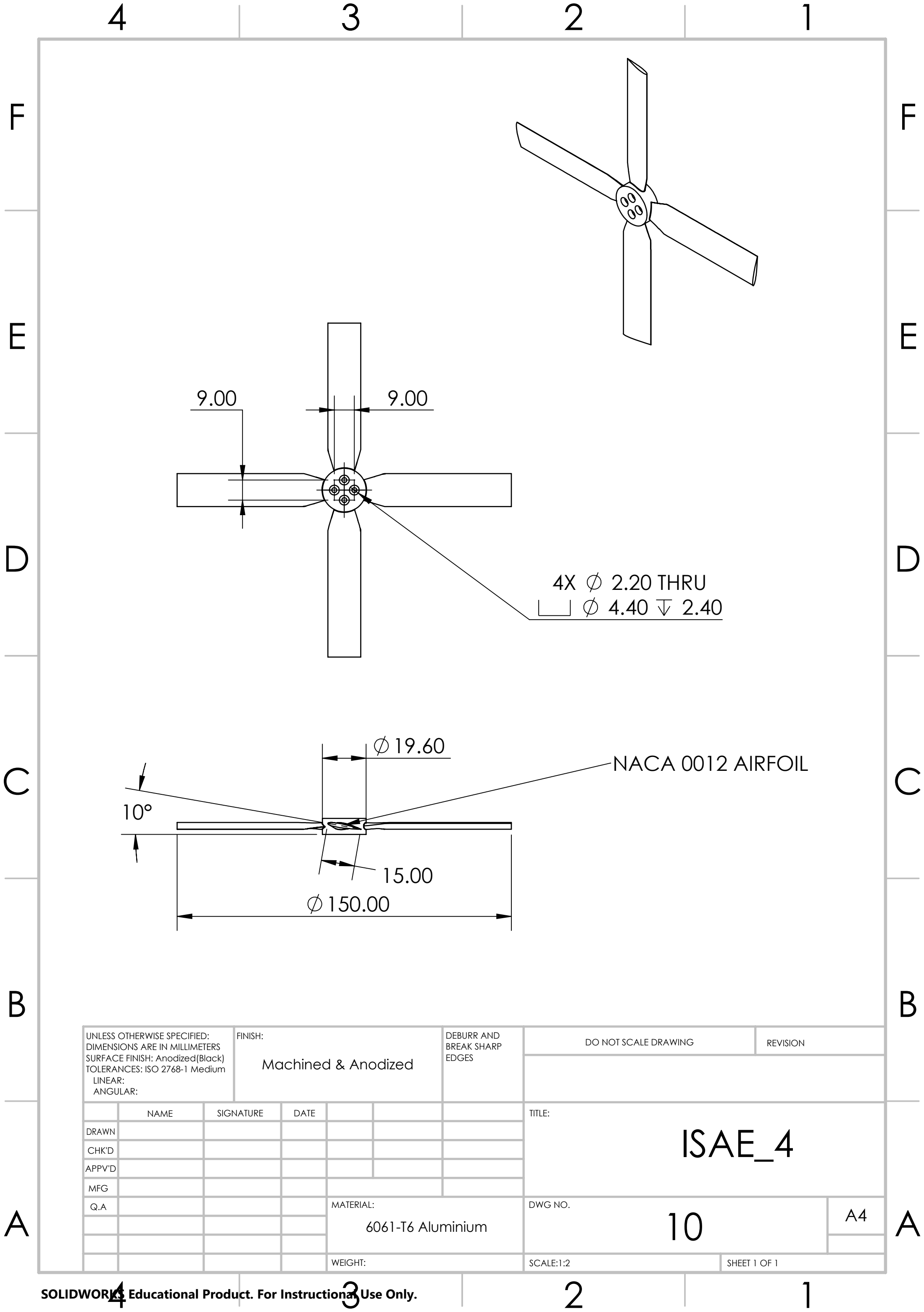

Fig. A.10: ISAE-4 Rotor

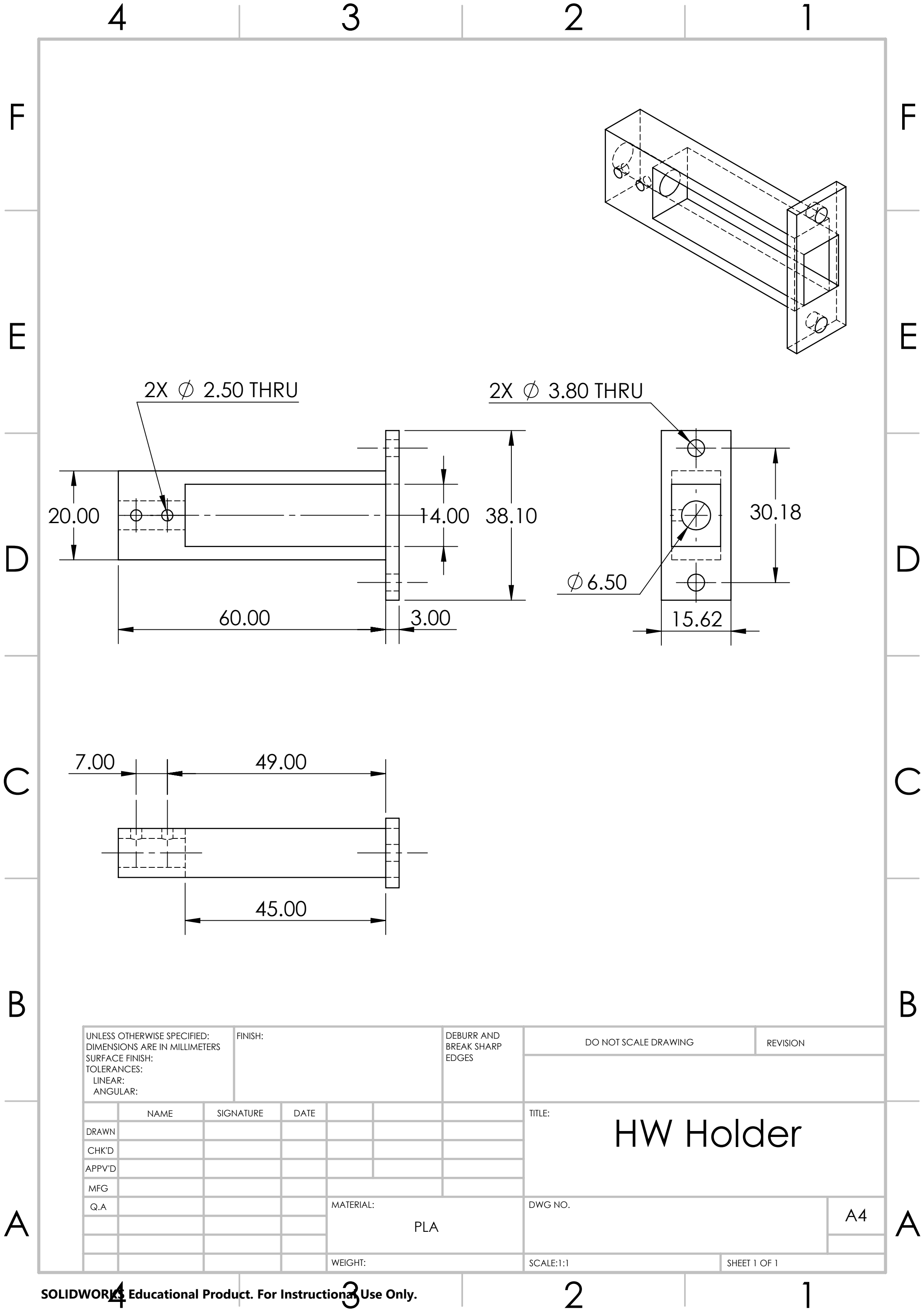

Fig. A.11: Hotwire Holder

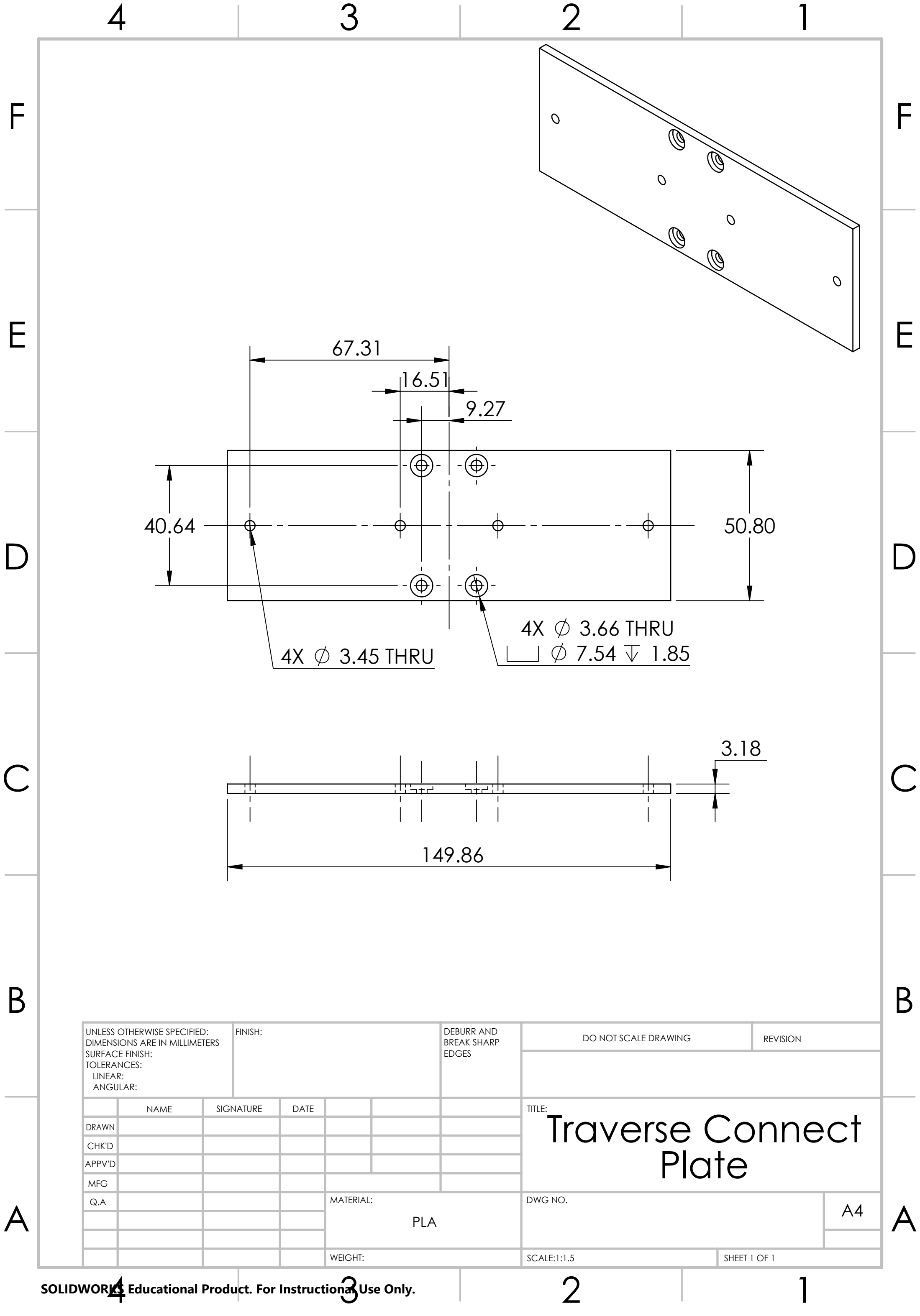

Fig. A.12: Traverse Connecting Plate

Appendix B

LABVIEW Software

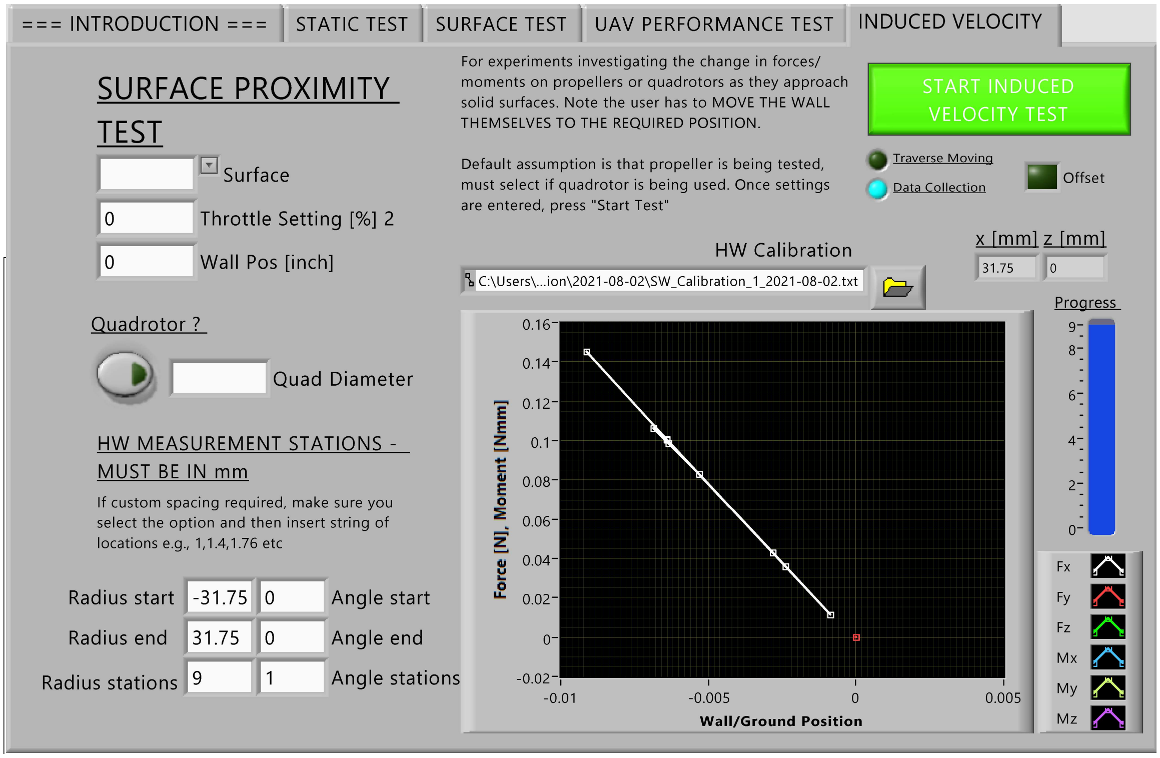

SURFACE PROXIMITY TEST

Surface

Throttle Setting [%] 2: 0

Wall Pos [inch]: 0

Quadrotor ?

Quad Diameter

HW MEASUREMENT STATIONS - MUST BE IN mm

If custom spacing required, make sure you select the option and then insert string of locations e.g., 1,1.4,1.76 etc

Radius start: -31.75 — Angle start: 0

Radius end: 31.75 — Angle end: 0

Radius stations: 9 — Angle stations: 1

For experiments investigating the change in forces/ moments on propellers or quadrotors as they approach solid surfaces. Note the user has to MOVE THE WALL THEMSELVES TO THE REQUIRED POSITION.

Default assumption is that propeller is being tested, must select if quadrotor is being used. Once settings are entered, press "Start Test"

HW Calibration: C:\Users\...ion\2021-08-02\SW_Calibration_1_2021-08-02.txt

x [mm]: 31.75

z [mm]: 0

Fig. B.1: LABVIEW Program Front Panel

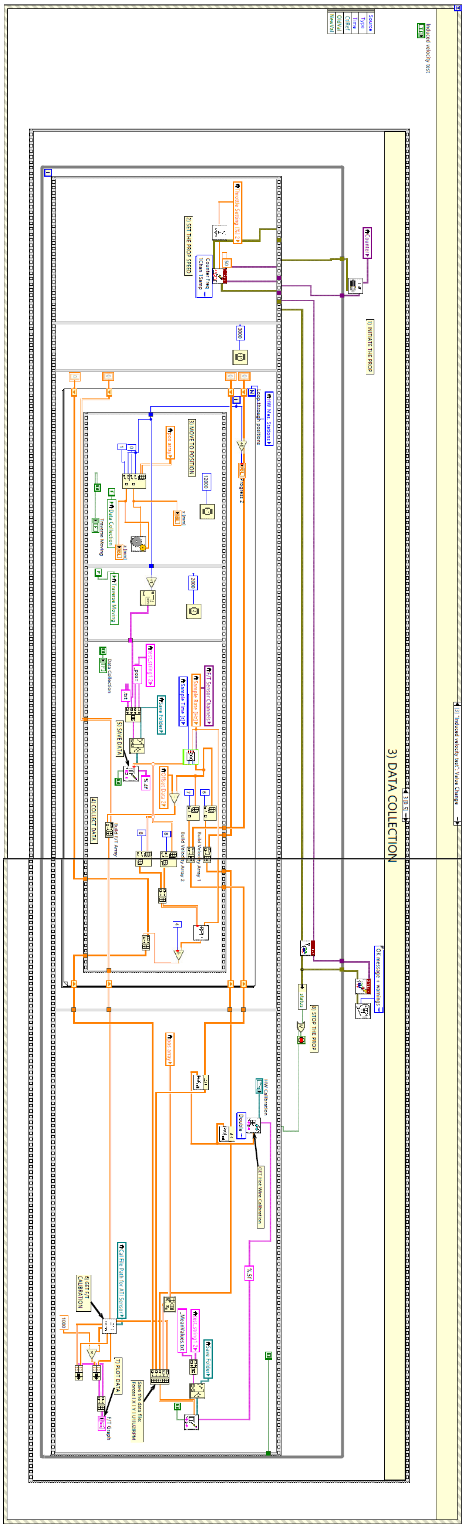

Fig. B.2: LABVIEW Program Block Diagram